



UNIVERSITÄT  
BAYREUTH

# **Modelling the non-linear mechanics of polymeric microcapsules and hydrogels**

**Ali Ghaemi**

geboren in Zanjan, Iran

Von der Universität Bayreuth  
zur Erlangung des Grades eines  
Doktors der Naturwissenschaften (Dr. rer. nat.)  
vorgelegte Abhandlung

1. Gutachter: Prof. Dr. Stephan Gekle
2. Gutachter: Prof. Dr. Stephan Kümmel

Tag der Einreichung: 14. Februar 2018

Tag des Kolloquiums: 16. Mai 2018



To my loving parents:  
S. Ebadati & A. Ghaemi



## **Acknowledgements**

First and foremost I would like to express my sincere gratitude to my supervisor Prof. Dr. Stephan Gekle who invited me to join his amazing research group at the University of Bayreuth. Thanks to him, I had the opportunity to work on the most interesting projects, and in collaboration with several motivated researchers from different universities and companies. The goals of these projects could not be achieved without their valuable contributions. So many thanks go to Prof. Andreas Ferry and his student, Alexandra Phillip (From TU Dresden and University of Bayreuth) who together with our collaborators from Henkel and Follmann companies provided us with the microcapsule samples and the results of the micro-mechanical tests. Manufacturing of Poly(NIPAM) mats and their experimental analyses would be impossible without Li Liu's tireless efforts under Prof. Seema Agarwal's supervision. I am also grateful to Inga Melnyk from IPF in Dresden, and the other members of the aforementioned research groups for all the insightful discussions on different aspects of microcapsule technology and actuators.

I would like to thank Markus Hilts and Stephan Brütting from university of Bayreuth for their awesome IT supports and their immediate and effective solutions to the technical problems. I also appreciate the assistance of many people in the administration, including Claudia Brandt and Thomas Hoefft who guided me through the labyrinth of German bureaucracy.

I am very grateful to the members of our dynamic and enthusiastic group, specially Achim, Abdallah, Axel, Christian, Carina and Miriam for our amusing talks, scientific and technical discussions, their patience with me learning German and their readiness to contribute whenever I needed their help or opinion. During this time, I had also the good fortune of meeting and living with many special people who made my stay in Bayreuth a fun and memorable experience. I am thankful to all, in particular to Dominic Schäfczuk for being so friendly and helpful and for our amusing sightseeings in Bavaria.

Finally, I would like to express my eternal gratitude towards my parents for their continuous supports and their unconditional Love.



## Abstract

Polymeric parts are used in a wide range of products from textile and cosmetics to all types of electronic devices. The quality and performance of these parts depend highly on their mechanical behaviour. Therefore, it is important to understand their mechanics and to be capable of predicting their performance under the conditions specific to their use.

In this work the mechanical behaviour of two types of polymeric parts in different applications are investigated. The first type is a sample of polymeric microcapsules that serve as perfume oil containers in washing detergents. During the washing, they are expected to remain stable. However, they should break and release their contents during the storage or the wearing time of the washed textiles, hence extending their softness and fresh smell. The second system is a hydrogel actuator which has a bilayer structure. One layer is composed of aligned and the other of randomly oriented poly(N-isopropyl acrylamide) fibers. When the bilayer mat is put in water it folds into a stable 3D structure, which can be used as a scaffold for cell culture and in tissue engineering.

In this work that is presented in four chapters, numerical methods are used to understand the mechanics underlying the deformation of the studied polymeric parts. The corresponding simulations complement the mechanical tests, by making the calculation of the mechanical properties possible, and contribute to the explanation of the experimental observations.

Chapter one is the extended abstract of the following three chapters that contain the full text of our publications. In addition to present a detailed outline of the contents of each publication, it describes the relationship between them in a broader context. Furthermore, it explains the contribution of the thesis to the topics that are addressed in this research as well as the author's contributions to each publication.

In chapter two, finite element analysis (FEA) together with nano-indentation experiments is applied to study the mechanics of perfume containing microcapsules under uniaxial compression. An elastic-perfectly plastic model is proposed to reproduce the results of the mechanical tests. Furthermore, with the help of FEA calculations the corresponding mechanical properties are approximated. Then, using the detailed stress distribution maps, a breakup mechanism is proposed. At the end, this mechanism is validated by predicting the shape of the broken capsules.

The focus of chapter three is on the deformation dynamics and the breakup of such capsules in a generic shear flow. In this study, the shells of the capsules have a finite thickness, and their mechanics are described by an elastic or elastic-perfectly plastic constitutive laws. It is shown that under the hydrodynamic stresses, the originally circular elastic shell deforms into an ellipse with a steady shape. After recovering the reported results on the deformation dynamics of the elastic capsules, we show that the finite thickness of the shell changes during its deformation, such that it is thinner at the equator of the equilibrium ellipse, and thicker in the poles. We explain the relationship between this observation and the distribution of the normal and the circumferential stresses in the shell thickness, in order to propose a possible breakup mechanism at higher shear rates. We continue by demonstrating the effects of the plasticity and the strain-hardening on the deformation and the break-up of the capsules. It is found that if the shear rate is high enough for the deformation to enter the plastic regime, the capsule elongates more than its elastic counterpart. Furthermore, the thinner shells are shown to be more sensitive to plasticity. Finally, it is demonstrated that, if the plastic deformation is followed by a strain-hardening regime as it has been observed for microcapsules studied in chapter two, the breakup can be significantly delayed or even prevented completely.

In chapter four, we present a bilayer actuator made of poly(N-isopropyl acrylamide) hydrogel. It displays an irreversible change in shape by rolling when it is in contact with water. To meet the requirements of its applications in tissue engineering, it is important to predict and to control the final folded shape of the system. Here, we apply a simplified anisotropic elastic model, with respect to the morphology of the fibers in individual layers, in order to predict its final three-dimensional shape in water. The results of this analysis demonstrate the necessity of considering the anisotropy of the mechanical properties in modelling the large non-linear deformations of this system.

**Keywords:** Microcapsule, Hydrogel, Mechanical characterization, Elastic-perfectly-plastic, anisotropy, non-linear deformation, Nano-indentation, Shear flow.

## **Zusammenfassung**

Polymere Bestandteile finden sich in verschiedenen Produkten, zum Beispiel Textilien und Kosmetika. Sie werden ebenfalls in allen Arten von elektronischen Geräten verwendet. Die Qualität und Leistung dieser Teile hängt stark von ihrem mechanischen Verhalten ab. Daher ist es wichtig, ihre Mechanik zu verstehen und ihre Leistung unter den spezifischen Anwendungsbedingungen vorherzusagen.

In dieser Arbeit wird das mechanische Verhalten von zwei Arten von Polymeren Bestandteilen in verschiedenen Anwendungen untersucht. Der erste Typ ist eine Probe von polymeren Mikrokapseln, die als Parfümölbehälter in Waschmitteln dienen. Während des Waschens wird erwartet, dass sie stabil bleiben. Sie sollten jedoch während der Lagerung oder der Tragezeit der gewaschenen Textilien brechen und ihren Inhalt freisetzen. Hierdurch wird die Weichheit und der frische Geruch der Wäsche verlängert. Das zweite System ist ein Hydrogel-Aktuator, der eine Doppelschichtstruktur aufweist. Eine Schicht besteht aus ausgerichteten und die andere aus zufällig orientierten Poly(N-Isopropylacrylamid)-Fasern. Wenn die Doppelschichtmatte in Wasser gelegt wird, faltet sie sich zu einer stabilen 3D-Struktur, die als Gerüst für Zellkulturen und im Tissue Engineering verwendet werden kann.

In dieser Arbeit, die in vier Kapiteln eingeteilt ist, werden numerische Methoden verwendet, um die Mechanik zu verstehen, die der Verformung der untersuchten Polymerteile zugrunde liegt. Die entsprechenden Simulationen ergänzen die mechanischen Tests, indem sie die Berechnung der mechanischen Eigenschaften ermöglichen und zur Erklärung der experimentellen Beobachtungen beitragen.

Kapitel eins ist die erweiterte Zusammenfassung der folgenden drei Kapitel, die den vollständigen Text unserer Publikationen enthalten. Neben einer detaillierten Darstellung der Inhalte jeder Publikation beschreibt sie die Beziehung zwischen ihnen in einem breiteren Kontext. Darüber hinaus erklärt sie den Beitrag der vorliegenden Arbeit zu den behandelten Themenfeldern, sowie den Beitrag des Autors zu jeder Veröffentlichung.

In Kapitel zwei wird die Finite-Elemente-Analyse (FEA) zusammen mit Nanoindentationsexperimenten angewendet, um die Mechanik parfümhaltiger Mikrokapseln unter uniaxialer Kompression zu untersuchen. Ein elastisch-perfekt plastisches Modell wird vorgeschlagen,

um die Ergebnisse der mechanischen Tests zu reproduzieren. Darüber hinaus werden mit Hilfe von FEA-Berechnungen die entsprechenden mechanischen Eigenschaften approximiert. Dann wird unter Verwendung der detaillierten Belastungsverteilungskarten ein Bruchmechanismus vorgeschlagen. Am Ende wird dieser Mechanismus validiert, indem die Form der kaputten Kapseln vorhergesagt wird.

Der Fokus des dritten Kapitels liegt auf der Deformationsdynamik und dem Aufbrechen solcher Kapseln in einem generischen Scherfluss. In dieser Studie haben die Schalen der Kapseln eine endliche Dicke, und ihre Mechanik wird durch elastische oder elastisch-perfekt plastische konstitutive Gesetze beschrieben. Es wird gezeigt, dass sich die ursprünglich kreisförmige elastische Schale unter den hydrodynamischen Spannungen zu einer elliptischen Form mit konstanter Geometrie verformt. Nachdem wir Ergebnisse aus der Literatur über die Deformationsdynamik der rein elastischen Kapseln reproduzieren, zeigen wir, dass sich die endliche Dicke der Schale während ihrer Verformung ändert, so dass sie am Äquator der Gleichgewichtsellipse dünner und an den Polen dicker ist. Wir erklären die Beziehung zwischen dieser Beobachtung und der Verteilung der Normal- und Umfangsspannungen in der Schale, um einen möglichen Auflösungsmechanismus bei höheren Scherraten vorzuschlagen. Weiterhin demonstrieren wir die Auswirkungen der Plastizität und der Kaltverfestigung auf die Verformung und das Aufbrechen der Kapseln demonstrieren. Wir finden, dass, wenn die Schergeschwindigkeit hoch genug ist, die Verformung im plastischen Bereich stattfindet und die Kapsel sich weiter dehnt als im rein elastischen Fall. Darüber hinaus zeigen die dünneren Schalen eine höhere Empfindlichkeit gegenüber Plastizität. Schließlich wird gezeigt, dass, wenn auf die plastische Verformung ein Verfestigungsregime folgt, wie es für die in Kapitel zwei untersuchten Mikrokapseln beobachtet wurde, das Aufbrechen signifikant verzögert oder sogar vollständig verhindert werden kann.

In Kapitel vier präsentieren wir einen Doppelschicht-Aktuator aus Poly (N-Isopropylacrylamid) Hydrogel. Er zeigt eine irreversible Formänderung durch Rollen, wenn er in Kontakt mit Wasser kommt. Um die Anforderungen seiner Anwendungen im Tissue Engineering zu erfüllen, ist es wichtig, die endgültige gefaltete Form des Systems vorherzusagen und zu kontrollieren. Hier wenden wir ein vereinfachtes anisotropes elastisches Modell in Bezug auf die Morphologie der Fasern in einzelnen Schichten an, um ihre endgültige dreidimensionale Form in Wasser vorherzusagen. Die Ergebnisse dieser Analyse zeigen die Notwendigkeit, die Anisotropie der mechanischen Eigenschaften bei der Modellierung der großen nichtlinearen Deformationen dieses Systems zu berücksichtigen.

**Stichworte:** Mikrokapsel, Hydrogel, mechanische Charakterisierung, elastisch-perfekt-Kunststoff, Anisotropie, nichtlineare Verformung, Nano-Eindruck, Scherfluss.

# Table of contents

<b>1</b>	<b>Extended Abstract</b>	<b>1</b>
1.1	General Introduction . . . . .	1
1.2	The mechanics of microcapsules . . . . .	2
1.2.1	Experimental approach . . . . .	3
1.2.2	Mechanical characterization of microcapsules . . . . .	3
1.2.2.1	Elastic deformation of microcapsules . . . . .	6
1.2.2.2	Plastic deformation of microcapsules . . . . .	6
1.2.2.3	Strain-hardening regime . . . . .	8
1.3	Deformation and dynamics of capsules in shear flow . . . . .	9
1.3.1	Verifying the numerical method . . . . .	10
1.3.2	Thinning of the Elastic shells . . . . .	10
1.3.3	The onset of plasticity and its influence on capsule deformation . . . . .	11
1.3.4	Strain hardening . . . . .	11
1.3.5	Capsules under cyclic loading . . . . .	11
1.4	The mechanics of hydrogel actuators . . . . .	12
1.4.1	Experimental observations . . . . .	12
1.4.2	Numerical analysis . . . . .	15
1.5	General conclusion and outlook . . . . .	16
1.6	Author's contribution . . . . .	17
1.7	List of our publications in peer reviewed journals . . . . .	18
1.8	List of conference presentations . . . . .	18
1.8.1	Oral presentations . . . . .	19
1.8.2	Poster presentations . . . . .	19
<b>2</b>	<b>Mechanical behaviour of micro-capsules and their rupture under compression</b>	<b>21</b>
2.1	Introduction . . . . .	22
2.2	Methods . . . . .	25
2.2.1	Sample preparation and experiments . . . . .	25

2.2.1.1	The composition of micro-capsules . . . . .	25
2.2.1.2	Nano-indentation experiments . . . . .	25
2.2.1.3	AFM imaging . . . . .	26
2.2.2	Finite element simulations . . . . .	26
2.3	Results and Discussion . . . . .	27
2.3.1	Geometrical characterization . . . . .	27
2.3.2	Wall thickness characterization . . . . .	28
2.3.3	AFM compression experiments . . . . .	28
2.3.4	FEM simulations . . . . .	29
2.3.5	Characterization of micro-capsule rupture . . . . .	31
2.4	Conclusion . . . . .	32
2.5	Supplementary information . . . . .	35
<b>3</b>	<b>Plastic deformations of microcapsules with finite thicknesses in shear flow</b>	<b>41</b>
3.1	Introduction . . . . .	42
3.2	Methods . . . . .	43
3.3	Results and Discussion . . . . .	44
3.3.1	Elastic capsules with finite wall thickness . . . . .	45
3.3.1.1	Deformation dynamics . . . . .	45
3.3.1.2	Thinning of elastic shells . . . . .	47
3.3.2	Plastic deformation of the shell . . . . .	50
3.3.2.1	Onset of plasticity . . . . .	50
3.3.2.2	Pre-rupture hardening . . . . .	51
3.3.2.3	Capsule breakup under cyclic shear flow . . . . .	52
3.4	Conclusions . . . . .	55
3.5	Supplementary information . . . . .	57
<b>4</b>	<b>One-component dual actuation: Poly(NIPAM) can actuate to stable 3D forms with reversible size change</b>	<b>63</b>
4.1	Main text . . . . .	64
4.2	Supplementary information . . . . .	73
	<b>References</b>	<b>79</b>

# Chapter 1

## Extended Abstract

### 1.1 General Introduction

Polymeric parts are used in a wide range of applications from textile and furniture to all forms of transportation. The quality and performance of many polymeric products depend highly on their mechanical behaviour. For instance, in applications where polymers are replacing woods or metals, such as plastic chairs, polymeric gears and pipes, the final products need to be stable, showing the minimum deformation under the mechanical loads. In other cases such as shoe insoles and stretch clothes, they need to reversibly deform in order to offer the highest comfort and product durability. In some modern applications, however the criteria for the optimum mechanical performance of polymeric products are far more complicated. For instance for microcapsules used in washing detergents and cosmetics. The polymeric shells of these minute containers need to be on the one hand mechanically stable in order to preserve their contents, and on the other hand easily breakable when they should be released [1–11].

Understanding the mechanical behaviour of the polymeric products, and predicting their performance under realistic conditions is often very complicated. In many cases, such as shoe insoles and stretch clothes, the products undergo large non-linear deformations, which can not be addressed by the analytical solutions of the corresponding deformation equations. In other products, like polymeric composites or textiles, the anisotropy or non-linear material properties add other layers of complexity to their mechanical behaviour. The problem in hand gets even more complicated when the products are too small, such as microcapsules, or too fragile, such as the soaked and swelled hydrogels, to be characterized using the conventional mechanical tests.

Numerical analyses offer a diverse and powerful set of tools to address these types of problems. One of the numerical methods that is particularly developed to simulate the

mechanics of solid parts is the finite element method. During the last years this analysis has been widely used to characterise the mechanical behaviour of different types of polymeric products in realistic deformation scenarios [12–22].

In this work, using a combination of different numerical tools and experimental methods, we are facing the challenge of characterizing the mechanical behaviour of two types of polymeric parts in different applications. In the second chapter, the non-linear deformations of individual perfume containing Melamine-formaldehyde microcapsules under uni-axial compression are investigated. An elastic-perfectly plastic model is proposed to account for the mechanical behaviour of their shells. The corresponding governing equations are solved in the finite element based software, Abaqus, and the mechanical model is validated by successfully reproducing the results of nano-indentation experiments that are carried out by Prof. A. Fery's group. This experimental-numerical approach intends to provide the manufactures with a detailed understanding the mechanics of this particular product, in order to optimize their morphology. In chapter three, for the first time, the deformation dynamics and the breakup of similar capsules in a generic shear flow are addressed. In addition to the geometrical non-linearity of the capsule deformation, and the non-linear mechanical behaviour of the shell, studying this phenomena includes solving a complicated fluid-structure interaction problem which is handled using the immersed-boundary method based solvers implemented in Abaqus-2016. In order to validate the applied numerical solvers, the results for the simplified elastic capsules are compared to the similar case studies in the literature. Then, the effects of shell thickness, plasticity and strain hardening on the deformation and breakup dynamics of capsules are presented. In chapter four, a rare example of hydrogel actuators with possible applications in tissue engineering are studied. This system is composed of two layers which are tied to each other through a stable cross-linked interface. One layer is made of mostly unidirectionally aligned poly(N-isopropyl acrylamide) fibers. The other layer is composed of similar, but randomly oriented fibers. The non-linear three dimensional deformations of the resulting hydrogel actuators are studied using a simplified elastic but anisotropic model. The results of this analysis demonstrate the necessity of considering anisotropy in modelling the response of this actuator to water.

## 1.2 The mechanics of microcapsules

Deformation and breakup of microcapsules under compression is a common scenario in several applications, particularly those where they are expected to be triggered mechanically in order to release their contents. For instance, in cosmetic creams where they should break during the massage or rubbing against the skin [2–6]. The same applies to the perfume

containing microcapsules used in laundry detergents. The capsules in these products are expected to attach to the fabrics of the textile, and to break during the very last stages of the washing process, or in the storage time, and during wearing [7–11].

### 1.2.1 Experimental approach

Understanding the mechanics of microcapsules is of great importance to the manufacturer. However, due to their small size and fragility it is very difficult to measure their mechanical properties using the common mechanical tests. In this context, single microcapsule experiments are developed where the specimen is compressed between two parallel surfaces [23–31]. Similarly, in this project the individual microcapsules are compressed in a nano-indentation device. The experimental setup that is used in Prof. Fery's group is presented schematically in Fig.1.1-a. It is mainly composed of an atomic force microscope (AFM) and a light microscope. The latter which is placed below the glass substrate Fig.1.1-a-I, records the micrographs of the capsule at the beginning of the experiment and after the capsule is broken Fig.1.1-(b,c). The micrographs of the intact microcapsules are used to estimate their size, i.e. the external diameter. In the compression test, the cantilever of the AFM moves towards the substrate, and the sapphire attached to it presses against the capsule wall. The force exerted by the capsule, as well as the corresponding position of the indenter are recorded by AFM, giving a force-displacement graph up to the capsule's breaking point, Fig.1.1-e. Thereafter, the broken capsules are subjected to AFM microscopy to measure their thicknesses. In the resulting height profiles, half of the height of the second connecting baseline gives an approximation of shell thickness, Fig.1.1-d.

### 1.2.2 Mechanical characterization of microcapsules

The outcome of the compression test is a complex force-displacement relationship, Fig.1.1-e, which can not be readily analysed to reveal the mechanical properties of the system. In order to characterise similar experimental data, researchers often use the solutions of the simplified analytical models [33–37]. The equation that has often been applied is based on Reisner's shell theory [38, 39]. It states a linear relationship between the exerted point force on the thin wall of an empty capsule and its infinitesimal displacement as follows:

$$\frac{F}{EHR_i} = \frac{4}{\sqrt{3(1-\nu^2)}} \frac{H}{R_i} \alpha \quad (1.1)$$

where  $F$  is the compression force,  $H$  is the wall thickness of the shell,  $R_i$  is the inner radius of the shell,  $E$  is Young's modulus,  $\nu$  is Poisson's ratio,  $\alpha = \frac{d}{2R_i}$  is the fractional displacement,

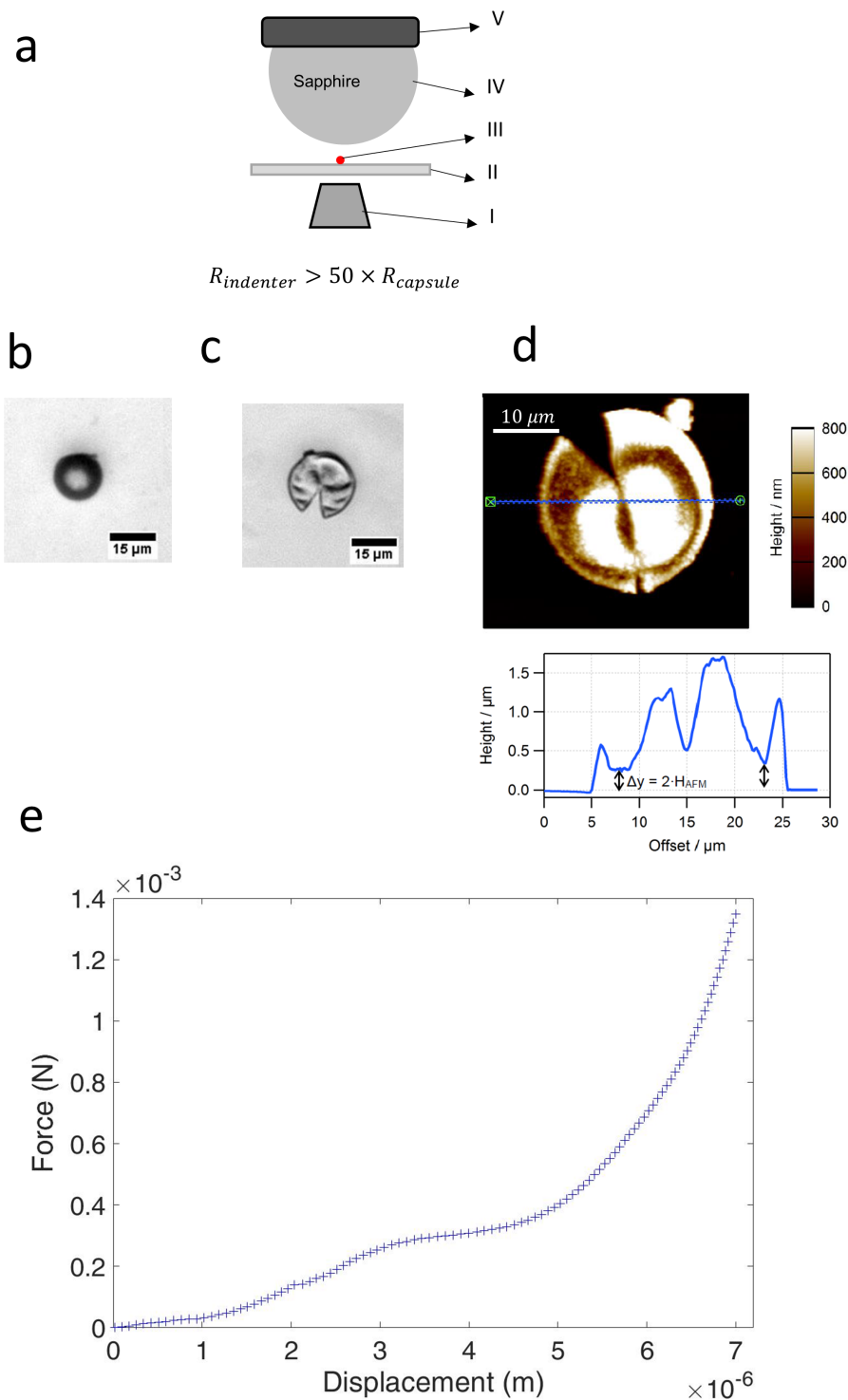


Fig. 1.1 (a) the experimental set-up of the nano-indentation test. I: The schematic light microscope. II: the glass substrate that is placed above the microscope. III: The microcapsule sample on the substrate. IV: the sapphire indenter with a radius more than 50 times larger than the size of the capsule. V: The cantilever of the AFM. (b) The micrograph of the intact capsule. (c) The micrograph of the ruptured capsule. (d) Top: the AFM height contours of the ruptured microcapsule with a marked cross section (blue line). Bottom: the corresponding height profile of the marked cross section. (e) The force exerted by the capsule on the indenter against its displacement. (b),(c),(d) are taken from [32].

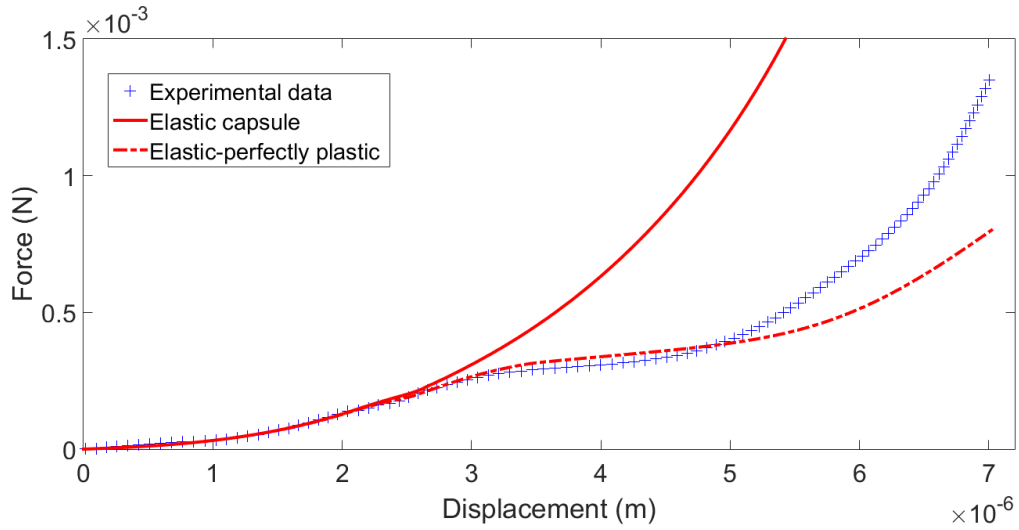


Fig. 1.2 The experimental force-displacement graph for an exemplary microcapsule with  $R = 6.25 \mu\text{m}$  and  $H = 190 \text{ nm}$  is shown with blue crosses. The red lines correspond to the finite element simulations of a microcapsule of the same size and thickness, but with different constitutive laws as described in the legend.

and  $d$  is the displacement of the indenter. When applied carefully for very small deformations of microcapsules [29, 26, 32], this method may give an acceptable approximation of  $E$ . However, Fig.1.2 clearly shows that for the largest part of the deformation, the response of the exemplary microcapsule is non-linear, i.e.  $\frac{dF}{d\alpha} \neq \text{constant}$ , and its mechanical behaviour can not be explained using Eq. (1.1).

There are two sources of non-linearity in the overall deformations of the capsules with a liquid core under uni-axial compression. One source is the readily observed geometrical non-linearity of the capsule deformation. The other is the non-linear mechanical behaviour of the shell material, i.e.  $\frac{d\sigma}{d\varepsilon} \neq \text{constant}$  where  $\sigma$  and  $\varepsilon$  are the local stress and the strain in the capsule shell. The existing analytical approaches do not include these complexities, hence their predictions of the whole deformation do not agree with the experimental results.

Numerical methods, such as finite element analysis, on the other hand can address this problem using the discretization of the applied load and the deformation, and by solving the corresponding governing equations by means of numerical approximations, e.g. Newton-Raphson method. More information on the model and the numerical process used for this particular problem are available in [32, 40]. In the following sections the results of the numerical simulations of the nano-indentation test for an exemplary microcapsule are presented.

### 1.2.2.1 Elastic deformation of microcapsules

Although polymeric parts do not behave as Hookean elastics in large deformations, this simplified model explains their small deformations satisfactorily. In particular, for the small deformations of microcapsules with an incompressible liquid core, assuming a Hookean elasticity leads to an agreement between the results of the experimental and the numerical methods, Fig.1.2 [32, 41, 26, 29]. In this regime the non-linear response of the capsules results from the geometrical non-linearity of its deformation, and is considered in finite element simulations. However, for further displacements of the indenter,  $0.06 < \alpha < \frac{d_{breakup}}{2R} \approx 0.64$ , the results of such a simplified model deviates drastically from those of the experiment Fig.1.2.

### 1.2.2.2 Plastic deformation of microcapsules

In large deformations of polymeric parts, some of the physical interactions and cross-links between the polymer chains are broken or irreversibly dislocated. As a result the resistance of the polymeric body to the external deforming forces decreases, and it yields [42, 43]. The macroscopic observation of this phenomenon is the sudden drop of the measured stress rate, i.e.  $\frac{d\sigma}{d\varepsilon}$ , during the mechanical test, and the irreversible deformation of the polymeric part [44–46, 42, 47]. Such behaviour has been experimentally confirmed in case of similar microcapsules [46]. Therefore, inspired by former studies on melamine-formaldehyde systems [29, 26], an elastic-perfectly plastic constitutive law is considered for the mechanics of the shell. The schematic stress-strain curve of this model for one-dimensional deformation is depicted in Fig.1.3-a. The strain on the horizontal axis is the true strain (also referred to as Hencky strain in chapter two), defined as  $\varepsilon = \int_{l_0}^l \frac{dl}{l} = \ln \frac{l}{l_0}$ , where  $l_0$  and  $l$  are the original and the current lengths of the beam respectively, and the vertical axis shows the conjugate true stress [40]. The elastic part of the deformation follows the linear Hooke's law,  $\sigma = E\varepsilon$ , where  $E$  is the elastic modulus. The plastic regime is considered to be isothermal and independent of strain rate, and takes place when the total stress reaches a given value  $\sigma_y$ , defined as the yield stress. Thereafter during the plastic deformation the value of stress does not change, see Fig.1.3-a.

In three-dimensional deformation, the elastic regime is explained by the generalized Hooke's law,  $\sigma = C : \varepsilon$ , where  $C$  is the stiffness tensor. Moreover, the equivalent stress and strain are defined according to the von Mises criterion. This criterion states that a body yields when the second invariant of the stress deviator tensor equals an intrinsic value,  $\sigma_{VM}^2$ , which depends only on the material. Afterwards, the part behaves like a viscous incompressible fluid. From the equations of motion, von Mises derives the following for the equivalent stress

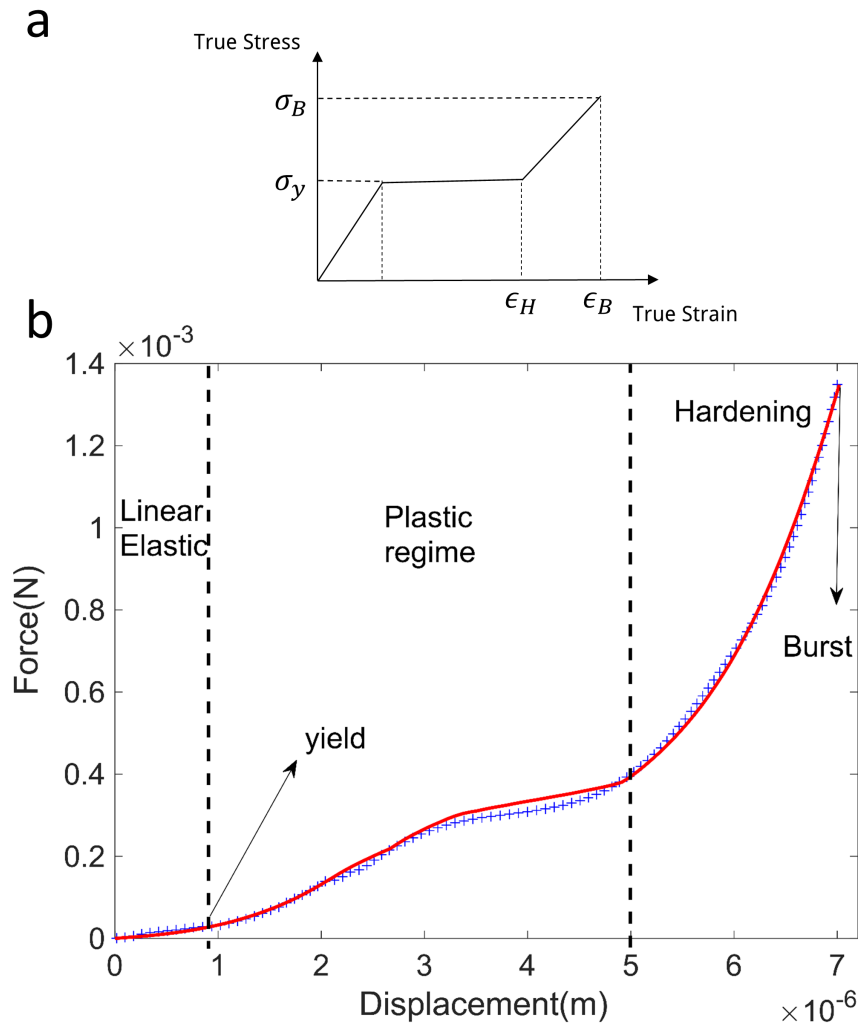


Fig. 1.3 (a) The true stress-strain relationship for a one-dimensional rod with an elastic-perfectly plastic behaviour under uni-axial load. This graph is characterised by a linear elastic regime till the start of plasticity when the normal stress equals the yield stress,  $\sigma_y$ . The plastic part of deformation is shown as a plateau till the beginning of strain-hardening regime at  $\epsilon_H$ . After a linear increase of stress in the sample, the deformation ends at  $(\epsilon_B, \sigma_B)$ , standing for the stress and the strain at the breaking point. (b) The mechanical characterization of the force-displacement data for a microcapsule with  $R = 6.25 \mu\text{m}$  and  $H = 190 \text{ nm}$ . The measured force against the displacement of the AFM probe is shown in blue. The corresponding numerical results from the FEM simulation assuming an elastic-perfectly plastic constitutive law with a final strain-hardening is plotted in red. Different regimes of deformation are separated by dashed lines.

[48, 45]:

$$\sigma_{VM} = \sqrt{\frac{1}{2}[(\sigma_{xx} - \sigma_{yy})^2 + (\sigma_{yy} - \sigma_{zz})^2 + (\sigma_{zz} - \sigma_{xx})^2] + 3(\sigma_{xy}^2 + \sigma_{xz}^2 + \sigma_{yz}^2)} \quad (1.2)$$

where  $\sigma_{ij}$  are the components of the Cauchy stress tensor and  $\sigma_{VM}$  is the equivalent von Mises stress. This model was originally developed and applied to explain the perfect plasticity, i.e. independent of temperature and of strain rate, of solid metals [48, 49]. The yielding of the polymers in general is a complex phenomena, and this simplified model can not fully capture all the aspects of their plastic deformation, e.g. anisotropy of yielding, temperature and strain rate dependencies [50–58]. However, Mercade *et al.* [29, 26] used the same model to successfully describe the plastic deformation of microcapsules enclosing a liquid core. We find that assuming a perfect plastic regime in the larger deformations of the microcapsules, i.e. when  $0.06 < \alpha$ , results in a better agreement between the numerical prediction and the experimental outcome, see Fig.1.2. However, in further displacement ratios  $0.2 < \alpha$ , there is a noticeable difference between the results of the two methods (Fig.1.2).

### 1.2.2.3 Strain-hardening regime

In the mechanical test of many polymeric specimens, a strain-hardening regime is observed before the breakup. This deformation regime appears as an increase of the measured stress at the end of the plastic deformation [59–63, 43]. A similar behaviour has been reported for liquid containing melamine-formaldehyde microcapsules under uni-axial compression [29]. A linear relationship as the simplest possible scenario to account for the increase of the equivalent stress is considered here. Consequently, the results of the numerical simulations get closer to the corresponding experimental measurements, as shown in Fig.1.3.

Therefore, the finite element simulation reveals the existence of three deformation regimes, that are located in the corresponding force-displacement graph: (i) a linearly elastic regime (approximately for  $0 < \alpha < 0.06$ ), (ii) a plastic regime in which the equivalent stress in the material saturates at a maximum value due to yielding (approximately for  $0.6 < \alpha < 0.4$ ) and (iii) a strain-hardening regime in which the stress rapidly increases again.

In chapter one, we show that all the microcapsule specimens show a similar behaviour. Furthermore, we use the results of FEM simulations to generate detailed maps of the pre-breakup stress distribution in the thickness of the shell. Accordingly, we propose a possible burst mechanism for the filled elastic- perfectly plastic microcapsules under uni-axial compression.

### 1.3 Deformation and dynamics of capsules in shear flow

Deformation of capsules subjected to shear flow is relevant to applications where they are immersed in a flowing fluid environment, e.g. drug delivery systems in blood stream, perfume containers in washing cycles or capsules inside the microfluidic devices, and rheoscopes.

Many former studies [64] show that under linear shear flow an originally circular or spherical capsule deforms into an ellipse or an ellipsoid, respectively, as illustrated Fig.1.4-a. During the elongation phase, the Taylor deformation parameter  $D_{12} = \frac{R_a - R_c}{R_a + R_c}$ , where  $R_a$  and  $R_c$  are the main radii of the ellipse, constantly increases till it reaches an equilibrium value  $D_{12}^\infty$  as shown in Fig.1.4-b. For the infinitesimally thin shells the magnitude of  $D_{12}^\infty$  depends on the fluid properties, the applied shear rate, and the mechanical properties of the shell. This can be best described by the volume capillary number,  $Ca_v = \frac{\mu_{out}\dot{\gamma}}{G}$ , as the ratio of fluid viscous forces and the resistance of the shell to deformation. In this definition,  $\mu_{out}$  is the dynamic viscosity of the external fluid,  $\dot{\gamma}$  is the linear shear rate under which the capsule deforms, and  $G$  is the bulk shear modulus of the shell [64].

Studying this phenomenon includes solving a complicated fluid-structure interaction problem. In addition to the geometrical non-linearity of the capsule deformation, considering the full degrees of freedom for the position of the wall makes the problem in hand very non-trivial to solve. For very thin capsules, with simple mechanics such as fully elastic shell, in the regime of small deviations from the original shape, this problem has been addressed analytically. However, for the practically large deformations of capsules which are composed of shells with a finite thickness, applying the numerical methods is inevitable. The problem becomes even more complicated by considering a complex non-linear constitutive law for the shell such as viscoelastic and hyperelastic models. In this context several numerical tools are developed to address such complexity [65–92], see also the review articles [64, 93].

One of the proposed approaches is the immersed boundary method, where the fluid domain is meshed with the Eulerian elements, whose position is fixed while the associated velocity of the fluid changes, modelling the flow of the material. The position of the capsule wall on the other hand is determined through a Lagrangian analysis, where the deformable solid part is discretized with a moving grid.

In chapter three, using an immersed boundary method algorithm implemented in Abaqus [40], we address the dynamics and the deformation of an elastic-perfectly plastic capsule with a thick shell. This numerical tool which is extensively used in the literature [94–99] facilitates the coupling between the fluid and the structure during its non-linear deformation.

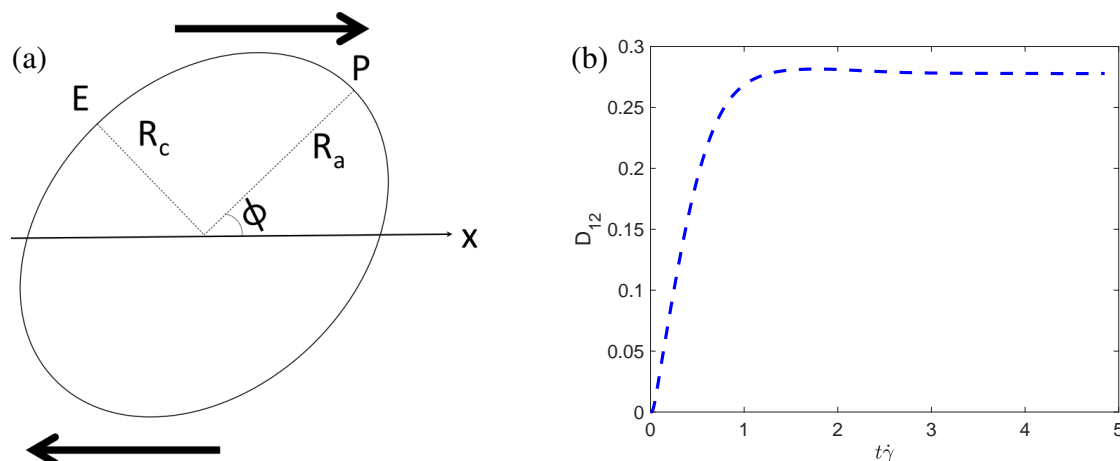


Fig. 1.4 (a) Schematic deformation of an elastic capsule under linear shear flow. The circular capsule deforms into an ellipse ( $R_a > R_c$ ) with the inclination angle  $\phi$ . "P" and "E" denote one of the poles and the equator of the ellipse, respectively. (b) Deformation parameter  $\frac{R_a - R_c}{R_a + R_c}$  against dimensionless time for an elastic capsule with  $H/R_o = 0.1$  in a linear shear flow such that  $Ca_v = 0.0075$ .

### 1.3.1 Verifying the numerical method

We validate the applied immersed boundary algorithm by comparing the FEM simulation results with independent studies. We show that in full agreement with former experimental [100–102] and numerical research, the originally circular cross-section of the capsule elongates in the straining direction, into an ellipse with a steady shape. Next, we demonstrate the quantitative consistency between the equilibrium Taylor parameter  $D_{12}^\infty$  of a capsule with  $H/R_o = 0.05$ , where  $H$  and  $R_o$  are the initial thickness and the outer radius of the circular cross-section, and those reported by Sui *et al.* [89] for infinitesimally thin shells enclosing a liquid core. For the capsules made of shells with a finite thickness we compare our results with Dupont *et al.* [103]. We report the same dependency of the deformation parameter on the thickness of the shell. Moreover, our work reproduces the collapse of the  $D_{12}$  for different values of shell thickness when plotted over the surface capillary number  $Ca_s = \frac{Ca_v}{R}$  as observed for 3D capsules.

### 1.3.2 Thinning of the Elastic shells

We show that, during the transient deformation of the capsule, the thickness of the shell changes such that the minimum and the maximum values for  $h/H$ , where  $h$  is the local thickness of the shell, occur at the equator and in the poles of the equilibrium ellipse respectively. The inhomogeneous thinning of the shell is studied in relation to the distribution

of the normal and the circumferential stresses in the shell thickness. Accordingly, it is demonstrated that the normal stresses play a determining role in the local thinning of the shell. This observation is used to suggest a possible breakup mechanism in higher shear rates.

### 1.3.3 The onset of plasticity and its influence on capsule deformation

Similar to our analysis of uniaxially compressed capsules in chapter two, we use the von Mises criteria for plasticity. We show that due to plasticity the resistance of the shell to deformation decreases, hence its  $D_{12}^\infty$  shifts to higher values as soon as the plastic deformation takes place. We continue our analysis by examining the effect of plasticity ratio, defined as  $Y = \sigma_y/E$ , on the dynamics of the deformation. We show that a lower plasticity ratio results in an earlier and a larger deviation from the corresponding elastic deformation. In fact, while shells with higher plasticity ratios,  $\sigma_y/E \geq 0.068$ , deform into more elongated steady shapes, shells with very low plasticity ratios are in general less resistant to deformation and thinning therefore more likely to break up. Thereafter, for an arbitrary plasticity ratio we report how shells with different thicknesses behave under the same flow condition. We show that the deformation parameters of the capsules with thinner plastic shells deviate more drastically from that of their elastic counterparts.

### 1.3.4 Strain hardening

We conclude our analysis of the plastic capsule deformation dynamics by reporting on the effect of strain hardening. We show that at the end of the plastic regime, the strain-hardening causes a resistance to the deforming hydrodynamic stresses. Consequently, the resulting  $D_{12}^\infty$  falls between those of the elastic-fully plastic and the elastic shells.

### 1.3.5 Capsules under cyclic loading

One of the important aspects of plastic deformation is the energy loss and the irreversible deformation of the system in periodic loading-unloading scenarios. This is of practical relevance in applications like washing, where the capsules are mechanically loaded and unloaded several times. Therefore, at the end of chapter three, we concern ourselves with the mechanical behaviour of capsules under cyclic shearing. Here, we compare the final deformed states of an arbitrary capsule under two different cyclic scenarios which take exactly the same time to finish. First, we demonstrate that shearing of the plastic capsules leads to their permanent deformation, similar to former experimental studies [104]. Furthermore, between

the two proposed scenarios the one with a longer uninterrupted shearing step deforms the capsule to a greater degree compared to the other scenario with two disconnected shearing steps.

## 1.4 The mechanics of hydrogel actuators

Hydrogels are three-dimensional and insoluble networks of hydrophilic polymers, that swell through the absorption of water without getting decomposed [47]. They are manufactured in industrial or laboratory scale for a wide range of applications, e.g. as absorbent in diaper, watering beads for plants, cell and bacterial culture in biotechnology, tissue engineering, cosmetics, perfume containing textile, and in a growing number of proposed biomedical applications such as drug and cell carriers [105–107].

Hydrogels are often manufactured and used as two-dimensional products like films or in simple three-dimensional shapes such as microspheres and beads [108]. However, in many of their modern and potential applications such as cell culture and tissue engineering, it is necessary to deform these simpler shapes into complex and pre-designed 3D structures. In such cases, predicting their overall size and shape in water plays an important role in optimizing their performances.

In chapter four, we present a one-component hydrogel manufactured by Li Liu in Prof. S. Agarwal's group. This novel system deforms into stable three-dimensional structures in water, and shows a temperature-triggered size change in the range of the biological temperatures, 4 – 40°C.

In the numerical part of this work, we propose two different models to account for the system's mechanical properties, which cannot be easily measured for the swollen hydrogel in water, due to its extreme fragility. We examine the validity of each model by comparing the results of the FEM simulations with the corresponding experimental observations.

### 1.4.1 Experimental observations

This system is composed of two fibrous layers. The main difference between the layers is the morphology of their fiber alignment. The fibers in one layer are mostly aligned, 97% vol., in one direction, while in the other layer they are randomly orientated in all directions, see Fig.1.5.

The fibres are the result of electro-spinning of a Poly(N-isopropyl acrylamide) solution. Collecting them on a cylindrical rotator at 800 *rpm* gives a layer with a finite thickness in which almost all the fibers are unidirectionally aligned. However, collecting the same fibers

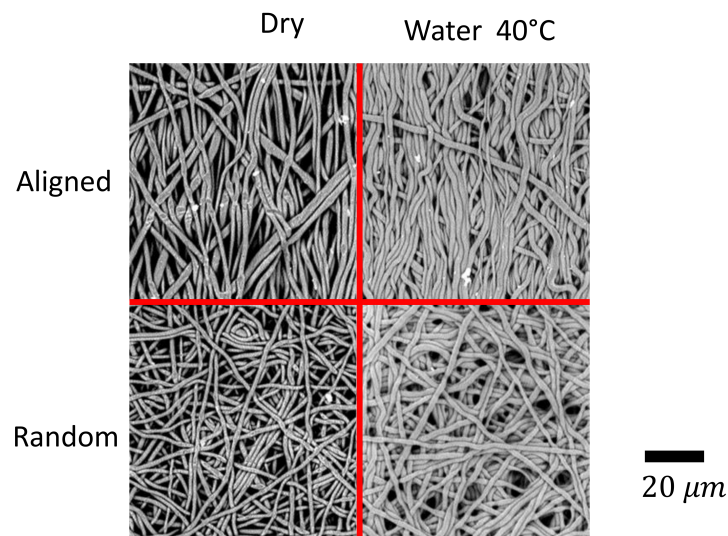


Fig. 1.5 The morphology of Poly(N-isopropyl acrylamide) fibers in aligned and random layers, in dry state and inside water.

on a disc with a rotating speed of 30 *rpm* produces a layer of randomly oriented fibers [109]. In this text for the sake of simplicity, the first and the second layer are referred to as the aligned and the random layer respectively.

As a result of the higher rotating speed of the cylinder, the fibers in the aligned layer are strongly pulled. The fibers of the random layer however are much less stretched hence contain less stored elastic energy. As soon as water flows into the hydrogel, the physical interaction between the fibers decreases. Therefore, they can release the stored energy and relax to a coiled conformation with a shorter length [110]. Assuming the same equilibrium state for all the fibers, the more stretched ones in the aligned layer release more energy, and relax to a shorter length compared to the fibers in the random layer. As a result, when the aligned layer is placed in water, it experiences a noticeable shrinkage,  $\Delta L/L > 30\%$ , along the direction of the fiber alignment, while the random layer collapses only by  $\approx 10\%$  in all directions.

Then the layers are pressed together and photo cross-linked to form a stable bilayer mat which does not decompose when placed in water. The resulting mat can be cut in different angles with respect to the orientation of unidirectional fibers in the aligned layer. In contact with water, within 4 *s* [109], they fold along the unidirectional fibers, and form unique three dimensional structures, see Fig.1.6-a.

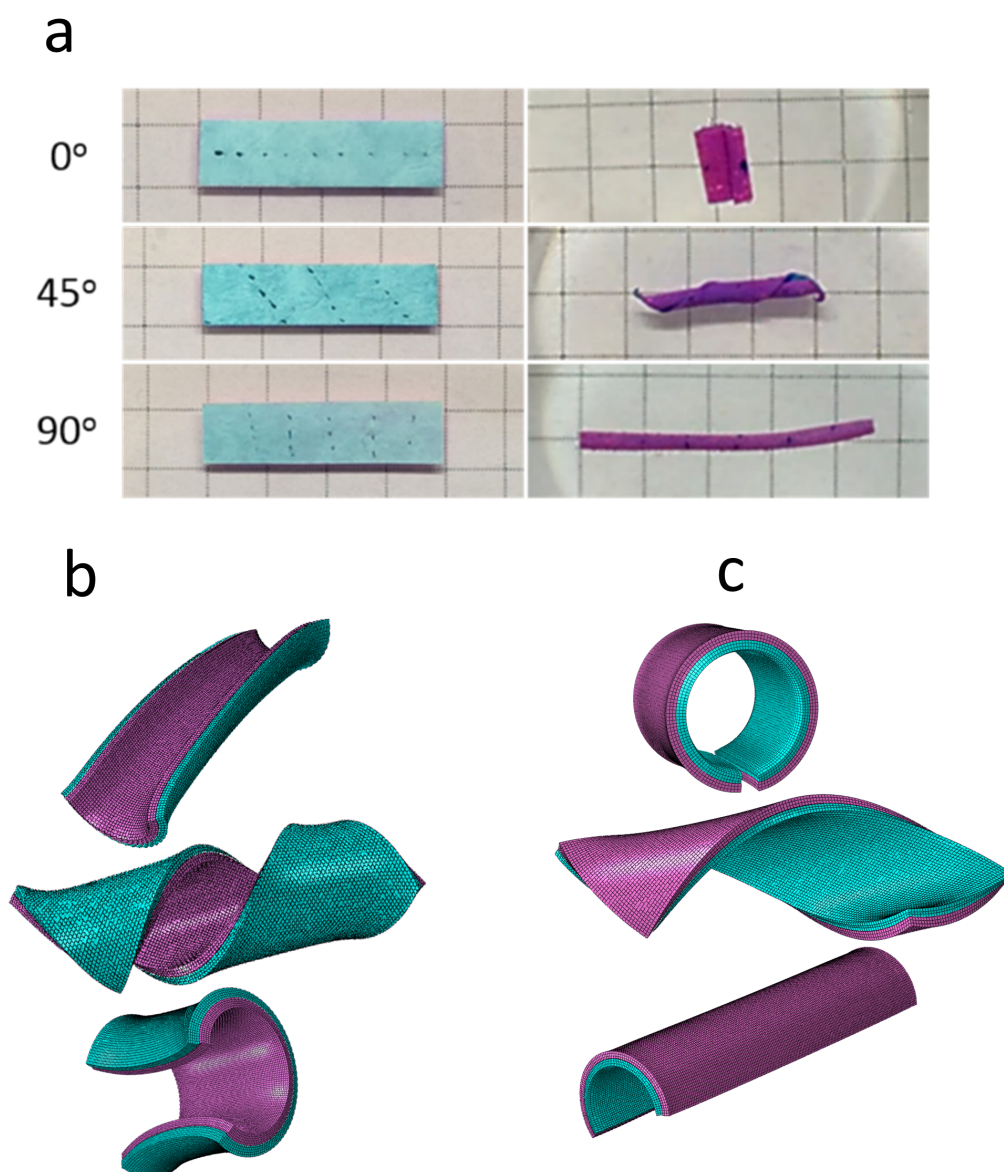


Fig. 1.6 (a) Folding of Bi-PNIPAM-0°, Bi-PNIPAM-45°, Bi-PNIPAM-90° mats (aligned layer (blue)/random layer (pink) (length: 2.0 cm, width: 0.5 cm) with the thickness ratio (aligned/bilayer) of 0.65) in water at 40°C. Fiber alignment direction is indicated by a black dotted line on the dry sample. (b) From top to bottom, the equilibrium shapes of the Bi-PNIPAM-0°, Bi-PNIPAM-45° and Bi-PNIPAM-90° bilayer mats from finite element simulations, with the oversimplifying assumption of an isotropic elastic modulus in both layers. The sizes of the mats are  $800 \times 500 \mu\text{m}$  for Bi-PNIPAM-0° mat, and  $1600 \times 500 \mu\text{m}$  for the 90° and 45°. (c) Equilibrium shapes of the bilayer mats obtained from finite element simulations, using anisotropic expansion coefficients in combination with an anisotropic elastic modulus. To obtain a clear illustration of the bending effects without interpenetration of the mats, the sizes of the mats are chosen as  $1600 \times 500 \mu\text{m}$  for the 0°,  $2000 \times 500 \mu\text{m}$  for the 45° and  $2000 \times 1000 \mu\text{m}$  for the 90° mat. In the simulations, both layers have the equal thickness of  $30 \mu\text{m}$ .

### 1.4.2 Numerical analysis

In order to predict the equilibrium forms of the folded mats, it is not necessary to take into account the complex dynamics of the water flow into the structure. Instead, it is enough to model the macroscopic folding as a static problem. In doing so, many researchers use the Timoshenko's analysis to explain the deformation of the hydrogels [111–116]. This model was originally developed for the thermostats [117]. These devices are composed of two different metal strips with unequal thermal expansion coefficients,  $\alpha_1$  and  $\alpha_2$ , tied to each other on one surface. Therefore, they deform differently in reaction to the same change of temperature. As a result the bilayer bends with a unique curvature which can be calculated using Timoshenko equation:

$$\frac{1}{r_c} = \frac{6(\alpha_1 - \alpha_2)(t - t_0)(1 + m)^2}{H(3(1 + m)^2 + (1 + mn)(m^2 + \frac{1}{mn}))} \quad (1.3)$$

where,  $r_c$  is the equilibrium radius of curvature,  $t$  and  $t_0$  are the current and the initial temperatures of the system respectively,  $H = H_1 + H_2$ ,  $m = \frac{H_1}{H_2}$ ,  $H_1$  and  $H_2$  the thickness of the metal strips,  $n = \frac{E_1}{E_2}$  with  $E_1$  and  $E_2$  as their corresponding Young's moduli [117].

This model considers different one-dimensional changes in the length of each component, resulting in the in-plane folding of the thermostat. Moreover, it assumes that both parts are isotropic. The limitations of these simplifications in modelling the deformations of hydrogels are reported for different systems [118–120]. Here, we show that ignoring the two-dimensional expansion/shrinkage of the layers and the anisotropy of the aligned layer, stemming from the unidirectional orientation of the fibers, will lead to the wrong prediction of the three dimensional foldings of the bilayer hydrogels, see Fig.1.6-a.

Anisotropy of the aligned layer can be observed in the tensile tests of the dry samples. It is shown that, the Young's modulus parallel to the the fibers is on average 50 times larger than the one in the perpendicular direction, i.e.  $\frac{E_{parallel}}{E_{perpendicular}} = 50$ . For the random layer however, isotropy is a valid assumption, and from tensile tests,  $\frac{E_{random}}{E_{parallel}} = 0.6$ . The corresponding experimental data for the wet samples are not available. We show that plugging the dry state experimental results into the numerical simulations of the bilayer hydro-gels, results in the qualitatively correct prediction of the three-dimensional foldings of the hydrogels, Fig.1.6-c.

## 1.5 General conclusion and outlook

This thesis addresses the complex mechanics of two types of polymeric parts which are widely used in modern applications. The first group are individual microcapsules enclosing a liquid core with polymeric shells. The second group are two-dimensional hydrogel mats that fold into unique 3D structures in contact with water.

In chapter two, a combined experimental-numerical approach to mechanical characterization of the deformation and rupture of specific filled microcapsules under axisymmetric compression is presented. The non-linear force-deformation relationship from AFM nano-indentation experiments are reproduced using a finite element analysis assuming a simplified elastic-perfectly plastic model for the capsules mechanical behavior, in agreement with recent works on similar systems. The existence of the following deformation regimes, that can be located in force-deformation graphs are revealed in the numerical analysis: (i) a linearly elastic regime, (ii) a plastic regime in which the stress in the material saturates at a maximum value due to yielding and (iii) a strain-hardening regime in which the stresses rapidly increase again. This work completes the former studies on the mechanical behaviour of similar microcapsule systems by proposing a breakup mechanism that suggests microcapsules rupture in the equatorial region along one (or several) meridian line(s). This result is shown to be consistent with the experimental observations on the broken capsule.

This study particularly provides the industrial collaborators, Henkel AG & Co. KGaA and Follmann GmbH & Co. KG companies, with a detailed understanding of microcapsules mechanical behaviour, in order to optimize their morphology for a more efficient targeted release of the perfume. Additionally, due to the importance of microcapsules mechanical characterization, the results of this research are of interest to other researchers studying new microcapsule systems in the years following its publication [121–127].

In chapter three, for the first time we study the mechanics of such capsules in shear flow. The dynamics and the deformation of capsules subjected to a linear shear flow are extensively studied in recent years. This work contributes by demonstrating the local thinning of the shell, and reporting its possible effect on the breakup of the elastic capsules. More importantly, for the first time, we extend these studies to the capsules with elastic-perfectly plastic shells. In this regard, our work reports on the effects of plasticity and a the strain hardening regime on the deformation of capsules. Furthermore, we study the results of periodic loading-unloading process on their permanent deformed shapes.

The results of this study provide an important starting point for more detailed modeling and analysis of capsules in realistic deformation scenarios. This eventually contributes to the design of novel capsules for complex applications where predicting their deformation

dynamics and breakup are essential for targeted release such as in health products, cosmetics, microfluidics, and drug delivery systems.

In chapter four, a one-component hydrogel mat composed of electro-spun PNIPAM fibers is presented. This novel system that is manufactured as planer mats, forms functional 3D structures in water, which can be used in sophisticated applications such as cell culture and tissue engineering. For such applications, it is of profound importance to study the complex folding process, and to predict and optimize their shape in water.

The finite element analysis demonstrates that aligning PNIPAM fibers in unidirectional fashion creates a hydrogel layer with anisotropic mechanical properties. Moreover, it emphasises the importance of considering this anisotropy in modelling the folding of the bilayer into unique 3D structures in water. These results offer an important starting point for a more comprehensive modelling approaches to address the other aspects of their complex mechanics including the dynamics of folding , and the possible visco-elasticity and the plasticity of the swelling gels, as well as their signal triggered actuation. Moreover, the presented numerical-experimental approach has the potential to address more complex geometries in the field of smart hydrogels, such as bilayers forming closed structures [128] and individual multicomponent core-shell fibers deforming into helices.

## 1.6 Author's contribution

The numerical studies and analyses in all the chapters of this manuscript were accomplished by Ali Ghaemi<sup>1</sup>, under the supervision of Prof. Stephan Gekle<sup>1</sup>. Manufacturing of the studied systems, and the experimental analyses presented in this work were carried out by collaborators from different companies, research institutes, and universities as follows:

In chapter two, the perfume oil was made by Henkel AG & Co. KGaA. This product was encapsulated using Melamine-formaldehyde by Follmann GmbH & Co. KG. Andreas Bauer<sup>2</sup> and Klaus Last<sup>3</sup> provided the filled microcapsules. The experimental part of this study including nano-indentation test, atomic force microscopy of the broken microcapsules, measuring the shell thickness, and the micrographs of the intact and the broken capsules were all carried out in Prof. Andreas Fery<sup>4,5,6</sup>'s group, and were provided by Alexandra Philipp<sup>4,7</sup>.

In chapter four, the manufacturing of the PNIPAM bilayer mats and the experimental analyses were carried out by Li Liu<sup>8</sup> in Prof. Seema Agarwal<sup>8</sup>'s group.

1. Biofluid Simulation and Modeling, Fachbereich Physik, Universität Bayreuth, Universitätsstraße 30, 95440 Bayreuth, Germany

2. Henkel AG & Co. KGaA, Krefeld, Hentrichstr.17-25, 47809 Krefeld, Germany
3. Follmann GmbH & Co. KG, Heinrich Follmann-Straße 1, 32423 Minden, Germany
4. Physikalische Chemie II, Universität Bayreuth, Universitätsstraße 30, 95440 Bayreuth, Germany
5. Institute of Physical Chemistry and Polymer Physics, Leibniz Institut für Polymerforschung Dresden e.V., Hohestraße.6, 01069 Dresden, Germany
6. Technical University of Dresden, Chair for Physical Chemistry of Polymeric Materials, Dresden, Germany
7. Physikalische Chemie I, Universität Bayreuth, Universitätsstraße 30, 95440 Bayreuth, Germany
8. Macromolecular Chemistry II and Bayreuth Center for Colloids and Interfaces, Universität Bayreuth, Universitätsstraße 30, 95440 Bayreuth, Germany

## 1.7 List of our publications in peer reviewed journals

- A. Ghaemi, A. Philipp, A. Bauer, K. Last, A. Fery, and S. Gekle, *Mechanical behaviour of microcapsules and their rupture under compression*, Chemical Engineering Science 142, 236-243 (2016)
- L. Liu, A. Ghaemi, S. Gekle, and S. Agarwal, *One-component dual actuation: Poly (NI-PAM) can actuate to stable 3D forms with reversible size change*, Advanced Materials 28, 9792–9796 (2016)
- A. Ghaemi, and S. Gekle, *Plastic deformation of a microcapsule with finite thickness in shear flow*, to be submitted.

## 1.8 List of conference presentations

Chapters two and four of this thesis were presented and discussed in the following conferences.

### 1.8.1 Oral presentations

- *Mechanical behaviour of microcapsules and their rupture under compression*, A. Ghaemi, A. Philipp, A. Bauer, K. Last, A. Fery and S. Gekle, September 2016, ECIS-2016, Rome, Italy
- *Poly(NIPAM) can actuate to stable 3D forms: A numerical study on one-component dual actuation*, A. Ghaemi, L. Liu, S. Gekle and S. Agarwal, May 2017, E-MRS Spring Meeting, Straßburg, France

### 1.8.2 Poster presentations

- *Mechanical behaviour of microcapsules and their rupture under compression*, I. Melnyk, A. Ghaemi, A. Philipp, A. Bauer, K. Last, A. Fery and S. Gekle, March 2016, DPG Spring Meeting, Regensburg, Germany
- *Mechanical behaviour of microcapsules and their rupture under compression*, A. Ghaemi, A. Philipp, A. Bauer, K. Last, A. Fery and S. Gekle, September 2017, BPS'17, Bayreuth, Germany
- *Poly(NIPAM) can actuate to stable 3D forms: A numerical study on one-component dual actuation*, A. Ghaemi, L. Liu, S. Gekle, and S. Agarwal, March 2017, DPG Spring Meeting, Dresden, Germany



# Chapter 2

## Mechanical behaviour of microcapsules and their rupture under compression<sup>†</sup>

A. Ghaemi<sup>1</sup>, A. Philipp<sup>2,3</sup>, A. Bauer<sup>4</sup>, K. Last<sup>5</sup>, A. Fery<sup>\*,2,6,7</sup>, and S. Gekle<sup>\*,1</sup>

<sup>†</sup> Published as: A. Ghaemi, A. Philipp, A. Bauer, K. Last, A. Fery, and S. Gekle, *Mechanical behaviour of microcapsules and their rupture under compression*, Chemical Engineering Science 142, 236-243 (2016), DOI: 10.1016/j.ces.2015.11.002

1. Biofluid Simulation and Modeling, Fachbereich Physik, Universität Bayreuth, Universitätsstraße 30, 95440 Bayreuth, Germany
2. Henkel AG & Co. KGaA, Krefeld, Hentrichstr.17-25, 47809 Krefeld, Germany
3. Follmann GmbH & Co. KG, Heinrich Follmann-Straße 1, 32423 Minden, Germany
4. Physikalische Chemie II, Universität Bayreuth, Universitätsstraße 30, 95440 Bayreuth, Germany
5. Institute of Physical Chemistry and Polymer Physics, Leibniz Institut für Polymerforschung Dresden e.V., Hohestraße.6, 01069 Dresden, Germany
6. Technical University of Dresden, Chair for Physical Chemistry of Polymeric Materials, Dresden, Germany
7. Physikalische Chemie I, Universität Bayreuth, Universitätsstraße 30, 95440 Bayreuth, Germany

\* Corresponding authors

**Abstract** Understanding the deformation of micro-capsules (MCs) and especially the mechanism of their rupture is of crucial importance for their performance in various applications. Mechanical instability can on the one hand be a failure mechanism, resulting in undesired release, but can on the other hand be used as a release trigger. In this work, finite element analysis together with nano-indentation experiments are applied to characterize the deformation of single filled MCs made of melamin-formaldehyde. The simulations reveal that the capsules undergo different deformation regimes: starting from linear elastic deformation, upon further compression the MCs yield and are plastically deformed. The final step is a strain hardening regime, where the maximum stress rapidly increases till the MCs rupture. Finally, we describe the MCs rupture mechanism obtained from numerical simulation and experimental results. We show that the axial and radial stresses cause significant thinning of the shell at the MC's equator, and that the circumferential stress leads to rupture along the meridians of the MC.

**Keywords:** microcapsule, nanoindentation, plasticity, rupture, finite element analysis simulations

## 2.1 Introduction

Micro-capsules (MCs) are primarily used to encapsulate a gel, solid, or liquid core by a coating shell. There are numerous shell materials that are selected with respect to the chemistry of the core, and the specific functions that MCs are expected to perform. This long list includes gums, starch, cellulose, beeswax, copolymers, resins, lipids, and carbohydrates [129, 130].

MCs have been widely used in a variety of applications such as polymer composites [25], agro-chemicals industry [131], flame retardants [132], perfume containers in washing powders, health products and cosmetics [1], food industry [133], paint coatings [134], building construction materials [135, 136], self healing materials [137], and corrosion inhibitors [138]. Additionally, many researchers consider them as promising candidates for further applications like smart micro-containers [139], magnetically [140, 141], chemically, and mechanically triggered active release [142], biomimetic MCs in drug delivery systems and micro-biotechnology [143–145].

Mechanical behavior of MCs, along with the chemistry of their constituents, and the physical properties of their shell, highly influences their performance. For example in polymer composites, MCs are commonly used to enhance their compression and impact strengths [25]. In biomedical applications, when they are used in cartilage and bone replacements, MCs are expected to endure a high level of compression. In blood vessels where they may function

as drug delivery agents, their stability under shear forces is of main interest [146]. Recent results as well indicate that the mechanical properties of microcapsules influence endocytosis and internalization pathways in a controllable way, offering new opportunities in cellular medicine research and cancer therapy [147]. A review article providing a broader overview of the relevance of microcapsule mechanics and of methods for mechanical characterization of microcapsules can be found in [148].

Understanding the mechanical behavior of MCs, especially their rupture is of crucial importance in order to control the quality of the products and the efficiency of their performance. In this context, single microcapsule experiments are of major importance. Historically, the first single-capsule experiments were carried out on egg cells by Cole in the 1930s by compressing the cells between two parallel plates while monitoring the force as a function of the compression [149]. Recent experiments follow a similar scheme [23–31]: the MCs are placed under a flat or pointed probe that moves toward a stationary metal substrate until the capsule is completely flattened (for highly plastic like phenolic capsules) or crashed (for brittle materials such as glass or carbon). The maximum force experienced by the MC at its burst and the corresponding displacement of the probe can be readily obtained from such experiments. However, in order to complete MCs rupture characterization it is necessary to relate this data to the proper stress and strain distribution in the shell thickness.

Mathematical models have been considered as useful tools to fill this gap. However, the so far proposed analytically tractable models can only describe very simple scenarios which are rarely of practical interest in micro-capsule technology. One example of these models is Reissner's shell theory [38, 39]. This model was originally developed to calculate the displacement of shallow spheres under a point force, but has also successfully been applied for flat probes at small deformations. It has been applied to estimate the compression force of an empty elastic capsule with a very thin shell ( $h/r \ll 0.1$ ) from the displacement of the probe for sufficiently small deformations ( $d/h \ll 0.1$ ) through the following equation:

$$\frac{F}{Ehr} = \frac{4}{\sqrt{3(1-\nu^2)}} \frac{h}{r} \alpha \quad (2.1)$$

where  $F$  is the compression force,  $h$  is the wall thickness of the shell,  $d$  is the displacement,  $r$  is the inner radius of the shell,  $E$  is Young's modulus,  $\nu$  is Poisson's ratio, and ( $\alpha = \frac{d}{2r}$ ) is the fractional displacement.

In fact, a general mathematical model that accounts for the mechanical behavior of a filled MC in larger deformations is not available. This is partly due to the possible complexity of the shell material properties, and the geometrical non-linearity of MC deformation [148].

Numerical analysis such as finite element method offer the opportunity to address such a theoretically complex, nevertheless practically very important problem.

Several researchers have studied the mechanical deformations and the collapse mechanisms of similar spherical systems with dimensions bigger than 0.1 mm ("macro-balloons") under compression. For instance, Lim *et al.* [150] presented experimental results of a single macro-balloon compression together with an appropriate Finite Element analysis to investigate the deformations and the failure of single macro-capsules made of stainless steel. For this analysis they assumed a simple linear elastic model with rate-independent plasticity for the material. These studies inspired further numerical research on the mechanics of smaller systems when the suitable experimental data was available.

In 2007, Carlisle *et al.* [151] used a linear elastic model to predict the burst location of carbon micro-balloons (MBs) with the size of 20  $\mu\text{m}$ . Using this method they concluded that, in contrast to the previous studies which assumed a simple flexural stress to be responsible for the failure of MBs and hence predicted the burst location to be at the equator of the balloon, the failure was most likely to be initiated on the MB's inner wall, directly under the contact region. While considering a completely linear elastic deformation without plasticity is a reasonable choice for carbon as a brittle material, it can not account for the complex deformation of polymeric systems under compression [152].

For instance, in the case of melamine-formaldehyde (MF) capsules, by assuming a linear elastic model, one can get a good agreement with compression test results only for small displacements of the probe ( $d/r < 0.1$ ) [41]. However the prediction of such a simple model deviates dramatically in larger deformations [152, 26, 153]. Therefore, considering plasticity for this system is inevitable.

Recently, for MF capsules, Mercadé-Prieto *et al.* [29] proposed an elastic-perfectly plastic model as the simplest scenario that could predict the compression force versus the displacement of a micromanipulator probe in good agreement with the experimental results. In this analysis the shell material is modeled as a linear elastic solid that yields by further compression. Thereafter, a strain hardening stage is considered to account for the observed increase of stress in larger displacements ( $d/2r > 0.5$ ). Using this model, they concluded that the position of maximum strain, and stress and hence the rupture location is at the equator of the MCs.

In this work, a similar model will be examined for studying the mechanical behavior of a single MC under uniaxial compression. The MCs that are used for this study are particularly made to serve as perfume oil micro containers in washing machine powders. Failure under compression is considered the most likely mechanism of their rupture and the release of their contents.

Rupture due to shear forces would require excessively large flow velocities and/or attachment between the tip of the microcapsules and a second fibre, both of which are unlikely to occur. First, an elastic-perfectly plastic model with suitable parameters will be validated by comparing the Finite Element Method (FEM) simulation results with the relevant nano-indentation experimental data. Finally, their rupture mechanism and its localization will be discussed using the stress profiles at rupture together with corresponding after burst micrographs that clearly show its shape.

## 2.2 Methods

### 2.2.1 Sample preparation and experiments

#### 2.2.1.1 The composition of micro-capsules

The investigated micro-capsules consist of a melamine-formaldehyde (MF) shell and a perfume oil core. The core material was produced by Henkel AG & Co. KGaA (Krefeld, Germany). Then it was encapsulated with MF by Follmann GmbH & Co. KG (Minden, Germany). Two groups of these MCs with four capsules from each group are studied in this work.

#### 2.2.1.2 Nano-indentation experiments

Initially, the MCs were immobilized on a cleaned glass slide (Gerhard Menzel GmbH, Germany) which was coated with a positively charged polyelectrolyte, i.e. polyethylenimine (PEI,  $M_w = 25.000$  g/mol, Sigma Aldrich Co., USA). In this procedure, the glass substrate was covered with an aqueous PEI-solution (1 g/l, 50 mM NaCl) for 20 min. Afterwards, it was rinsed with Millipore water. A sufficiently diluted suspension of micro-capsules was deposited on the PEI-coated glass slide. The non-immobilized MCs were removed by rinsing the sample with Millipore water. Finally, all the samples were dried at room temperature.

Nano-indentation experiments were performed with the MFP nano-indenter (Asylum Research, USA). This device is an atomic force microscope (AFM) based nano-indentation system, where the nano-indenter is completely integrated with the MFP-3D AFM (Asylum Research, USA). For this experiment, the flexure spring (of the nano-indenter module) had a spring constant of  $578.494$  N/m, which was calibrated by the company. Its tip was a sapphire sphere with a diameter of  $800$   $\mu$ m.

Compression experiments on single micro-capsules were performed in dry state. An inverted optical microscope, Axiovert 200 (Carl Zeiss AG, Germany), was combined with

the nano-indenter, in order to place the MC exactly under the probe, and to take micro-graphs before the compression starts. These images were used to measure the outer diameter of the MC. The micro-capsule was then compressed till burst, with the rate of  $1.5 \mu\text{m}/\text{s}$ . The after burst state was also recorded using the optical microscope.

### 2.2.1.3 AFM imaging

Those microcapsules that were already compressed until rupture were imaged with an AFM MFP-3D (Asylum Research, USA) mounted on an inverted optical microscope (Axiovert 200, Carl Zeiss AG, Germany) in intermittent mode in air. Rectangular cantilevers purchased from Atomic Force, Germany (Olympus, OMCL-AC160TS,  $f=300\text{kHz}$ ,  $k=42\text{N/m}$ ) were used. Prior to the imaging measurements, the samples were dried in a vacuum oven for 45 min at  $60^\circ\text{C}$  to remove all perfume oil residues.

## 2.2.2 Finite element simulations

In the experiments, the probe head was much larger than the microcapsule. Therefore, the nano-indentation of the MCs was simulated as the compression of a spherical micro-capsule between two parallel plates, using the finite element software Abaqus 6.14. The schematic set-up of the simulation is shown in Fig.2.1. Here, the probe can only move in  $-Y$  direction, while the substrate has no degree of freedom modelled as "encastre" boundary condition in Abaqus. As a result, the displacement of the probe towards the substrate causes an axisymmetric deformation of the MC.

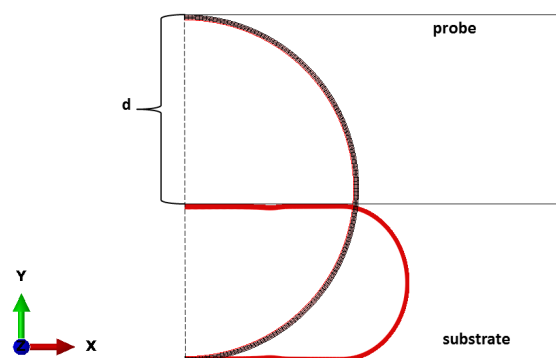


Fig. 2.1 **Schematic diagram of the compression experiment.** Half of the axisymmetric shell is shown at  $t = 0$ , and after the compression resulting from the displacement of the probe towards the fixed substrate, by  $d$ . The dashed line shows the axis of symmetry.

The liquid core of the MC was modeled using the surface-based fluid cavity capability in Abaqus with the density of water at room temperature. Two types of elements were separately used to mesh the shell: 600 CAX4RH (axisymmetric, solid elements, with 4-node bilinear quadrilateral formulation, hybrid with constant pressure, and reduced integration with hourglass control) and 150 SAX1 (2-node linear axisymmetric shell elements), and the results of simulations were compared. The probe and the substrate were both modeled as analytical rigid surfaces. The interactions between them and the MC were assumed to be frictionless contacts.

The material of the shell was modeled as a polymer with elastic-perfectly plastic properties, i.e., a linear elastic material with a Young's modulus  $E$  followed by a plastic regime. At the end, a linear increase in stress was considered for the strain hardening part. This model, which very well reproduces the experimental results, contains the following parameters:

$h$ : The wall thickness of the shell.

$r$ : The inner radius of the shell.

$E$ : Young's modulus.

$\nu$ : Poisson's Ratio

$\sigma_y$ : Von Mises yield Stress.

$\epsilon_H$ : Hencky hardening strain, and  $\sigma_H$ : Hencky hardening stress.

$\epsilon_B$ : Hencky breaking or rupture strain, and  $\sigma_B$ : Hencky rupture stress.

For simplicity, MCs were considered to be incompressible with  $\nu = 0.5$ . The effect of choosing different values of  $\nu$  is discussed in the supplementary material. The capsule radius and wall thickness were directly taken from the measurements. For each MC, the values of  $E$  were set in such a way that the calculated compression force versus probe displacement (F-d) could match the elastic part of the MC compression data. The rest of the parameters were set manually till the best fitting with the experimental results was achieved.

The results of FEM analysis were numerically validated using different levels of refinements for each element type, see the supplementary information part for further details.

## 2.3 Results and Discussion

### 2.3.1 Geometrical characterization

The diameters of studied microcapsules are listed in table.2.1.

MC sample	Diameter ( $\mu m$ )
A1	14.3
A2	12.5
A3	14.1
A4	16.1
B1	12.2
B2	13.8
B3	12.9
B4	13.5

Table 2.1 The analyzed MCs with their diameters measured from light micro-graphs.

### 2.3.2 Wall thickness characterization

Two examples of the AFM height contours that were used to determine the shell wall thicknesses are illustrated in Fig.2.2. These measurements are performed after drying already ruptured samples, and the V-shaped burst can be clearly seen in both images. The corresponding height profiles of the marked cross-sections are shown at the bottom of this figure. Using these profiles, the wall thickness is calculated as the half of the measured height of the flat part. For capsules from group A we find an average thickness of 190nm while for capsules from group B we find 140nm. As these thicknesses were determined after drying, the actual ones during the compression may slightly deviate from these values due to de-swelling of the shell.

### 2.3.3 AFM compression experiments

The results of uniaxial compression experiments for all the analyzed samples are shown in Fig.2.3. In this figure, the measured compression force is plotted against the displacement of the nano-indenter probe. In accordance with previous studies on similar systems [29, 26, 152, 30], all of these graphs share three main features. First, compression leads to an initial steep increase of force, which is then followed by a plateau region, after which the force continuously increases till the MC ruptures. The measured rupture forces of these capsules are also comparable to those values reported in literature (e.g. [23, 29]). Characterizing different parts of these force-displacement (F-d) graphs sheds light on the complex mechanical behavior of MCs under uniaxial load.

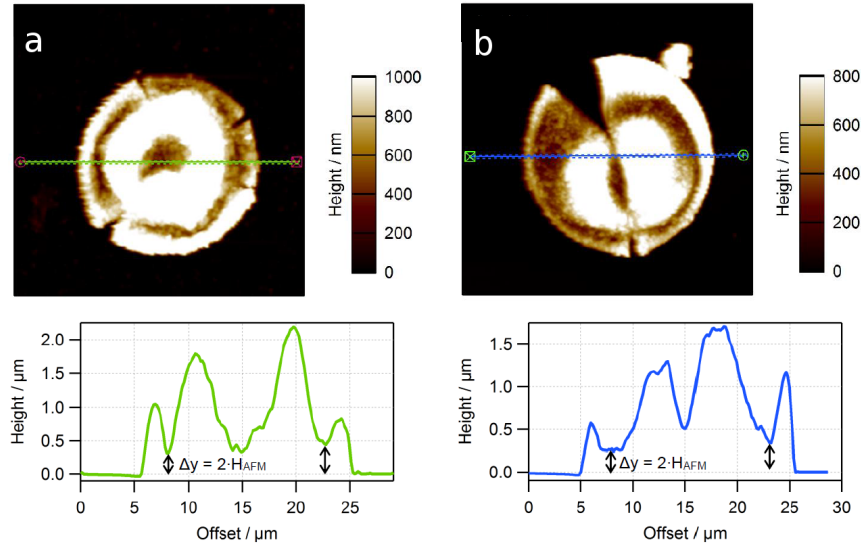


Fig. 2.2 **Measurement of the MC wall thickness using AFM imaging.** Top (a),(b): The AFM height contours of ruptured micro-capsules from groups A and B, respectively, with marked cross sections (green and blue lines). Bottom: the corresponding height profiles of the marked cross sections. All images have a size of  $30 \mu\text{m} \times 30 \mu\text{m}$ .

### 2.3.4 FEM simulations

FEM simulations can bridge the gap between the results of nano-indentation experiments and the mechanical parameters that are useful for characterizing different types of deformations which the MCs go through during compression tests.

The result from one of the FEM simulations considering the mentioned elastic-perfectly plastic model is compared to the corresponding experimental output for an exemplary MC, A2, in Fig.2.4. The success of the proposed model in reproducing the nano-indentation results is clearly demonstrated (Very good agreements were also achieved for the rest of the studied capsules, see the supplementary information for more details). Furthermore, the characteristic features of the F-d graph can now be related to the deformation regimes, i.e. linear elastic, plastic, and strain hardening part. In the elastic regime, the energy of deformation which can be estimated from the area under the F-d curve, is the smallest because yielding happens at very small displacements  $d/2r < 0.1$ , and the maximum force that is measured in this regime is also very small compared to the maximum force applied at the end of compression, i.e.  $F_{yield}/F_{burst} < 0.025$ . Accordingly, the whole energy of rupturing is mainly distributed between the plastic regime and the strain hardening part.

In each of the compression tests, different parts of the MC undergo multi-axial deformations. As a result, different components of the corresponding stress tensor are non-zero. In

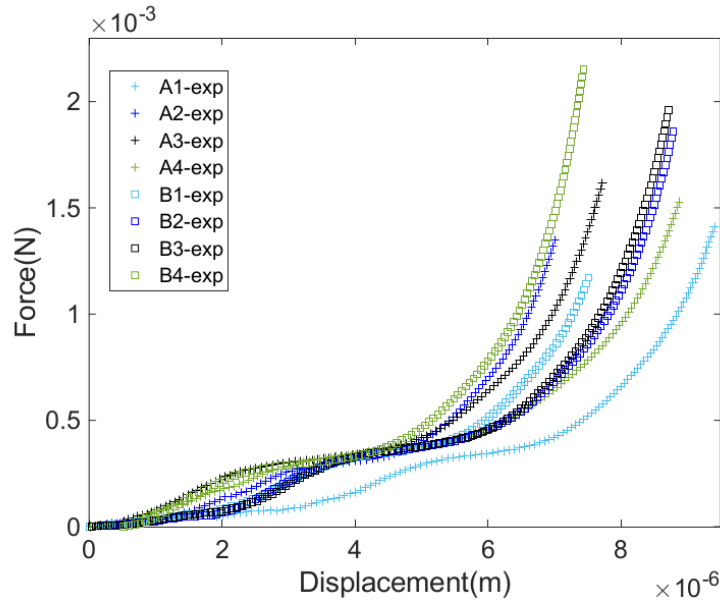


Fig. 2.3 **Force-displacement experimental results for all the analyzed samples.** The measured force ( $N$ ) against the displacement of AFM probe ( $m$ ) are plotted for all the analyzed samples.

such situations, the Von Mises yield criterion is very useful in characterizing the yielding of the plastic material. In this analysis, the object yields when the maximum equivalent stress exceeds  $\sigma_y$ . The distribution of Von Mises stress in the shell thickness of the same MC in different deformation regimes is shown in Fig.2.5.

Starting from  $d = 0$ , first the linear elastic deformation takes place. In this regime, the maximum Von Mises stress happens at the outer surface of the shell in the contact areas between the MC and the plates, see Fig.2.5(a). Thereafter, when  $\sigma_{max} = \sigma_y$ , the MC goes through plastic deformation, which is illustrated for  $d = 1.5 \mu m$  in Fig.2.5(b). Here, the position of  $\sigma_{max}$  moves to the inner surface of the shell, away from the plates, and stays there till the start of the hardening. Besides, the value of  $\sigma_{max}$  remains constant and equal to  $\sigma_y$  which is the characteristic of plastic behavior. Hardening starts at  $d \approx 5 \mu m$  and the stress distribution is illustrated in Fig.2.5(c). Hardening continues till  $d = 7.02 \mu m$  which is the maximum displacement of the probe before the MC ruptures. Meanwhile, the position of  $\sigma_{max}$  moves toward the equator of the capsule while its magnitude approaches  $\sigma_B$  which is the maximum stress at burst, see Fig.2.5(d).

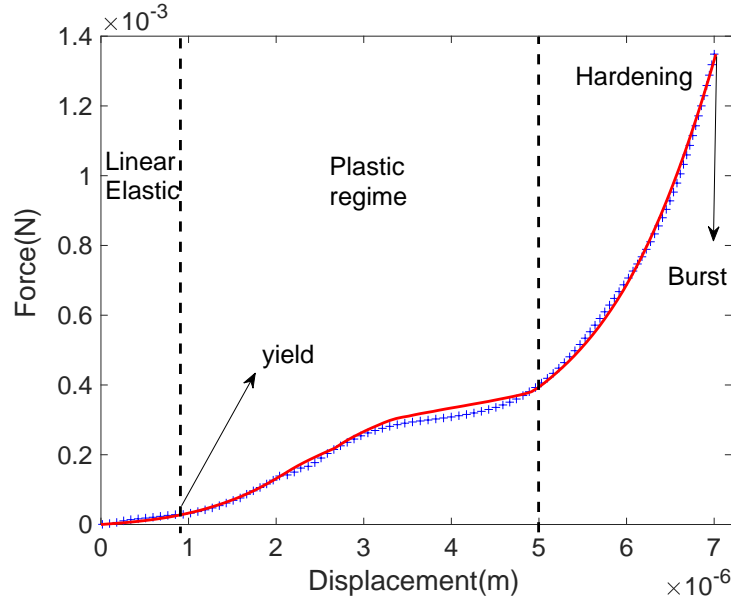


Fig. 2.4 Comparison between numerical and experimental results, and characterization of the force-displacement data for the MC, A2, with  $r = 6.25 \mu\text{m}$ . The measured force against the displacement of the AFM probe is shown in blue and the corresponding FEM simulation result is plotted in red. Different regimes of deformation are separated by dashed lines.

### 2.3.5 Characterization of micro-capsule rupture

The left side of Fig.2.6-(a) and Fig.2.6-(b) show micro-graphs of two MCs before the compression starts. By comparing the after burst images, Fig.2.6-right, one can recognize the plastic deformation of the MCs during which they are irreversibly flattened under compression. Furthermore, the burst locations for both MCs are clearly observable in these images. In this figure, the V-shape ruptures of the MCs indicate that the direction of rupture is parallel to the axis of the compression.

In order to explain the rupturing mechanism and to predict its location, it is appropriate to have a closer look at the distribution contours of all the normal and shear stresses just before the rupture point. Fig.2.7-(a) shows that, parallel to the  $X$  axis, the maximum magnitudes of  $\sigma_{XX}$  have positive values and occur at the inner surface of the MC. This indicates that in this location the MC is stretched parallel to  $X$  axis. At the equator, however,  $\sigma_{XX}$  has a negative sign, resulting in the compression of the MC wall in this position. The maximum of  $\sigma_{YY}$ , on the other hand, occurs at the equator, and its value is positive, which causes the stretching of the shell parallel to  $Y$  axis, see Fig.2.7-(b). These normal stresses at the equator, in both  $X$  and  $Y$  directions cause the noticeable thinning of the shell in this location ( $\Delta h/h_0 > 23\%$ ), see Fig.2.8. The distribution of shear stress in the thickness of the shell wall is shown in

Fig.2.7-(c). Because of the symmetry of deformation with respect to the equator, the sign of the shear stresses in the upper part is opposite to the one in the lower part and its magnitude is equal to zero at the equator. Additionally, the maximum magnitude of shear stress is less than 50% of the maximum magnitudes of the normal ones, and hence the deformation of MC in this regime is mainly influenced by normal stresses. Finally, Fig.2.7-(d) shows that the maximum value of the circumferential stress,  $\sigma_{\theta\theta}$ , exceeds the magnitude of all the other normal stresses by roughly 50%. The large value of  $\sigma_{\theta\theta}$  can be attributed to the incompressibility of the liquid core which is put under pressure by the compression from the top. This stress, with a positive sign, causes the circumferential stretching of the MC wall at its equator, and most likely leads to the rupture of the wall in the direction parallel to the axis of compression. This conclusion is in full agreement with the after burst micro-graphs in Fig.2.6 which show that the MCs rupture along their meridians.

## 2.4 Conclusion

In this work, a combined experimental-numerical characterization of the deformation and rupture of oil-filled melanine-formaldehyde micro-capsules under axisymmetric compression was presented. We showed that the force-deformation curves from AFM nano-indentation experiments can be accurately reproduced using a finite element analysis assuming a simplified elastic-perfectly plastic model for the capsules mechanical behavior in agreement with recent work on similar capsules [26, 29]. The corresponding simulations revealed the existence of three deformation regimes, that could be located in F-d graphs: (i) a linearly elastic regime (approximately for  $0 < d/2r < 0.1$ ), (ii) a plastic regime in which the stress in the material saturates at a maximum value due to yielding (approximately for  $0.1 < d/2r < 0.4$ ) and (iii) a strain-hardening regime in which the stresses rapidly increase again. Individual micro-capsules taken from the same batch of an industrial-scale production process showed rather large variations in their corresponding behavior, see Fig.2.3. Importantly, despite these variations, all the micro-capsules were found to rupture in the equatorial region along one (or several) meridian line(s). This behavior was obtained consistently from the mechanical tests using the optical micro-graphs of the MCs after rupture and the FEM simulations which showed that, at burst, the shell of the MC gets thinner at the equator, by roughly 20% as shown in Fig.2.8, and the circumferential stress around the equator exceeds all the other stresses in shell by roughly 50%.

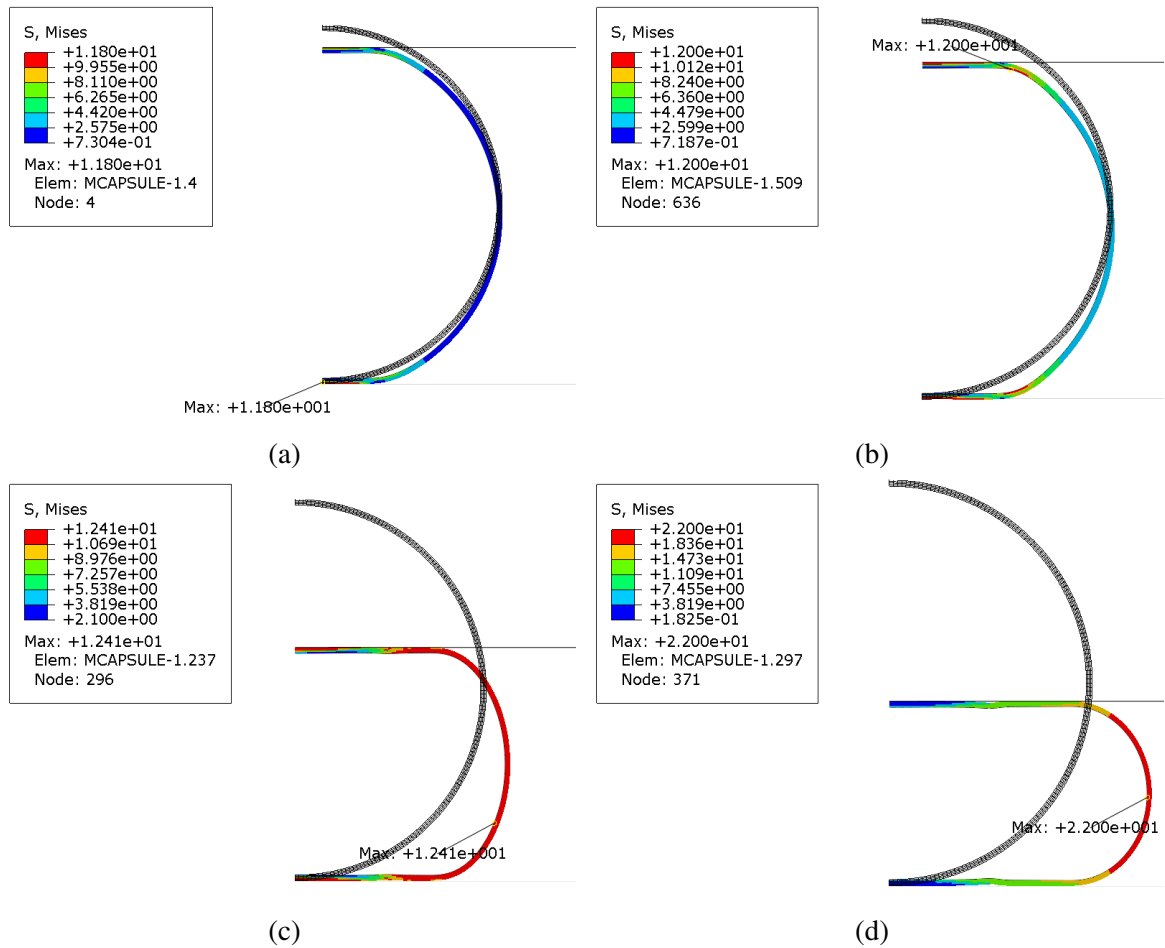
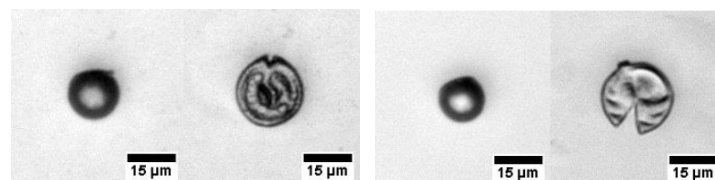


Fig. 2.5 **Von Mises stress distribution at different displacements.** (a) The stress distribution after the displacement of the probe by  $0.8 \mu\text{m}$  ( $d/2r = 6.4\%$ ), which results in fully elastic deformation of MC (b) The plastic regime at  $d = 1.5 \mu\text{m}$  ( $d/2r = 12\%$ ) where  $\sigma_{max} = \sigma_Y$  and remains constant. (c) The beginning of the strain hardening at roughly  $d = 5 \mu\text{m}$  ( $d/2r = 40\%$ ) that leads to an increase of  $\sigma_{max}$ . (d) The proximity of rupture ( $d/2r = 56.2\%$ ) where  $\sigma_{max}$  occurs at the equator. The units of Von Mises stresses are  $100 \text{ MPa} = 10^8 \text{ Pa}$ . The undeformed state is shown in black.



(a) Microcapsule from group A (b) Microcapsule from group B

Fig. 2.6 **Light micro-graphs of MCs before and after rupturing.** On the left side: The micrographs of intact MCs before compression. On the right side: The micro-graphs of ruptured micro-capsules.

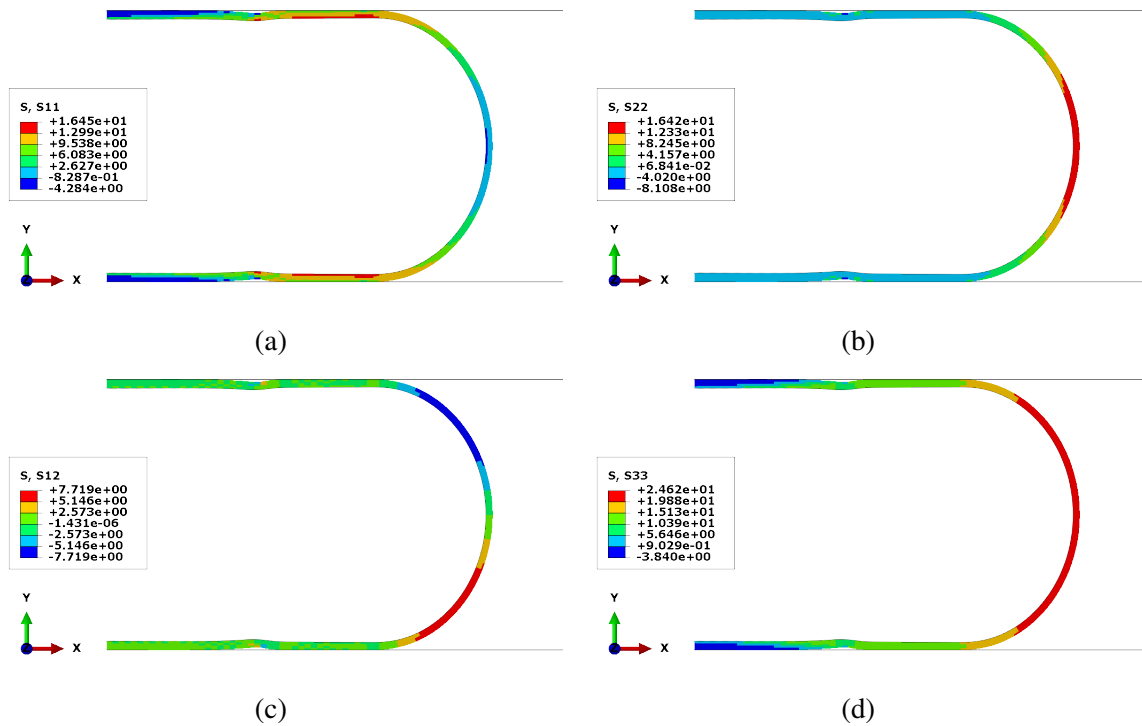


Fig. 2.7 **Distribution of stress tensor components at burst.** (a) Normal stress perpendicular to the axis of compression ( $S11 = \sigma_{xx}$ ). (b) Normal stress parallel to the axis of compression ( $S22 = \sigma_{yy}$ ). (c) Shear stress inside the thickness of the shell ( $S12$ ). (d) Normal out-of-plane (circumferential) stress ( $S33 = \sigma_{zz}$ ). For the cut through the  $z=0$  plane shown here, the components of the stress tensor in Cartesian coordinates,  $\sigma_{xx}$ ,  $\sigma_{yy}$ ,  $\sigma_{zz}$  correspond to radial ( $\sigma_{rr}$ ), axial ( $\sigma_{zz}$ ) and circumferential ( $\sigma_{\phi\phi}$ ) stresses in cylindrical coordinates, respectively. The units of all illustrated stresses are  $100 \text{ MPa} = 10^8 \text{ Pa}$ .



Fig. 2.8 **Distribution of shell thickness at rupture.** The thickness of the shell in different locations, at the maximum displacement of the probe. The shell is meshed with SAX1 elements, and the minimum is located at the equator of the MC. The unit of length is  $\mu\text{m}$ .

## Acknowledgment

A. G. and S. G. would like to thank the Volkswagen Foundation for financial support.

## 2.5 Supplementary information

### FEM simulations for all eight micro-capsules

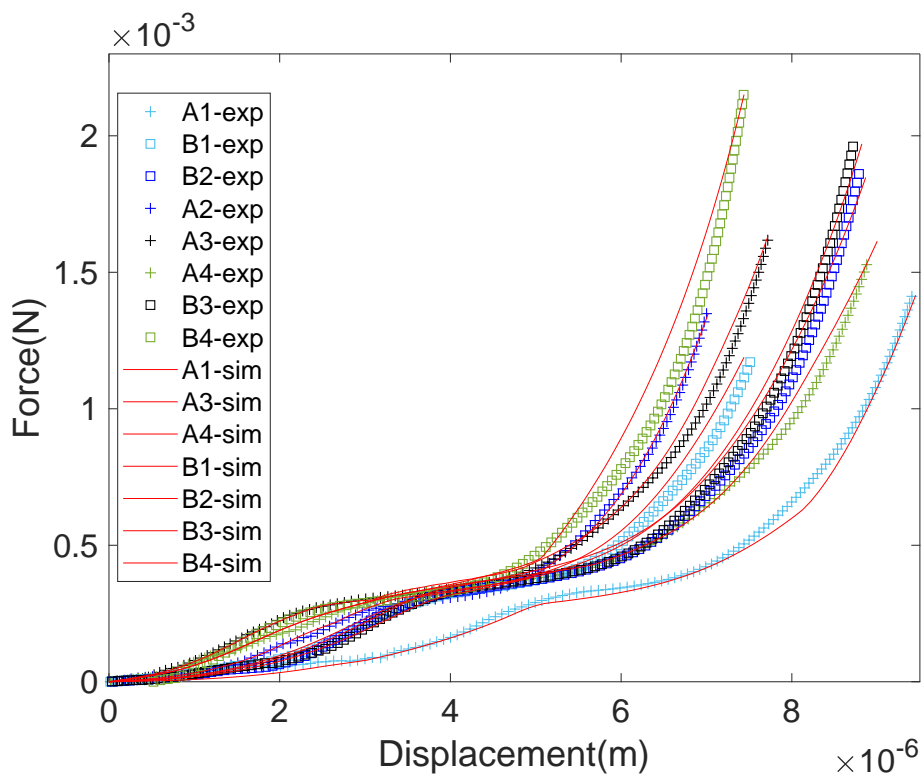


Fig. 2.9 **Comparison between numerical and experimental results.** Agreement between FEM simulations shown with red lines and the measured force-displacement results represented by colorful symbols for eight investigated micro-capsules.

Fig.2.9 demonstrates the agreement between the predictions of the proposed elastic-fully plastic model and the experimental data for all the studied samples.

## Grid independence analysis

Fig.2.10 illustrates the validity of the presented FEM analysis using CAX4HR elements by showing the agreement between the numerical results from simulations that use different levels of grid refinement.

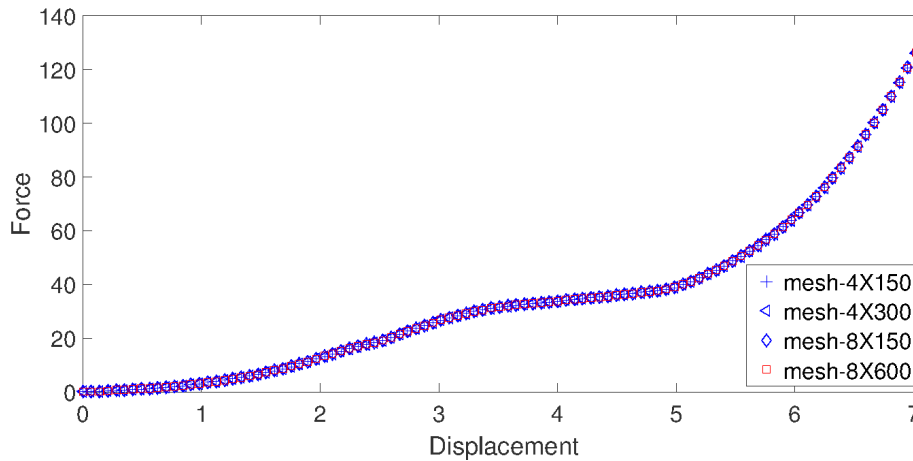


Fig. 2.10 **Grid independence studies for an exemplary MC.** The force ( $10 \mu N$ ) against displacement ( $\mu m$ ) is calculated using the grids composed of CAX4HR elements with different levels of refinement:  $4 \times 150$ ,  $4 \times 300$ ,  $8 \times 150$  and  $8 \times 600$  elements.

Fig.2.11 shows the Von Mises stress distribution in the thickness of the shell of an MC that is meshed by solid elements with two levels of refinements. The values of  $\sigma_{VM}$ , as well as their locations are in full agreement in both simulations.

MC sample	Diameter ( $\mu m$ )	E (GPa)	$\sigma_y$ (Mpa)	$\sigma_B$ (Mpa)	$\epsilon_B$
A1	14.3	0.9	86	132	0.37
A2	12.5	3	120	228	0.26
A3	14.1	9	120	236	0.29
A4	16.1	8	110	203	0.29
B1	12.2	3	150	190	0.40
B2	13.8	3	150	223	0.25
B3	12.9	2.	140	235	0.44
B4	13.5	28	170	544	0.22

Table 2.2 The analyzed MCs, with the measured diameters, and their estimated mechanical properties from FEM analysis.

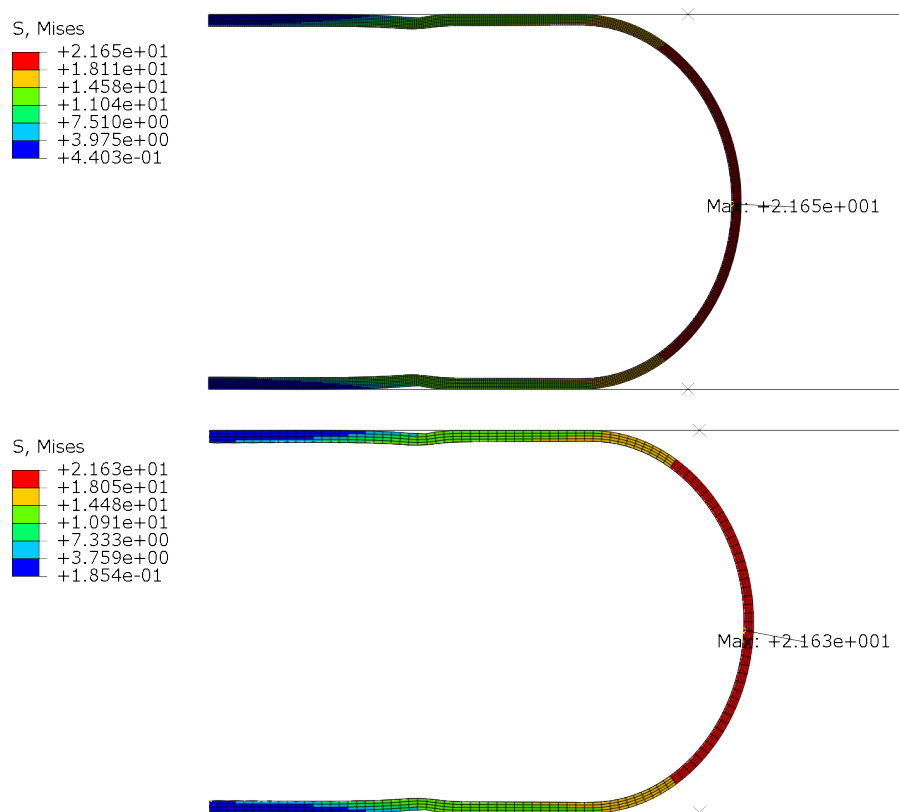


Fig. 2.11 **Grid independence studies on the distribution of Von Mises stress.** The distribution of Von Mises stress at the burst point of an exemplary micro-capsule that is meshed with different levels of refinement.

## FEM simulations with shell elements

In FEM analysis, choosing SAX1 shell elements over CAX4HR type results in faster calculations and more computational efficiency in simulating the whole range of deformations. Additionally, the final results show an acceptable agreement with those simulations that use solid elements, see Fig.2.12.

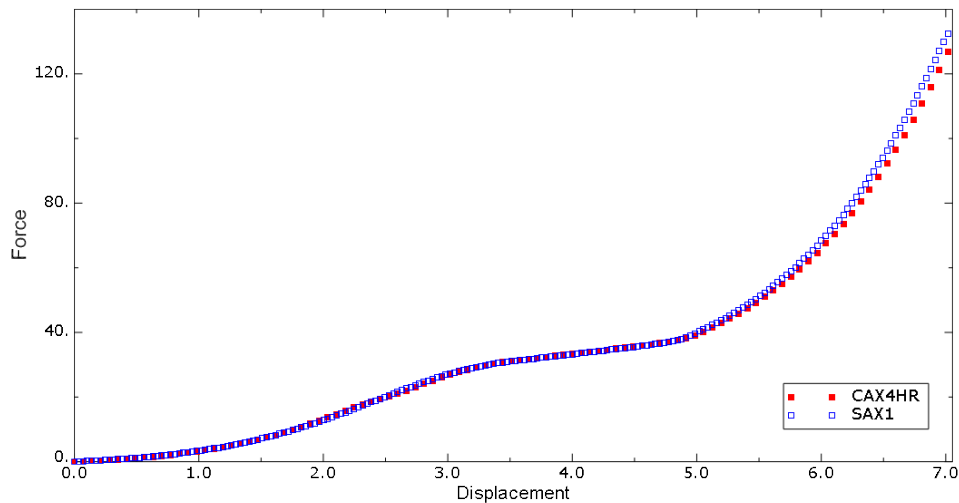


Fig. 2.12 **Numerical results using SAX1, and CAX4HR element types.** Numerical force-displacement results, using SAX1 shell elements, plotted by blue empty squares, and using CAX4HR solid elements, shown by red filled squares. The units of force and displacement are ( $10\mu N$ ), and ( $\mu m$ ) respectively.

Using shell elements is also more convenient to measure the variations of thickness. Nevertheless, the analysis using SAX1 type elements can not be applied to calculate shear stress and strain, neither can it provide the details of any stress or strain distribution in the thickness of the shell wall.

### Influence of Poisson's ratio

The effect of choosing different Poisson ratios ( $\nu$ ) on the mechanical behavior of MCs, under compression is addressed by comparing the force-displacement graphs of one exemplary MC, and considering three different values of  $\nu$ , see Fig.2.13. In accordance with previous studies [29], changing of  $\nu$  does not lead to a significant difference in the mechanical behavior of MCs during the elastic deformation [41]. Additionally, we found that even in further displacements, there is still an acceptable agreement between the results of the three simulations.

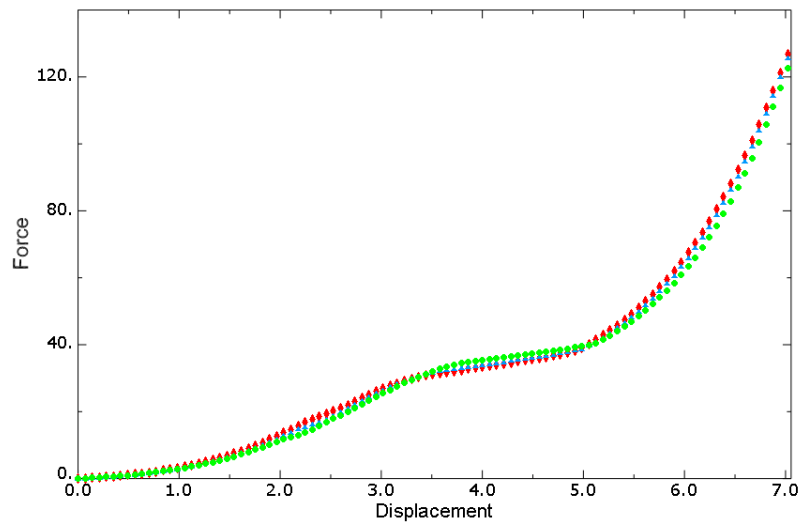


Fig. 2.13 **The effect of Poisson ratio on MCs mechanical behavior.** Numerical force-displacement results for the same sample, using  $\nu = 0.5$  in filled red diamonds,  $\nu = 0.33$  shown by filled blue triangles, and  $\nu = 0.01$  in green filled circles. The units of force and displacement are ( $10 \mu N$ ), and ( $\mu m$ ) respectively.



# Chapter 3

## Plastic deformations of microcapsules with finite thicknesses in shear flow<sup>†</sup>

Ali Ghaemi<sup>a,\*</sup>, Stephan Gekle<sup>a,\*</sup>

<sup>†</sup> To be submitted

<sup>a</sup> Biofluid Simulation and Modeling, Theoretische Physik, Universität Bayreuth, Universitätsstraße 30,  
95440 Bayreuth, Germany

\* Corresponding authors

**Abstract** Understanding deformation and breakup of artificial microcapsules by external force is essential for knowledge guided design of novel capsule materials. In many applications, e.g. microcapsules in washing powder, break up is induced via shear stresses exerted by an external liquid flow. Here, we present a computational investigation on the dynamic breakup of microcapsules in a generic shear flow which includes (i) the finite thickness of the capsule shell and (ii) its plastic deformation. We find that, if shear rates are high enough to induce plastic deformations, the elongation of the capsule is larger than its elastic counterpart. Depending on the plasticity ratio of the shell, the capsule reaches a steady shape or breaks up. Using detailed stress distributions in the shell right before the onset of plasticity, we show that the parts of the shell to yield first are located near the inner edge around the equator and at the outer edge in the poles of the deformed capsule. Finally, we find that if plastic deformation is followed by a hardening regime as has been observed for microcapsules using static AFM-based measurements, deformation rate decreases and the breakup can be significantly delayed or even prevented completely.

### 3.1 Introduction

Artificial capsules are composed of a liquid or gel core enclosed by a solid, usually stretchable membrane [154]. They exist in a wide range of sizes from micro- up to a few millimetres and are used in a variety of applications. Microcapsules with radii  $R = 1 - 100 \mu m$ , for instance, have evolved into established components of polymer composites [155], agro-chemicals industry [156], flame retardants [157], cosmetics [158], perfume containers in washing powders. Furthermore, they are studied as promising candidates for drug delivery systems where they are internalized by living cells [159]. From a more fundamental perspective, microcapsules can serve as model system for the biological cells or eggs [160].

For many of these applications, the mechanical properties of the shell are essential for the final performance of the capsules, e.g. during controlled release of the capsule's contents via shell breakup. Theoretically, the mechanical behavior of capsules has been mostly simplified to that of an elastic shell enclosing a liquid core [161, 154]. However, many of the capsules used in industrial applications show more sophisticated properties requiring more complex material constitutive models [162, 26, 29, 153, 44]. Previously, we and others showed that an elastic-fully plastic model with a final strain hardening can accurately reproduce the nano-indentation test results of melamine formaldehyde microcapsules [26, 32]. Moreover using stress distribution maps it was possible to explain the MCs collapse mechanism and to predict approximately the position and the shape of breakup in full agreement with experimental data [32].

One of the many conditions in which the capsules are deformed and eventually break up is when they are immersed in a shear flow as occurring in microfluidic devices, during washing cycles or inside blood vessels and rheometers. The nonlinear deformation of isolated 2D and 3D capsules with an elastic shell in flow has been extensively studied by many researchers experimentally [163, 104, 164, 160] as well as theoretically-numerically [65–92], see also the review articles [64, 93]. For an infinitesimally thin capsule enclosing a Newtonian fluid, the deformation dynamics depends on three dimensionless parameters: (i) the Reynolds number  $Re = \frac{V^\infty \rho d}{\mu_{out}}$ , (ii) the viscosity ratio between inside and outside fluids  $\frac{\mu_{in}}{\mu_{out}}$ , and (iii) the capillary number  $Ca_v = \frac{\mu_{out} \dot{\gamma}}{G}$  where  $\dot{\gamma}$  is the linear shear rate under which the capsule deforms, and  $G$  is the bulk shear modulus of the shell [64]. The first two parameters are determined solely by the properties of the flow and the fluid domain, while the last one is also affected by the mechanical behavior of the capsule. The majority of the corresponding research, consider the capsules to have infinitesimally thin shells and the mechanical properties to be fully elastic. While the former simplification has been lifted and walls with an effectively finite thickness have been studied recently by [103], plastic deformation of microcapsules due to shear flow has not been studied to date.

Here we overcome these limitations by numerically studying a capsule with a truly finite shell thickness that can change in response to the flow and which, for large deformations, exhibits plasticity. The applied material model is consistent with the mechanical behavior extracted from nano-indentation experiments of commercially available microcapsules [32]. When starting from a spherical rest shape, plastic deformation sets in simultaneously near the inner edge of the shell in a region around the equator and at the outer edge near the poles. At long times, plastic capsules exhibit two different types of behavior: at moderate to high plasticity ratios, the capsules reach a steady ellipsoidal shape similar to their purely elastic counterparts (but more elongated). At low plasticity ratios, capsules elongate faster and eventually can breakup under shear. We furthermore present a detailed analysis of stress distribution maps in the thickness of the shell and finally discuss the effect of periodic shear flows.

## 3.2 Methods

In our simulation setup, we consider a 2D capsule with radius  $R$ , measured from the outer surface of the capsule, and a finite wall thickness  $H$ . An elastic-perfectly plastic constitutive law is assumed to account for the mechanical behavior of the shell. The elastic part of deformation is described by the generalized Hookean law for an isotropic material with elastic modulus  $E$ . For a homogeneous and isotropic material, shear and bulk moduli are

related through  $G = \frac{E}{2(1+\nu)}$  with the Poisson ratio  $\nu$ . For the plastic part the von Mises criterion is applied with the yield stress  $\sigma_y$  above which the plastic deformation sets in. Moreover, the shell is assumed to be incompressible with a Poisson ratio  $\nu = 0.48$ .

The capsule is immersed in a Newtonian fluid between two parallel plates such that the distance between its center and each of the plates is  $D$ . The physical properties of the fluid inside and outside the capsule are identical:  $\frac{\rho_{in}}{\rho_{out}} = 1.0$ ,  $\frac{\mu_{in}}{\mu_{out}} = 1.0$ , where  $\rho$  is the density and  $\mu$  is the dynamic viscosity of the fluid. The linear shear flow is established by assigning constant velocity  $\pm V$  to the upper and lower plate, respectively, leading to a shear rate  $\dot{\gamma} = \frac{V}{D}$ . The following dimensionless quantities are considered:  $\frac{D}{R} = 10$ ,  $0.05 < \frac{H}{R} < 0.2$ ,  $Re \ll 1.0$ .

Our model is solved in Abaqus-2016. The shell is meshed with C3D8R elements and the Newtonian fluid is simulated as a  $2D \times 2D$  Eulerian domain and is discretized with EC3D8R elements. The integration is carried out using the Gaussian quadrature rule under reduced mode. The Mie-Grüneisen equation of state is considered to complete the material definition for the Eulerian part. This equation determines the volumetric strength of the fluid and is used to calculate the pressure as a function of the density and the specific energy [40]. The sound velocity in the fluid is taken as  $V_c = 1500 \text{ m.s}^{-1}$  and thus much larger than the imposed shear flow velocities leading to an essentially incompressible fluid. Since the whole problem is in two dimensions, a  $z$ -symmetry boundary condition is used. Free inflow/outflow boundary conditions are applied to the left and right edges, respectively, in order to allow for the non-obstructed flow of the fluid along the  $x$  axis. No other constraints are applied to the deformable capsule or the fluid. The interaction between the capsule and the fluid is computed via an enhanced immersed boundary method implemented in Abaqus. In order to account for the presence of the core fluid and thus to keep the enclosed area constant during the deformation of the capsule a fluid cavity boundary condition is applied to its inner surface. The results of the simulations are compared for different grid resolutions and the mesh independent results are reported. For the elastic shells the dimensionless size of the elements to achieve mesh independent results are  $L = \frac{I}{H} = 0.25$ , where  $I$  is the distance between the adjacent nodes of the hexagonal elements as shown in Fig.3.8. For the plastic shells however, the required element size is 0.125 as shown in Fig.3.9.

### 3.3 Results and Discussion

In this section we start by benchmarking our simulations on initially circular elastic capsules with a finite wall thickness in a linear shear flow by comparing with earlier studies. Thereafter, the local thinning of the capsule shell is demonstrated and explained using stress distribution maps in the thickness of the shell. We then proceed to study the beginning of plastic

deformation, the effect of plasticity on the deformation of the capsules and consider how a strain-hardening before breakup may change the dynamics of capsules. Finally, we offer an analysis of their deformations under periodic shear flows, and their final shape and rupture in such scenarios.

In the following, we will use the label *Elastic(or)Plastic* –  $Y_x$  –  $H_z$  to name an elastic or elastic-fully-plastic capsule with the plasticity ratio  $x = \frac{\sigma_y}{E}$ , and the thickness ratio of  $z = \frac{H}{R}$ . Shear rates are mentioned using the non-dimensional capillary number  $Ca_v = \frac{\mu\dot{\gamma}}{E}$ .

### 3.3.1 Elastic capsules with finite wall thickness

Many former studies [64] show that under linear shear flow an originally circular or spherical capsule deforms into an ellipse or an ellipsoid, respectively, as illustrated Fig.3.1-a. During this deformation, the Taylor parameter  $D_{12} = \frac{R_a - R_c}{R_a + R_c}$ , where  $R_a$  and  $R_c$  are the main radii of the ellipse, constantly increases till it reaches an equilibrium value  $D_{12}^\infty$  as shown in Fig.3.1-b. The magnitude of  $D_{12}^\infty$  depends on shell thickness, fluid properties, the applied shear rate, and the mechanical properties of the shell. During the deformation, the shear flow exerts force on the freely immersed capsule. Consequently, the capsule inclines and the angle between its long axis and the direction of the flow ( $\phi$ ) decreases as shown in Fig.3.1-c. The steady ellipse then starts the well-known tank-treading motion. This general behavior has been thoroughly studied and consistently reported both analytically and numerically in the case of infinitesimally thin elastic capsules.

#### 3.3.1.1 Deformation dynamics

In the limit of small thickness ratios  $\frac{H}{R}$ , our results are expected to match with earlier studies on 2D capsules with infinitely thin shells [89] under similar conditions. The relevant dimensionless quantities for a 2D capsule with infinitely thin shell are [89]: (i)  $\alpha = \frac{\mu\dot{\gamma}r}{E_2}$  where  $E_2$  is the interfacial elasticity modulus and (ii)  $E_b = \frac{E_B}{E_2 a^2}$  with  $a = \left(\frac{\text{Capsule area}}{\pi}\right)^{0.5}$  where  $E_B$  is the bending modulus [165]. Taking  $\alpha = 0.125$  and  $E_B = 0$ , Sui *et al.* [89] reported,  $D_{12}^\infty \approx 0.4$ .

In order to relate these results to our work, we calculate  $\alpha$  using  $E_2 = E \times H$  where  $E$  is the bulk shear modulus. We consider a thin shell with  $\frac{H}{R} = 0.05$  and  $\alpha = 0.15$ . For such thin shells, one can estimate the bending modulus as  $E_b = \frac{EH^3}{6(1-\nu)} \approx 5 \times 10^{-6}$  [64] which is very small and thus corresponds well to  $E_B = 0$  in [89]. Using these parameters, our FEM simulations in Fig. 3.1-b show  $D_{12}^\infty \approx 0.36$ . Alternatively, one can estimate  $D_{12}^\infty$  by extrapolating in Fig.3.10 of the Supporting Information to get an approximation of its

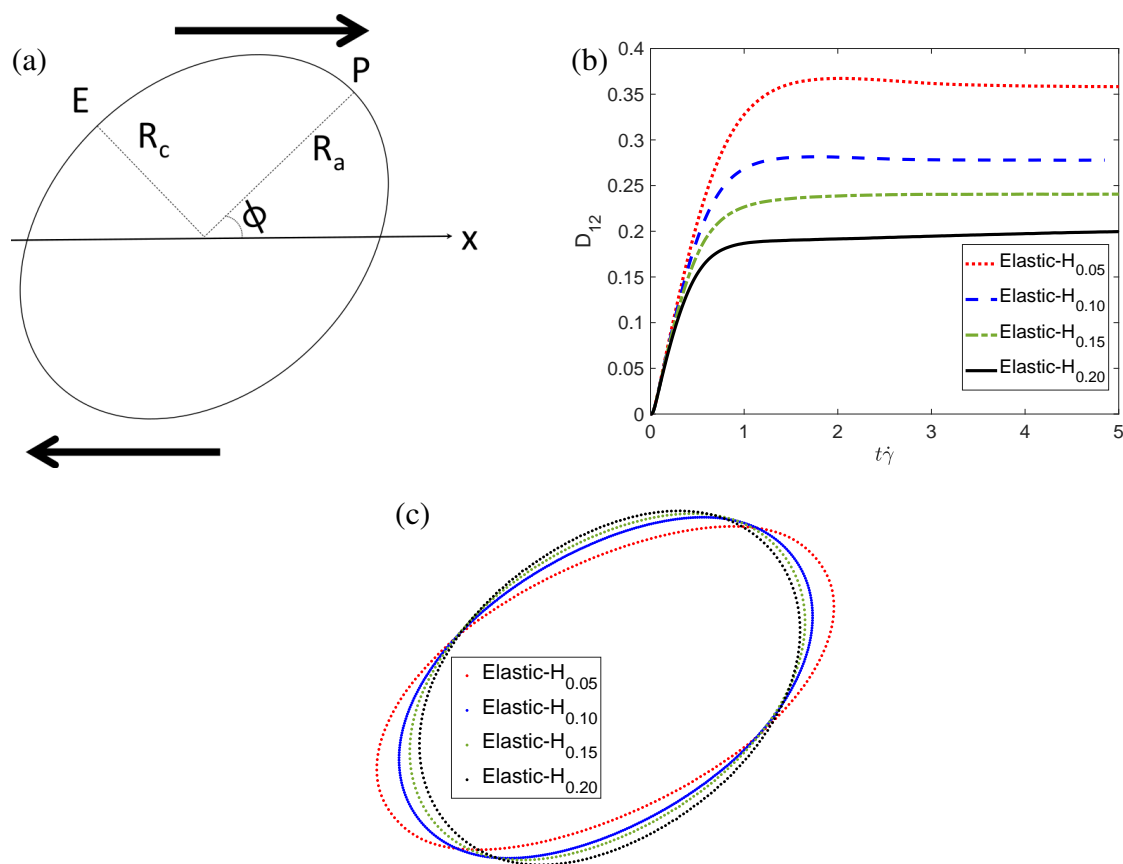


Fig. 3.1 (a) Schematic deformation of an elastic capsule under linear shear flow. "P" and "E" denote one of the poles and the equator of the ellipse, respectively. (b) Deformation parameter  $\frac{R_a - R_c}{R_a + R_c}$  against dimensionless time for  $Elastic - H_x$ , where  $x = \frac{H}{R}$  is the thickness to radius ratio. For all simulations  $Ca_v = 0.0075$ . (c) Exemplary profiles of deformed capsules from (b) after having reached the steady tank-treading state.

magnitude when  $\frac{H}{R} = 0$ . This approach gives  $D_{12} \approx 0.42$ . Both values are consistent with the results of [89].

For 3D capsules with an effective finite thickness, Dupont *et al.* [103] reported that the thinner capsules deform faster and become more elongated when subjected to a linear shear flow. They also showed that for a given thickness, the higher shear rates result in larger deformation rates and more deformed steady shapes. Qualitative agreement between these observations and the FEM simulations for a 2D capsule can be clearly seen in Fig.3.2-a where the effects of thickness ratio and shear rate on the deformation of capsules are demonstrated. Furthermore, in full agreement with their findings, plotting  $D_{12}^\infty$  against  $Ca_s = \frac{Ca_v}{(\frac{H}{R})}$  will cause all these results to fall on one master curve which corresponds to a membrane wall without bending resistance as demonstrated in Fig.3.2-b. Further comparison can be made for the

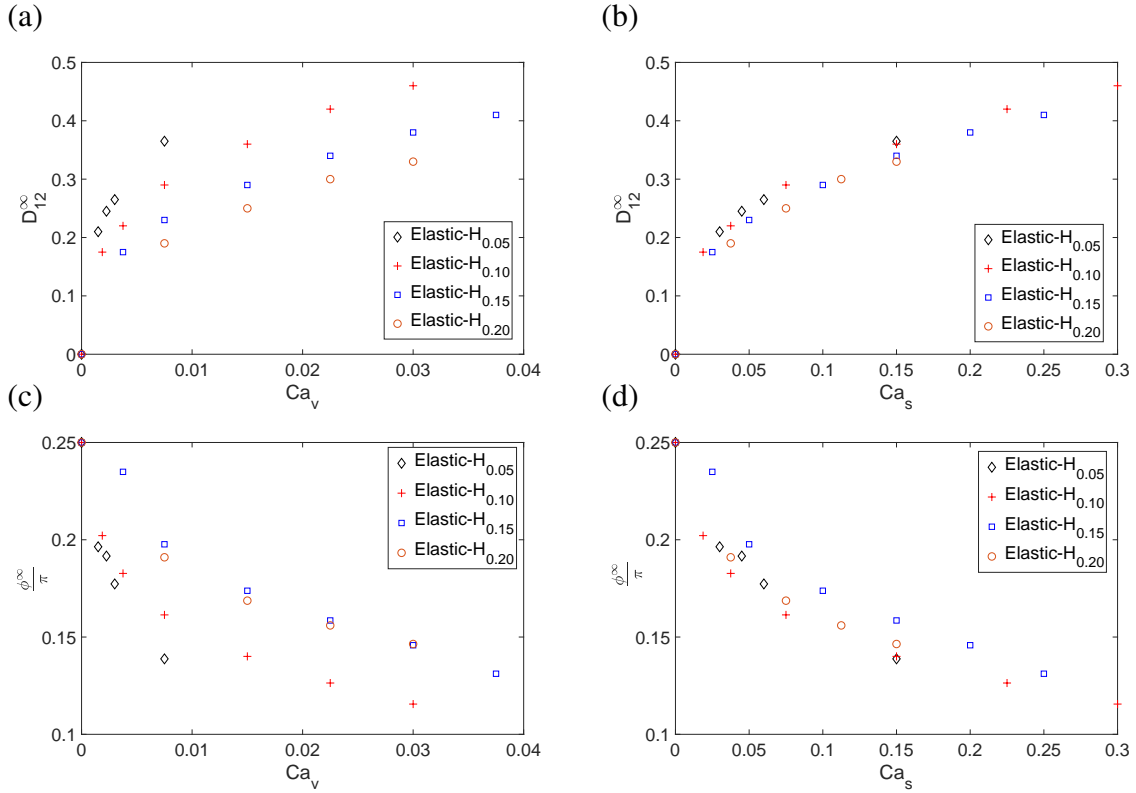


Fig. 3.2 (a)+(b) The equilibrium deformation indices  $D_{12}^{\infty}$  against  $Ca_v$  and  $Ca_s$  for elastic capsules with different thickness ratios  $\frac{H}{R} = 0.05, 0.1, 0.15, 0.20$ . (c)+(d) The equilibrium inclination angles  $\phi^{\infty}$  against  $Ca_v$  and  $Ca_s$  for the same capsules. Plotting the data over the surface capillary number  $Ca_s$  leads to the collapse of the data on one curve in agreement with earlier observations for 3D capsules [103].

inclination angle  $\phi$  of the deformed capsules. Consistent with former analytical studies and experimental observations [90, 164], for high shear rates, i.e. larger  $Ca_v$ , the equilibrium inclination angle ( $\phi^{\infty}$ ) decreases, and for smaller values of  $Ca_v$  it approaches the value of  $\frac{\pi}{4}$ , Fig.3.2-c. Additionally, we show that the thinner capsules are more inclined in a given shear flow. This can be attributed to the more elongated form of these capsules compared to the ones with thicker walls. Similarly as above, plotting  $\phi^{\infty}$  against  $Ca_s$  makes the  $\phi^{\infty} - Ca_v$  plots to approach a single curve as demonstrated in Fig.3.2-d.

### 3.3.1.2 Thinning of elastic shells

During the deformation of the capsule from the circular shape to the ellipse, while at the same time the enclosed area remains constant, the circumference of the capsule elongates. Since the shell is nearly incompressible its elongation leads to thinning in perpendicular direction. However, the thinning of the shell is not homogeneous. Direct measurements of the thickness values from simulation results show that the instantaneous thickness of the shell

$h$  reaches a minimum at the equator independent of the initial thickness and the applied shear rates while the maximum value of thickness is located at the poles as shown in Fig.3.3-a. Moreover, this plot implies that the thinner shells show less resistance to the thinning given the same flow conditions.

In order to explain these observations, the stress distribution in the thickness of the capsule wall is plotted in a coordinate system overlapping with the main axes of the ellipse, see Fig.3.3-b. In the vicinity of the equator, negative values of  $S_{11}$  indicate compressive stresses normal to the surface. In the same location, the circumferential stresses change sign from positive  $S_{22} > 0$  near the inner wall to  $S_{22} < 0$  near the outer wall. Furthermore, the magnitude of the off-diagonal components of the stress tensor, representing the in-plane shear stresses, are an order of magnitude smaller than the normal stresses. Therefore their contribution to the local shell deformation can be safely ignored. Similar analysis can be carried out for the poles of the ellipse, where the normal and tangential stresses are shown by  $S_{22}$  and  $S_{11}$ , respectively. Also here, the normal stresses are compressive. The tangential stresses however reverse and are compressive in the inner surface, and stretching close to the outer surface. In both locations, the tangential stresses are due to the local change of curvature. At the equator the curvature keeps decreasing and thus the outer surface of the ellipse experiences a tangential compression,  $S_{22} < 0$ , while the inner surface is stretched,  $S_{22} > 0$ . In the poles the curvature increases thus explaining the sign reversal of the tangential stresses compared to the equatorial location. The normal stresses on the other hand result in the local thinning of the shell. At the equator and in the poles, the normal stresses are compressive as shown by negative values of  $S_{11}$  and  $S_{22}$ , respectively. However, compressive stresses at the poles are smaller compared to those acting on the equator. Therefore, the thinning of the shell is less severe in this position. This leads to the hypothesis that the inhomogeneous compression and thinning of the shell is a possible mechanism of capsule breakup at higher shear rates, and the breakup is likely to happen at the equator.

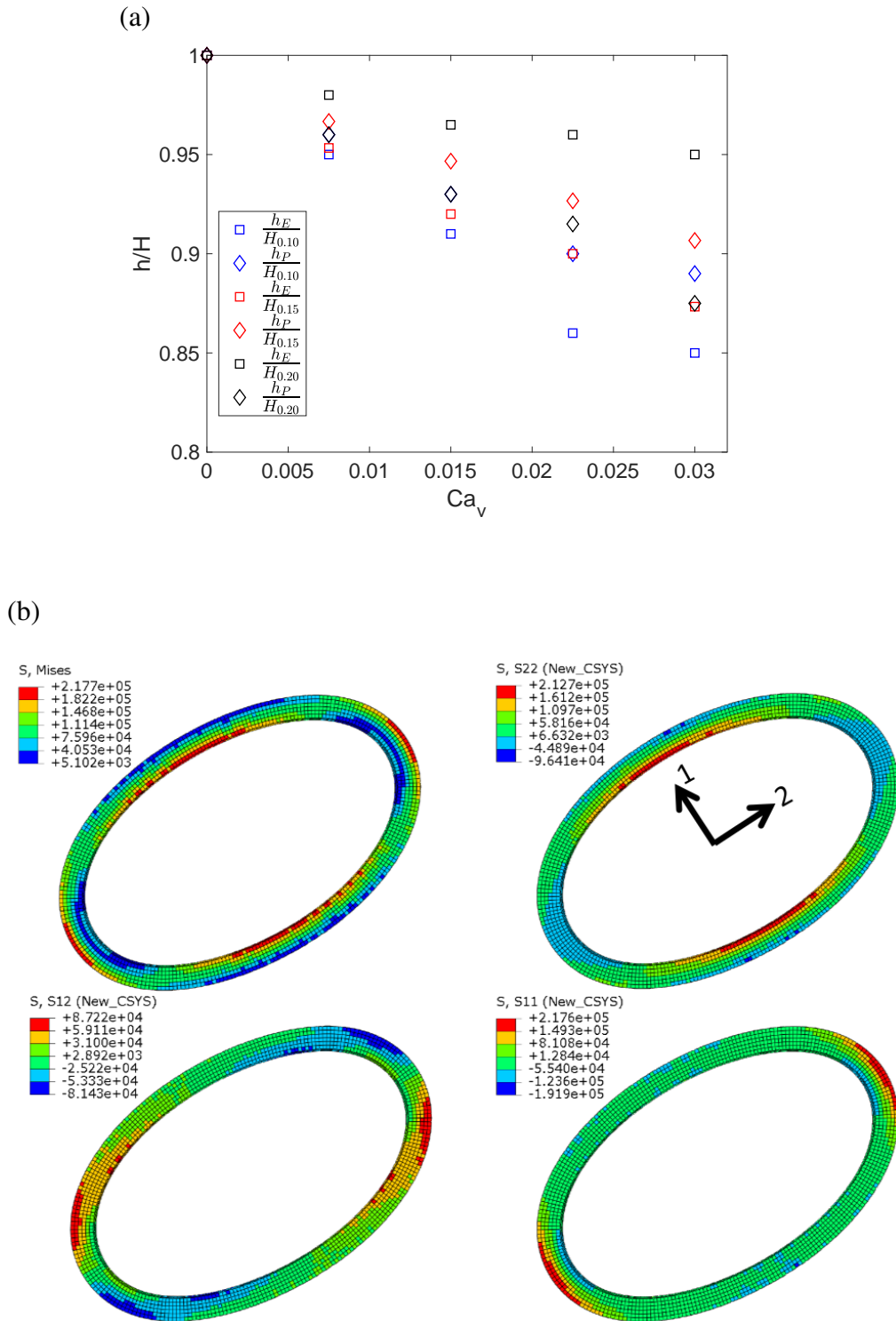


Fig. 3.3 (a) The shell thickness ratio ( $\frac{h}{H}$ ) in the equator of the ellipse and at its poles as a function of shear rate for the exemplary cases of *Elastic* -  $H_{0.10}$  in blue, *Elastic* -  $H_{0.15}$  in red, and *Elastic* -  $H_{0.20}$  in black. (b) Stress distribution in shell thickness of *Elastic* -  $H_{0.15}$  after reaching the equilibrium shape, where  $Ca_v = 0.0075$ .

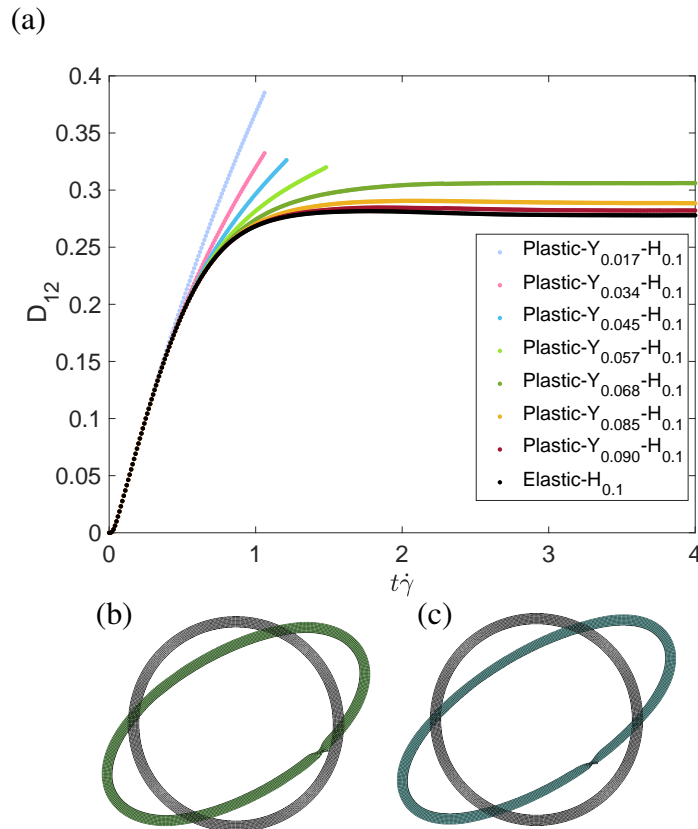


Fig. 3.4 (a) Deformation parameter  $D_{12}$  against dimensionless time  $t\dot{\gamma}$  for plastic capsules with different plasticity compared to a purely elastic capsule. In all cases  $Ca_v = 0.0075$ . (b)+(c) The numerical breakup of the  $Plastic-Y_{0.057}-H_{0.10}$  at  $t\dot{\gamma} = 1.48$ , and  $Plastic-Y_{0.017}-H_{0.10}$  at  $t\dot{\gamma} = 1.06$ . The elements are extremely distorted in one spot which we tentatively attribute to indicate the burst location.

### 3.3.2 Plastic deformation of the shell

#### 3.3.2.1 Onset of plasticity

When the magnitude of the von-Mises stress  $\sigma_{VM}$  locally exceeds the value of the yield stress  $\sigma_y$ , the deformation of the capsule wall enters the plastic regime. During the elastic phase the largest von-Mises stresses are located in the vicinity of the equator in the inner surface of the capsule as well as near the poles at the outer edge as detailed in Figs. 3.3-b and Fig.3.11. Accordingly, plastic deformation starts in these locations. As the capsule wall yields, its resistance to deformation decreases and it elongates with a rate higher than that of the purely elastic wall. Therefore, the  $D_{12} - t\dot{\gamma}$  curve of a plastic capsule deviates from that of the elastic one as soon as the plastic deformation takes place as illustrated in Fig.3.4.

A determining factor in the onset of plastic deformation is the magnitude of yield stress for a given  $E$  or its dimensionless equivalent, the plasticity ratio  $\frac{\sigma_y}{E}$ . This is of practical

importance when manufacturing microcapsules. For example, Koleva *et al.* report how the changes of n-Octadecyltrichlorosilane concentration can noticeably affect the magnitude of  $\sigma_y$  and the surface elastic modulus of Polysiloxane microcapsules [104]. However these changes are not proportional, i.e.  $\frac{\sigma_y}{E} \neq const.$  Here we show that the smaller values of  $\sigma_y$  given the same  $E$  result in an earlier and larger deviation from the  $D_{12}^\infty - t$  behavior observed for their elastic counterparts, see Fig.3.4-a. Indeed, while shells with  $\frac{\sigma_y}{E} \geq 0.068$  deform into elongated steady shapes, shells with very low plasticity ratios are in general less resistant to deformation and thinning, therefore more likely to break up. *Plastic - Y<sub>0.017</sub> - H<sub>0.10</sub>* for instance is shown to burst at  $t\dot{\gamma} = 1.06$ . Fig.3.4-(b,c) suggest that the burst of *Plastic - Y<sub>0.017</sub> - H<sub>0.10</sub>* and *Plastic - Y<sub>0.057</sub> - H<sub>0.10</sub>* take place around the equator due to the extreme thinning of the shell in the burst location. Both results are reasonably independent of grid resolution, see Fig.3.12, and therefore may correspond to the actual breakup of the shell.

During further deformations of the capsule, larger parts of the shell enter the plastic phase. Consequently, at the equator of the ellipse, the capsule gets thinner and attains a smaller curvature due to the normal compressive and the tangential stresses, respectively. Because of yielding, the thinning of the plastic shell is larger than that of the corresponding elastic one. For instance, in the case of *Plastic - Y<sub>0.068</sub> - H<sub>0.10</sub>*, in the middle of ellipse we find  $\frac{h_E}{H} \approx 0.92$  and at the poles  $\frac{h_P}{H} \approx 0.93$ ; whereas, for *Elastic - H<sub>0.10</sub>* the corresponding thicknesses are  $\frac{h_E}{H} = 0.95$  and  $\frac{h_P}{H} = 0.96$ . Therefore, the resulting ellipse is more elongated, and the corresponding  $D_{12}^\infty - Ca$  curve further deviates from that of the elastic capsule. Furthermore, we find that the thinner capsules show smaller resistance to yielding, and compared to thicker shells their  $D_{12} - t\dot{\gamma}$  deviates more sharply from that of the elastic capsule Fig.3.5.

### 3.3.2.2 Pre-rupture hardening

Often, polymeric materials show strain-hardening before they break up which has also been demonstrated via an experimental-numerical analysis for melamin-formaldehyde microcapsules [29, 32]. Therefore, considering a hardening phase is necessary to obtain a realistic description of the deformation dynamics of such commercial systems in shear flow. In our model, hardening resembles a Hookean elastic phase that starts at a certain strain and ends only at breakup. Accordingly, hardening induces a resistance to the deformation of the shell. As a result, it reduces the deformation rates after yielding and increases the stability of the capsule hence leading to a less elongated shape as illustrated in Fig. 3.6. The effect of hardening on capsules with a low plasticity ratio can be even more pronounced. For instance, the dimensionless moment of numerical breakup for the plastic capsule without hardening, *Plastic - Y<sub>0.034</sub> - H<sub>0.10</sub>*, is 1.06. The counterpart capsule with a strain-hardening however remains unbroken even at  $t\dot{\gamma} \approx 4$  with a far more elongated steady shape.

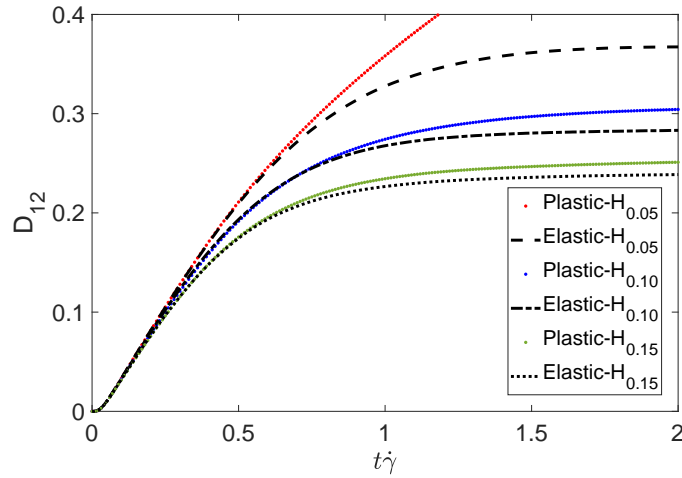


Fig. 3.5 The colored plots show the deformation of capsules with different wall thicknesses, but the same plasticity ratio,  $\frac{\sigma_y}{E} = Y_{0.068}$ , compared to their elastic counterparts shown as black lines. The thinner the capsule wall, the more drastic is the deviation of the plastic capsule's deformation from the elastic case. In all cases  $Ca_v = 0.0075$ .

### 3.3.2.3 Capsule breakup under cyclic shear flow

One interesting feature of plasticity is the permanent deformation of the system, and can lead to important effects, especially under periodic loading-unloading scenarios. These deformations are of relevance in many practical applications such as washing, where the microcapsules can undergo several load-relaxation cycles.

When the microcapsules are fully elastic, there is no energy loss and at the end of each cycle, they relax back to their original shape. Our model closely follows this expected behavior as shown in Fig.3.13. Therefore, if the elastic modulus is high enough (because of high cross-linking density for example) the capsules never break up or release their contents during loading-unloading process. Plastic behavior, however, can make the breakup more likely provided that the shear rate is high enough for the capsule deformation to enter the plastic regime. Composite polyelectrolyte MCs [44], and melamine-formaldehyde microcapsules [32, 26, 153] are examples of highly plastic systems. For example, the microcapsules in [32] possessed a plasticity ratio  $\frac{\sigma_y}{E} < 0.04$ , and might thus be expected to easily undergo plastic deformation.

In the following, the results of two shearing scenarios will be compared. The first scenario involves applying a continuous shearing for 0.1s after which the shearing is switched off and capsule relaxes till it reaches the equilibrium shape, i.e.  $\frac{dD_{12}}{dt} = 0$ . The second scenario is composed of four steps: first the shearing is applied for 0.05s, followed by 0.5s relaxation, after which the sequence repeats with another shearing phase of 0.05s and a relaxation phase

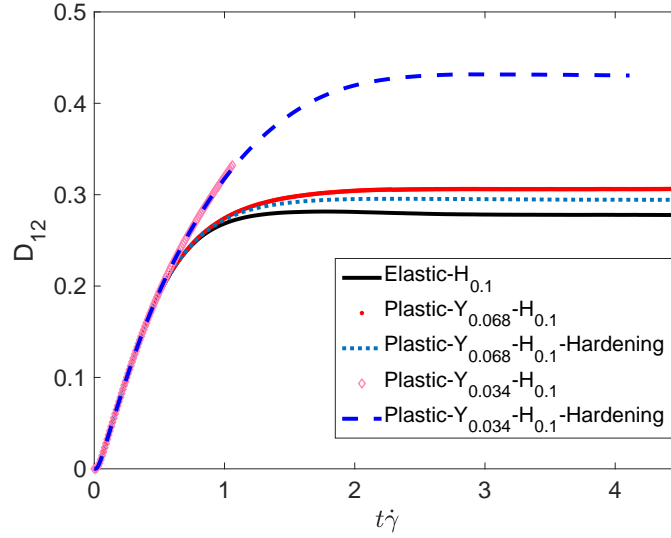


Fig. 3.6 The deformation dynamics of *Elastic* –  $H_{0.1}$  is shown in black. The deformations of *Plastic* –  $Y_{0.068}$  –  $H_{0.1}$  with and without hardening are illustrated in blue and red, respectively. Here, both cases attain a steady state, but strain-hardening leads to a noticeable increase in the resistance of the plastic shell to deforming hydrodynamic stresses. The effect of hardening is even stronger for *Plastic* –  $Y_{0.034}$  –  $H_{0.1}$ , where we observe a numerical instability and breakup without hardening (pink curve and Fig.3.12), but a steady state deformation if hardening is included. In all cases  $Ca_v = 0.0075$ .

of 0.5s. During the shearing step in the first scenario, the  $\sigma_{VM}$  exceeds the value of  $\sigma_y$  in the capsule membrane, therefore it deforms plastically in Fig.3.7-a. When the shearing is switched off, the stretched parts release the stored elastic energy and relax to a less energetic state. Plastic deformation, however, involves energy dissipation. Since the distribution of  $\sigma_{VM}$  is not homogeneous, different parts of the shell experience different extents of plastic deformation and, as a consequence, the relaxation of the shell becomes inhomogeneous as well. Therefore, the final state of a plastically deformed capsule after shearing and relaxation remains partly stretched as shown in Fig.3.7-a.

In the second scenario, the shearing step is shorter. Although  $\sigma_{VM}$  does exceed the yield stress, the total area undergoing the plastic deformation is smaller, Fig.3.7-b, and hence the dissipated energy is expected to be less compared to the first scenario. As a result, the shape after the first shear-relaxation step is less elongated and closer to the original circular shape. Shearing this deformed shape again and for the same amount of time increases the plastic deformation of the shell, leading to more elongated shape at the end of the second shearing step. Finally, after the second relaxation phase, we observe a final form which is less deformed compared to the plastic capsule in the first scenario as shown in Fig.3.7-b.

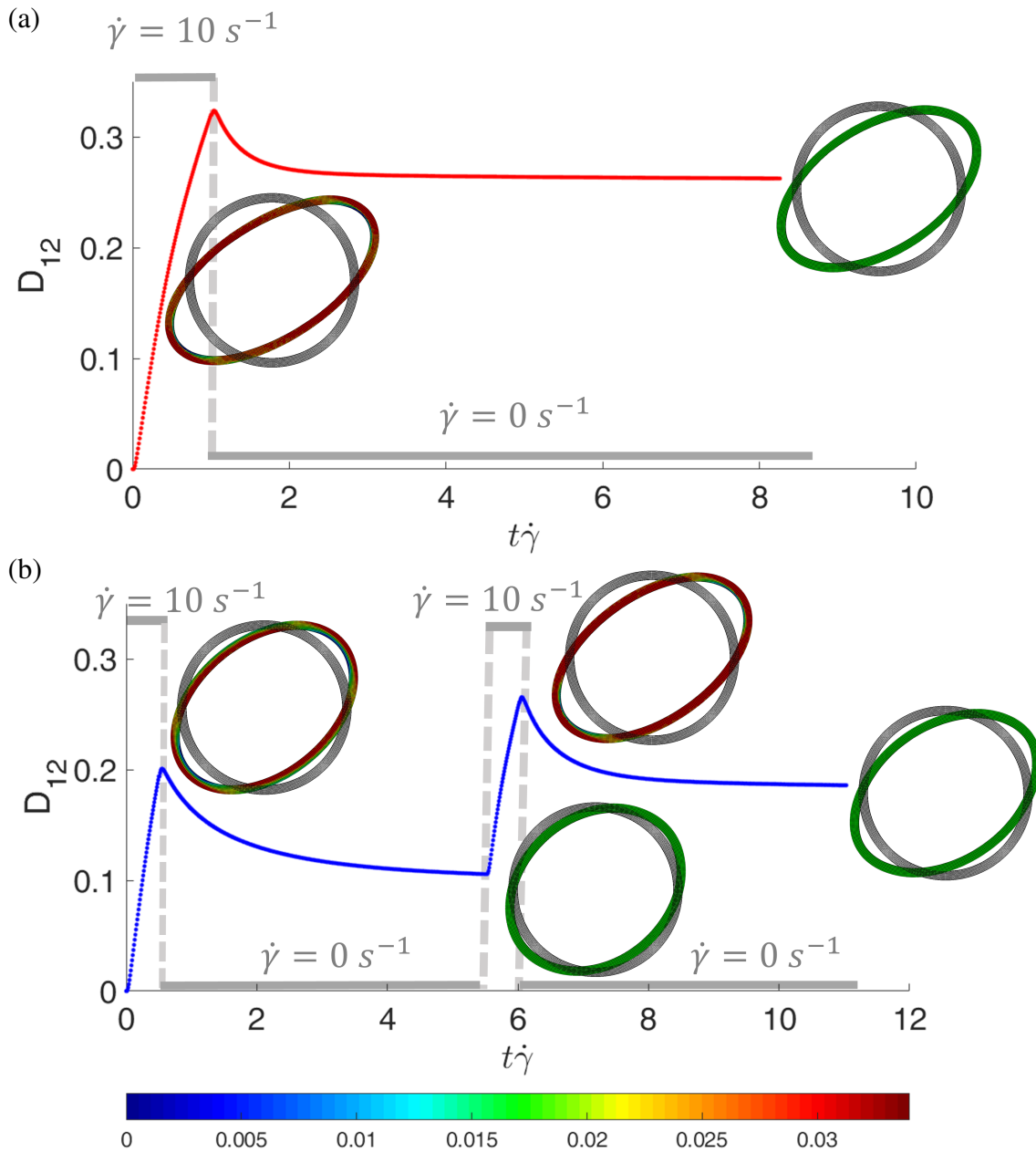


Fig. 3.7 The deformation dynamics of *Plastic* –  $Y_{0.034}$  –  $H_{0.1}$  during the first (a) and the second (b) deformation scenarios. In all shearing phases,  $Ca_v = 0.0075$ . The distribution of  $\sigma_{VM}$  in the deformed shell, at the end of each shearing step is illustrated. The permanently deformed shapes of the plastic capsule at the end of the relaxation steps are shown in green, and the original shape of the capsule is shown with black grids. The scale bar illustrates  $\frac{\sigma_{VM}}{E}$ . The grey diagrams in the background of the plots schematically illustrate the periodic shearing-relaxation steps of each scenario.

## 3.4 Conclusions

Deformation of capsules suspended in a shear flow is one of the important generic scenarios during which commercial capsules can break. Here, we numerically investigated a possible breakup mechanism for elastic as well as plastic microcapsules whose shell possess a finite thickness in 2D using the finite element software Abaqus-2016. Comparison of microcapsules with thin shells ( $\frac{H}{R} = 0.05$ ) led to good agreement with earlier works on 2D capsules with infinitely thin shells [89] thus verifying the applied simulation method. Similarly, our work reproduced the collapse of the Taylor deformation parameter for different shell thicknesses when plotted over the surface capillary number as observed also in 3D simulations [103]. Due to the finite thickness of the capsule shell in our model, we could quantify the shell thinning finding that thinning was more severe at the equator of the capsules and that the maximum thickness occurred at the capsule poles. We could trace back this result to the inhomogeneous distribution of compressive normal and stretching lateral stresses at these locations.

A second contribution of our work is the observation and characterization of the plastic deformation of microcapsules in shear flow. In accordance with recent studies using atomic force microscopy for the static deformation of microcapsules [32, 26], we assumed an elastic-perfectly plastic constitutive law for the mechanical behaviour of the shell. We showed that if the shear flow is strong enough to push the capsule into the plastic regime, depending on the plasticity ratio, the capsule deforms into a more elongated steady state, or it breaks up. We found that the dynamics and the moment of breakup as well as the location of burst were reasonably independent of mesh resolution. Therefore, the observed numerical breakup may correspond to the actual burst of the capsule in shear flow. Additionally, we showed that the thinner capsules are more sensitive to plasticity, i.e the  $D_{12} - t\dot{\gamma}$  deviates more sharply.

Subsequently, a strain-hardening regime before breakup was demonstrated to reduce the rate of deformation in the plastic regime, and to result in a less elongated capsule. Finally, the deformation of capsules under two cyclic shearing scenarios was discussed. We found that the first scenario with a longer uninterrupted shearing step proved to deform the capsule to a greater degree compared to the second scenario with two disconnected shearing steps.

Since plastic deformation is a common phenomenon in microcapsules [166, 46, 26, 32] our results provide an important starting point for more detailed modeling efforts of specific capsule types and flow scenarios which may eventually help in the design of novel microcapsules for specific applications where shear flows and breakup are essential, such as in drug delivery.

## **Acknowledgements**

We gratefully acknowledge support from the SFB/TRR 225 Biofabrication.

## 3.5 Supplementary information

### Mesh independence studies

**Elastic shells** The deformation dynamics of *Elastic* –  $H_{0.1}$ , with different grid resolutions as shown in Fig. 3.8-a. *Elastic* –  $H_{0.1} - L_{0.25}$ , with  $\frac{L}{H} = 0.25$ , shows a stable and convergent result that does not change by increasing the mesh resolution Fig. 3.8-b. Therefore, for the elastic shells this level of refinement is used.

**Plastic shells** In Fig. 3.9-a, *Plastic* –  $Y_{0.068} - H_{0.10} - L_{0.25}$  gives stable and convergent results. However, increasing the mesh refinement level changes the simulation results to lower  $D_{12}$  in the plastic regime. The deformation dynamics of *Plastic* –  $Y_{0.068} - H_{0.10} - L_{0.125}$  on the other hand remain independent of grid resolution. This is consistently observed for capsules with other plasticity ratios, Fig. 3.9-b. Therefore this level of refinement is applied for the plastic shells.

**Breakup Dynamics** Fig. 3.12 demonstrates the breakup dynamics of *Plastic* –  $Y_{0.057} - H_{0.10}$  and *Plastic* –  $Y_{0.017} - H_{0.10}$  with different mesh resolutions.

### Further data

**Comparison with infinitesimally thin shells** In literature, the studies of 2D capsules are limited to the ones with infinitesimally thin shells. In order to compare the FEM simulation results with them, we plot the  $D_{12}^{\infty}$  against the shell thickness, and extrapolate its value using a polynomial data fitting in order to estimate  $D_{12}^{\infty}$  at  $\frac{H}{R} = 0$ , see Fig.3.10.

**The onset of plasticity** The plasticity begins where the  $\sigma_{VM}$  exceeds the value of yield stress. During the elastic deformation, the highest values of  $\sigma_{VM}$  are located at the inside edge of the deformed capsule at the equator, and at the outer edge of the capsule in the poles. Therefore it is expected that the plastic deformation takes place at these locations; see Fig.3.9.

**The recovery of the elastic shell** As expected, the elastic capsule relaxes to its original shape when the shearing is switched off, see Fig.3.13.

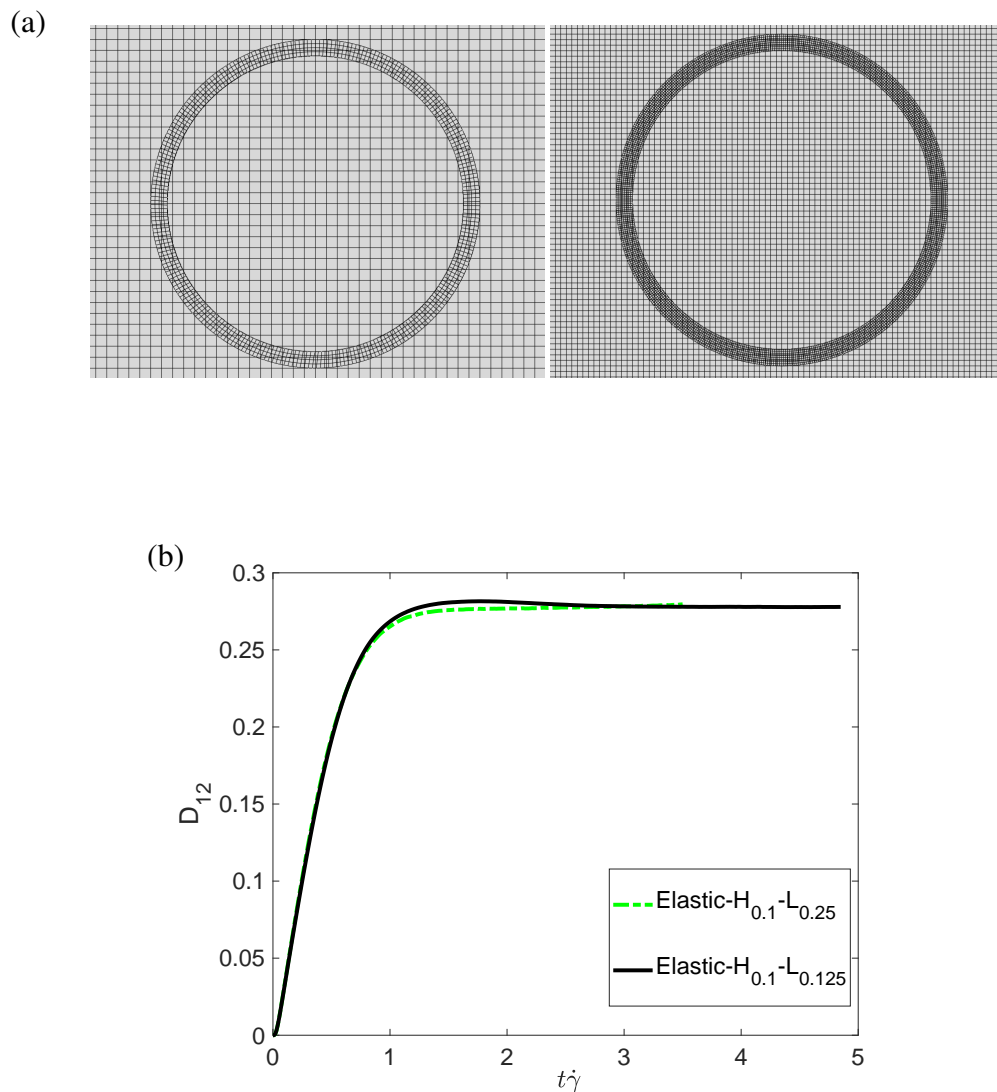


Fig. 3.8 (a) From left to right ,  $Elastic - H_{0.1} - L_{0.25}$ , and  $Elastic - H_{0.1} - L_{0.125}$ , where the number after  $L$  is  $\frac{L}{H}$ . (b) Deformation index,  $D_{12}$ , against dimensionless time for  $Elastic - H_{0.1}$  meshed as shown in (a). The coarsest mesh is composed of 1012 C3D8R [40] elements for the shell, and 10816 EC3D8R [40] elements for the fluid domain.

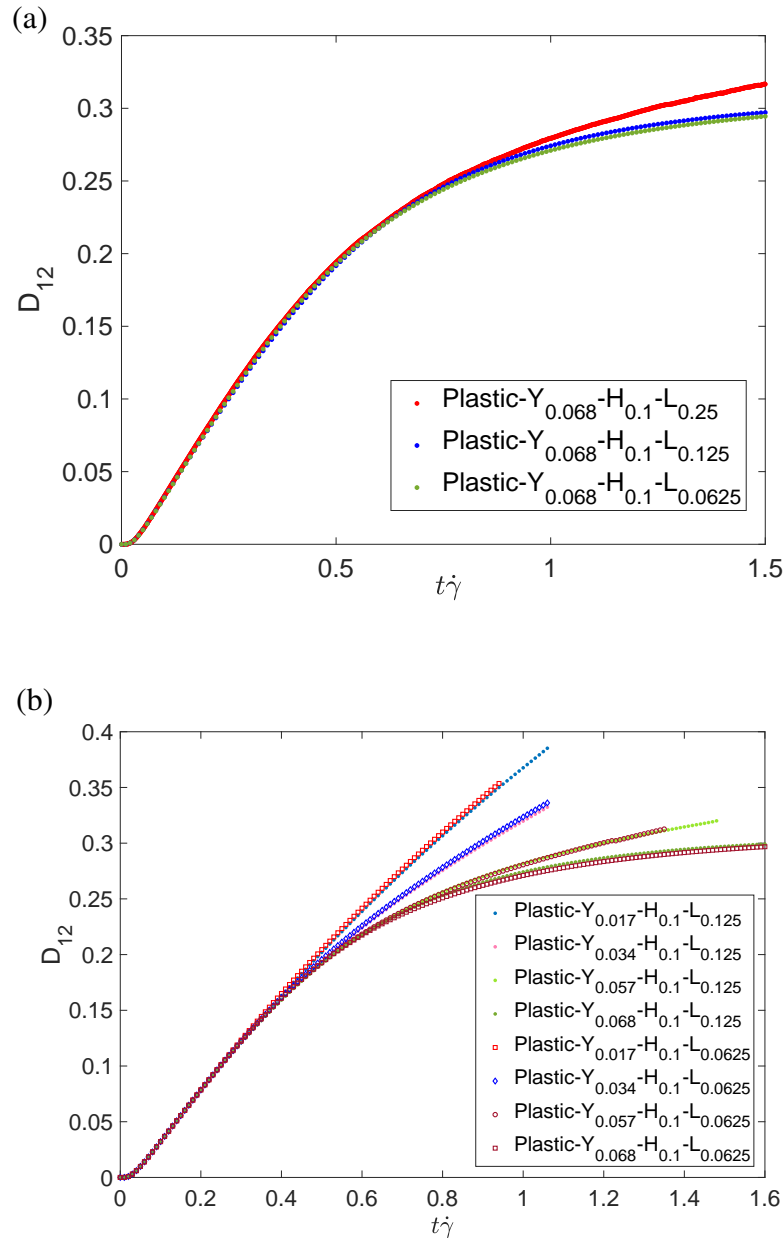


Fig. 3.9 (a) Deformation index,  $D_{12}$ , against dimensionless time for  $Plastic - Y_{0.068} - H_{0.1} - L$ . The coarsest mesh for  $Plastic - Y_{0.068} - H_{0.1} - L_{0.25}$  is composed of 1012 C3D8R [40] elements for the shell,  $\frac{l}{H} = 0.25$ , and 10816 EC3D8R [40] elements for the fluid domain. (b) The results of  $Plastic - Y - H_{0.1} - L_{0.125}$  remain independent of grid resolution, in different plasticity ratios.

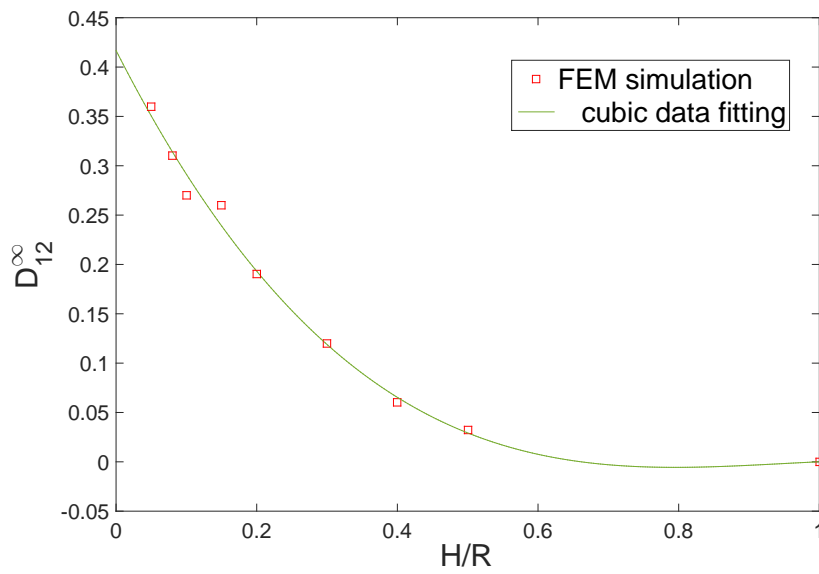


Fig. 3.10 Deformation index against thickness ratio  $\frac{H}{R}$  for *Elastic* –  $H_x$  capsules, with  $Ca_v = 0.0075$ . The green line corresponds to a cubic data fit that is used to obtain an estimate of  $D_{12}^{\infty}$  when  $\frac{H}{R}$  approaches zero.

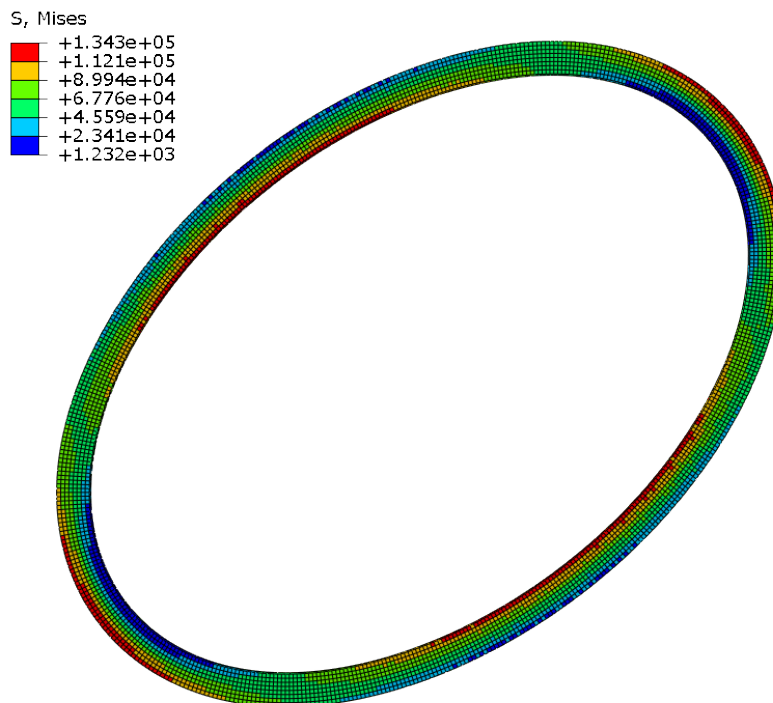


Fig. 3.11 Stress distribution in shell thickness right before yielding ( $(\sigma_{VM})_{max} < \sigma_{yield}$ ) for *Plastic* –  $Y_{0.068}$  –  $H_{0.1}$ .

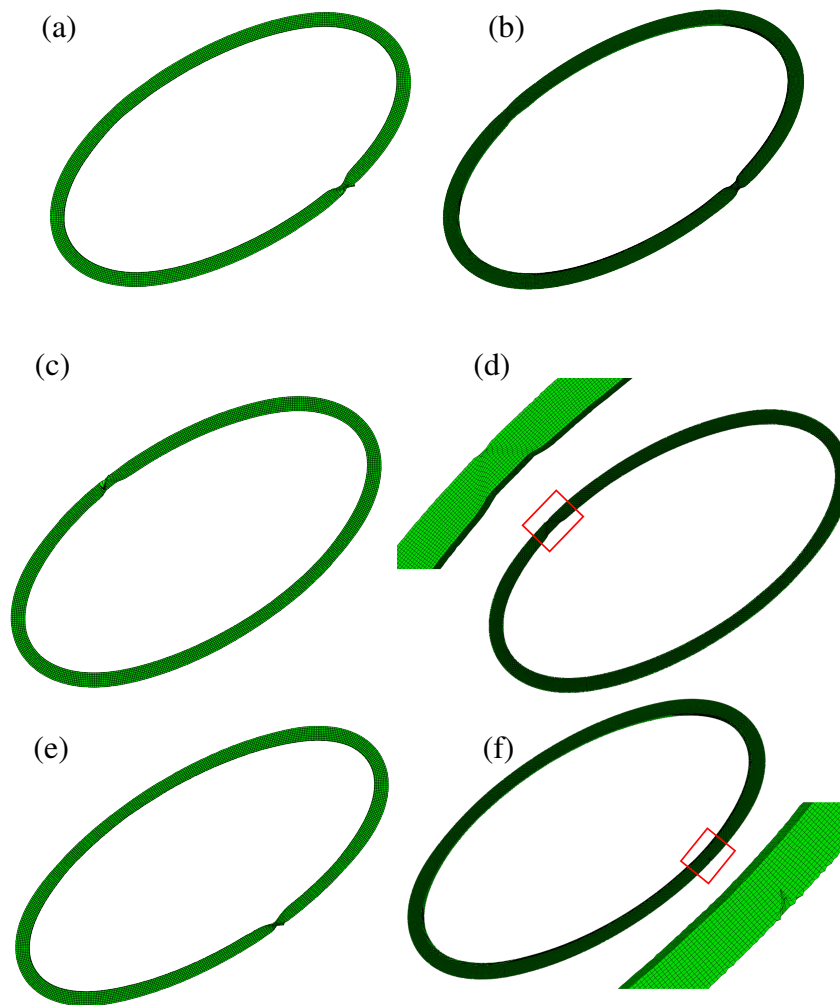


Fig. 3.12 (a)-(f) The breakup of  $Plastic - Y_{0.057} - H_{0.10} - L_{0.125}$ ,  $Plastic - Y_{0.057} - H_{0.10} - L_{0.0625}$ ,  $Plastic - Y_{0.034} - H_{0.10} - L_{0.125}$ ,  $Plastic - Y_{0.034} - H_{0.10} - L_{0.0625}$ ,  $Plastic - Y_{0.017} - H_{0.10} - L_{0.125}$ , and  $Plastic - Y_{0.017} - H_{0.10} - L_{0.0625}$  respectively. The insets magnify the distortion of the elements in the burst location.

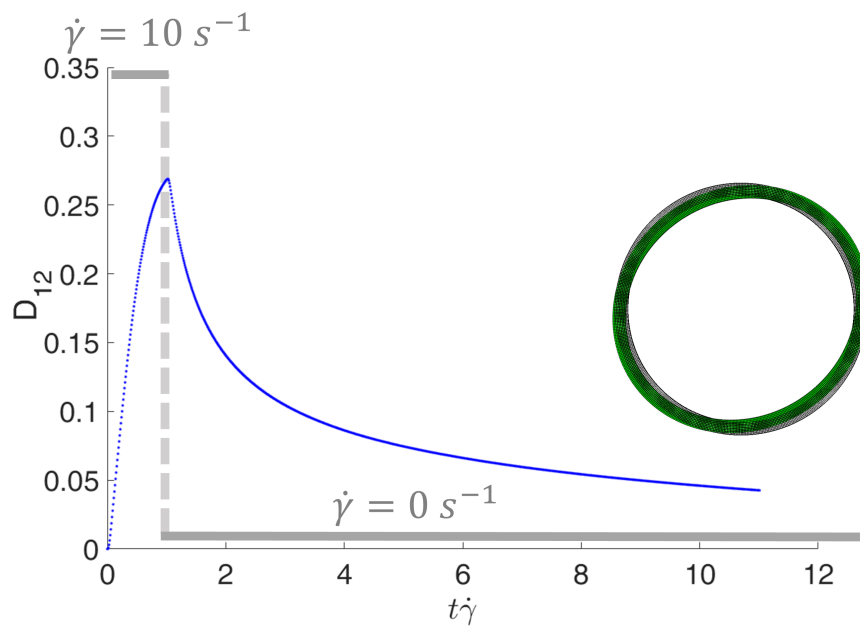


Fig. 3.13 The recovery of the *Elastic* –  $H_{0.1}$  shown in green, with the deformation dynamics shown in blue. The grey diagram in the background of the plot schematically illustrates the applied shearing and the relaxation steps. The black mesh shows the original capsule.

# Chapter 4

## **One-component dual actuation: Poly(NIPAM) can actuate to stable 3D forms with reversible size change<sup>†</sup>**

Li Liu<sup>1</sup>, Ali Ghaemi<sup>2</sup>, Stephan Gekle<sup>2</sup>, Seema Agarwal<sup>1\*</sup>

<sup>†</sup> Published as: L. Liu, A. Ghaemi, S. Gekle, and S. Agarwal, *One-component dual actuation: Poly (NIPAM) can actuate to stable 3D forms with reversible size change*, *Advanced Materials* 28, 9792–9796 (2016), DOI: 10.1002/adma.201603677

1. Macromolecular Chemistry II and Bayreuth Center for Colloids and Interfaces, Universität Bayreuth, Universitätsstraße 30, 95440 Bayreuth, Germany
2. Biofluid Simulation and Modeling, Fachbereich Physik, and Bayreuth Center for Colloids and Interfaces, Universität Bayreuth, Universitätsstraße 30, 95440 Bayreuth, Germany.

\* Corresponding author

**Abstract** A rare example of a one-component dual actuator is provided, which displays irreversible change in shape by rolling on contact with water and reversible size change on changing the temperature. The actuator has a bilayer structure with aligned and randomly oriented fibers of poly(N-isopropyl acrylamide). A combination of anisotropic  $E$  modulus and temperature dependent swelling/shrinkage provides the dual actuation.

## 4.1 Main text

In the last many years artificial polymeric bilayer architectures inspired from nature have been used for light, temperature, moisture, or electric and magnetic field triggered reversible twisting, bending and curling motions [167–181]. One of these most studied bilayer systems makes use of thermoresponsive hydrogels as active layer undergoing temperature dependent swelling/shrinking in water/ humid air in combination with a hydrophobic (passive) polymer inert layer leading to shape change [182–189]. Fast actuation, large deformations, reversibility, direction control, maintaining low cost and simple procedures of production of thermoresponsive bilayer actuators have already been achieved in one way or the other as evidenced from the literature [187–189]. A piece of paper though only one component also curls or bends on a water surface due to the differential swelling across the paper thickness. The curvature increases with time to a maximum and then flattens as the sheet becomes completely wet [190]. Artificial one component thermo-/hygro-responsive actuation is a rare phenomenon as special procedures are required for creating structural anisotropy. In one of the studies, which in real sense is not one component the anisotropy was generated by orientation of stiff inorganic particles within the swellable/shrinkable polymer hydrogel or thermoresponsive gel along the layer thickness using a weak external magnetic field. The hydrogels reversibly changed shape in accordance to the orientation of the particles [191]. A graphene paper with a gradient of reduced graphene oxide (hydrophobic)/graphene oxide (hydrophilic) showed reversible deformations with moisture and heat due to water driven differential expansion/contraction [192]. The gradient along the thickness can also be achieved by differential molar mass of the base polymer or cross-link density [193, 194]. A gradient along the thickness in a Poly(NIPAM) film was created by concentrating silica particles on one side of the film by electrophoresis followed by photo-polymerization. The cross-linked poly(NIPAM) gel in water bent at 40°C with the silica side outside. The removal of silica particles can provide gradient porous poly(NIPAM) gel bending in opposite direction [195].

Reversibility in actuation is seen as one of the advantages providing performance for many cycles. The majority of thermoresponsive actuators are reversible showing opening

and closing of tubes, curls, inversion of surfaces (inside-out) with change in temperature. For many applications, such as externally triggered formation of 2D and 3D scaffolds, reversibility of actuation is not desired as a slight change in temperature would reverse the process destroying the scaffold structure. Therefore, very fast irreversible actuation/shape/form change making 2D and 3D stable structures via temperature as the external trigger, in a simple way, and on a large scale is also a challenge. Here we report our new findings regarding dual one-component actuator with the following highlights: 1) actuation of only-poly(NIPAM)) membranes without any additional components; 2) formation of very fast 3D hollow tubes by temperature triggered self-rolling and curling in an irreversible way in different directions and being stable at all temperatures in water once they are formed; 3) actuation in size depending upon the temperature; 4) the observed behaviour is traced back to the unique combination of anisotropic thermal expansion and the anisotropic elastic modulus of the employed material as demonstrated by numerical simulations.

Cross-linked poly(NIPAM) fibrous membranes made by electrospinning show temperature and fiber alignment dependent swelling and shrinkage in water. Two such differently swellable/shrinkable poly(NIPAM) fibrous mats were combined together to generate a swelling/shrinkage gradient along the membrane thickness (perpendicular to the interface) to create temperature triggered very fast actuation. The gradient thickness can be easily adjusted by the time of spinning and is used for providing the irreversible actuation. For making such membranes, randomly aligned fibers were first spun on a horizontally rotating disc of diameter 13 *cm* at 30 *rpm* followed by deposition of aligned fibers on a vertically rotating disc of diameter 20 *cm* and disc rim of 4 *cm* with a rotating speed of 800 *rpm*. The degree of alignment of fibers, as calculated by the formula 1 (supporting information) was 97%. The fibrous mat was pressed at room temperature at 300 bars for 20 minutes and photo cross-linked to get a strong interface between the fiber layers (Figure 4.1-a, Figure 4.4). This method of making a stable fibrous layered membrane (no delamination on repeated use in water) was established in our previous work on bicomponent membranes [187]. The porosity, as determined by equations 2-4 (supporting information), was 40% and 33%, respectively, for random and aligned fibrous layers. The average diameters of as-spun random and aligned fibers were 1.5  $\mu\text{m}$  and 1.3  $\mu\text{m}$ , respectively (Figure 4.4). The resulting sample with asymmetric alignment of fibers was cut at varied angles to provide samples with randomly arranged fibers in one layer and parallel arranged (Bi-PNIPAM-0°), perpendicularly arranged (Bi-PNIPAM-90°), and fibers arranged at 45° (Bi-PNIPAM-45°) with respect to the long axis in the second layer as shown in Figure 4.1-a.

For comparison purposes, poly(NIPAM) individual random (mono-ran-PNIPAM) and aligned fibrous mats (PNIPAM-0°; PNIPAM-90°; PNIPAM-45°) were also prepared. Tem-

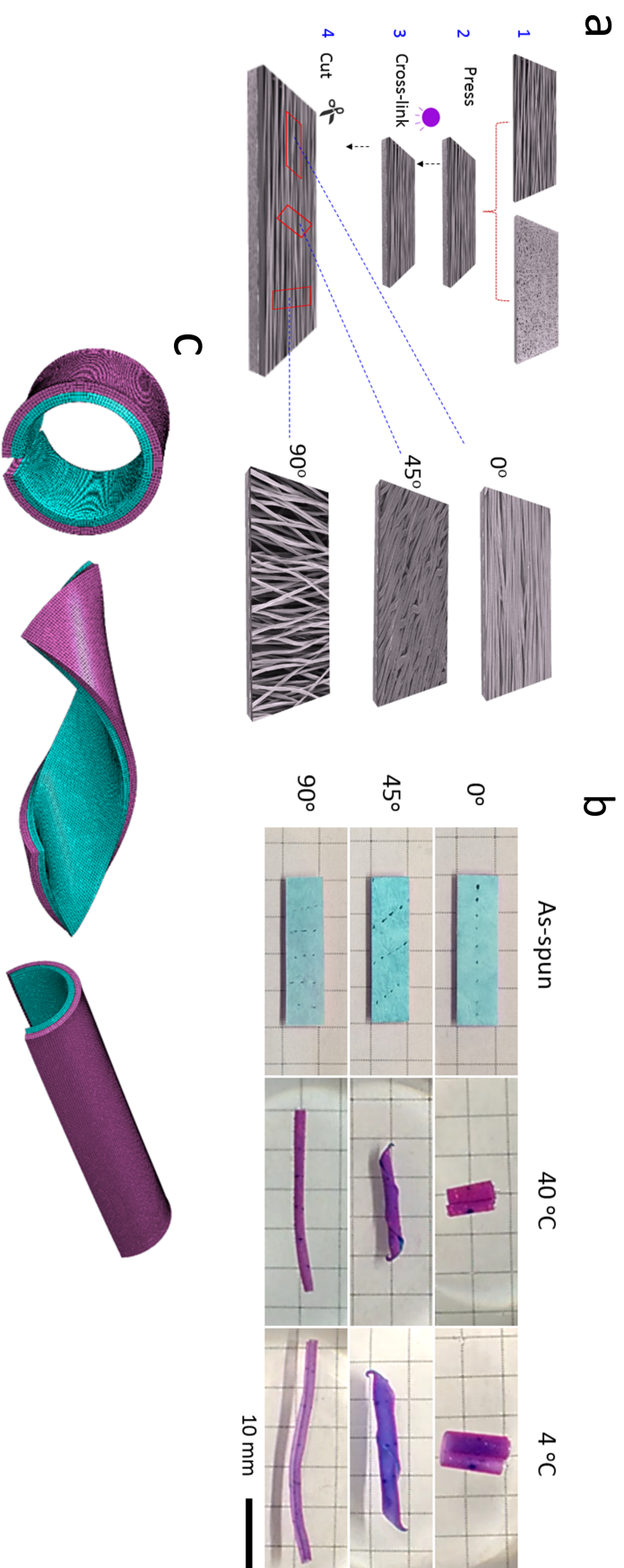


Fig. 4.1 a) Schematic of formation of Bi-PNIPAM-0°, Bi-PNIPAM-45°, Bi-PNIPAM-90° actuator by electrospinning of aligned layer and random layer, respectively (Step 1), followed by pressing and cross-linking (Steps 2 and 3). At last, the samples were cut into pieces at different angles (Step 4); b) one component poly(NIPAM) directionally controlled actuation: movement of Bi-PNIPAM-0°, Bi-PNIPAM-45°, Bi-PNIPAM-90° mat (aligned (blue)/ random (pink) (length: 2.0 cm, width: 0.5 cm) with the thickness ratio (aligned/bilayer) of 0.65) in water at different temperatures. Fiber alignment direction was indicated by a black dotted line on the sample. The good color contrast by dyeing the aligned and random mats might be invisible due to the transparency of poly(NIPAM-ABP) in water; c) equilibrium shapes of bilayer mats obtained from finite-element simulations in 40 °C water. From left to right are 0°, 45°, and 90° fiber alignments in one of the two layers. By using anisotropic expansion coefficients in combination with an anisotropic elastic modulus, good agreement with the experimental shapes in (b) is obtained.

perature and fiber alignment dependent swelling and shrinking of individual poly(NIPAM) fibrous mats with different fiber alignments is shown in Figure 4.5, and Table 4.1. The mat with fibers aligned parallel to the long axis of the fibers (PNIPAM-0°) showed around 33% shrinkage and 18% swelling in the direction parallel and perpendicular to the fiber alignment, respectively, whereas fiber mats with random alignment of fibers (mono-ran-PNIPAM) shrank approx. 11% in both directions on putting in water at 40°C, in a similar way as described previously [187, 188]. When two such fibrous mats (PNIPAM-0° and mono-ran-PNIPAM) were combined together in the form of a layered structure (thickness of PNIPAM-0° and mono-ran-PNIPAM fibrous mats were 33.9  $\mu\text{m}$  and 17.9  $\mu\text{m}$ , respectively; size: 2.0 cm  $\times$  0.5 cm  $\text{Length}(L) \times \text{Width}(W)$ ) and immersed in water at 40 °C, the structure showed rolling along the fiber alignment direction with the randomly oriented fibrous layer forming the outside of the rolls (Figure 4.1-b, and Movie-1 in Supporting Information) due to the gradient in differential shrinkage along the thickness. The high shrinkage of PNIPAM-0° compresses the mono-ran-PNIPAM layer all along the interface leading to rolling. Based on the naive assumption of an isotropic  $E$  modulus, the differential swelling and shrinkage pattern in Table 4.1 would suggest that rolling perpendicular to the direction of fiber alignment should also happen for a bilayer of PNIPAM-0° and mono-ran-PNIPAM. The preference of rolling along the length of the fiber mat can be explained by a significant difference in  $E$  modulus of the aligned PNIPAM-0° fibrous mat in parallel and perpendicular directions. Indeed, we measured the  $E$  modulus of the aligned fibrous mats in the dry state (Figure 4.6) and find that in the perpendicular direction it is much smaller than in parallel direction. Thus, even though the material does attempt to increase its size in the perpendicular direction, the resulting stress is too small to create buckling in this direction. Although a similar mechanical test on wet samples could not give any accurate quantitative values due to handling and gripping problems together with the difficulty of keeping uniform shape which is a general problem of all soft gels, a qualitatively similar trend is expected. We note that a similar mechanical anisotropy with a higher modulus in parallel direction in comparison to that in perpendicular direction is known for other soft gels [196].

The rolled tubes, when taken out from water, and dried, either at room temperature or at 60 °C, in a vacuum oven for 24 h did not return back to the original flat shape. However, they showed reversible change in size on changing the water temperature from 40 to 4 to 40°C keeping its tubular shape for at least 30 cycles. On transferring the rolled 3D structures in water from 40 to 4°C and vice versa led to no significant change in shape. Indeed, for a shape change when going from 40 to 4 °C (the temperature below lower critical solution temperature (LCST) of poly(NIPAM)), which in the first instant should be opening of the tube, two possible scenarios are (1) the inside layer swells in parallel direction and the outside

layer does not change its length, (2) both layers swell in parallel direction with the inside layer swelling appreciably more than the outside layer. Under both these conditions, the compressive force generated along the interface would open the tube. But from Table 4.1, it is evident that both mono-ran-PNIPAM (the outside layer) and PNIPAM-0° (inside layer) swell to almost the same extent in parallel direction. The mono-ran-PNIPAM increases in length by  $\approx 43\%$ , whereas PNIPAM-0° showed  $\approx 40\%$  increase. Therefore, in our case there is no net compressive force on the interface to open the tube. This explains irreversible shape change.

Once the tubes are formed, the change in water temperature to  $4^\circ\text{C}$  and vice versa led to an almost instant reversible change in size. The tubes swell (both length and width) at  $4^\circ\text{C}$  and shrink at  $40^\circ\text{C}$ . This is simply due to swelling of poly(NIPAM) in cold water ( $4^\circ\text{C}$ ) and shrinkage in hot water ( $40^\circ\text{C}$ ), an inherent property of poly(NIPAM) irrespective of fiber alignment direction.  $4$  and  $40^\circ\text{C}$  were arbitrarily chosen as two temperatures below and above the LCST ( $26^\circ\text{C}$ ) of poly(NIPAM) fibrous mat as observed by micro-DSC [188]. In short, there are two different processes: (1) from as spun (dry) state to wet and (2) from wet (hot) to wet (cold) and vice versa. The first process decides the shape and is irreversible. The second process decides the tube size and is reversible.

The same behavior, i.e., movement along fiber alignment, was observed in other samples with one layer made up of randomly arranged fibers and another layer with fiber alignments perpendicular and  $45^\circ$  (Bi-PNIPAM- $90^\circ$  and Bi-PNIPAM- $45^\circ$ ) (Figure 4.1-b). In case of PNIPAM- $45^\circ$ , compared to the random layer (mono-ran-PNIPAM), on going from dry as spun fibers to wet state at  $40^\circ\text{C}$ , the dimensional change (shrinkage) of aligned layer along the fiber orientation (diagonal D2) dominated that along the direction perpendicular to the fiber orientation (diagonal D1) (Figure 4.5, Supporting Information) leading to a helix with the randomly aligned fibrous layer outside. Also, Bi-PNIPAM- $90^\circ$  showed bilayer movement along the direction of fiber alignment due to the combined effect of the anisotropic  $E$  modulus and asymmetrical differential change in length and width as explained above for Bi-PNIPAM- $0^\circ$  sample. The width of PNIPAM- $90^\circ$  decreased by  $\approx 35\%$  whereas monoran-PNIPAM

Table 4.1 Size change of poly(NIPAM) fiber mats with different alignment of fibers in water at different temperatures ( $40$  and  $4^\circ\text{C}$ ). The similar mats were used in the previous work for getting reversible thermoresponsive actuation in shape by making bicomponent mats.

	$0^\circ$			$45^\circ$			$90^\circ$			Random		
	As-spun	$40^\circ\text{C}$	$4^\circ\text{C}$	As-spun	$40^\circ\text{C}$	$4^\circ\text{C}$	As-spun	$40^\circ\text{C}$	$4^\circ\text{C}$	As-spun	$40^\circ\text{C}$	$4^\circ\text{C}$
$L[\text{cm}]$	1.9670	1.3190	1.8500	2.0050	1.8310	2.6170	2.1015	2.3550	3.5080	2.1170	1.8870	2.7100
$W[\text{cm}]$	0.5240	0.6200	0.9320	0.5240	0.4640	0.6770	0.5165	0.3355	0.4985	0.5390	0.4790	0.6690
$D_1[\text{cm}]$	2.0410	1.4470	2.0490	2.0710	2.0860	3.0410	2.1630	2.3710	3.5480	2.1930	1.9560	2.7770
$D_2[\text{cm}]$	2.0480	1.4540	2.0710	2.0730	1.6560	2.3640	2.1700	2.3760	3.5340	2.1810	1.9480	2.7830

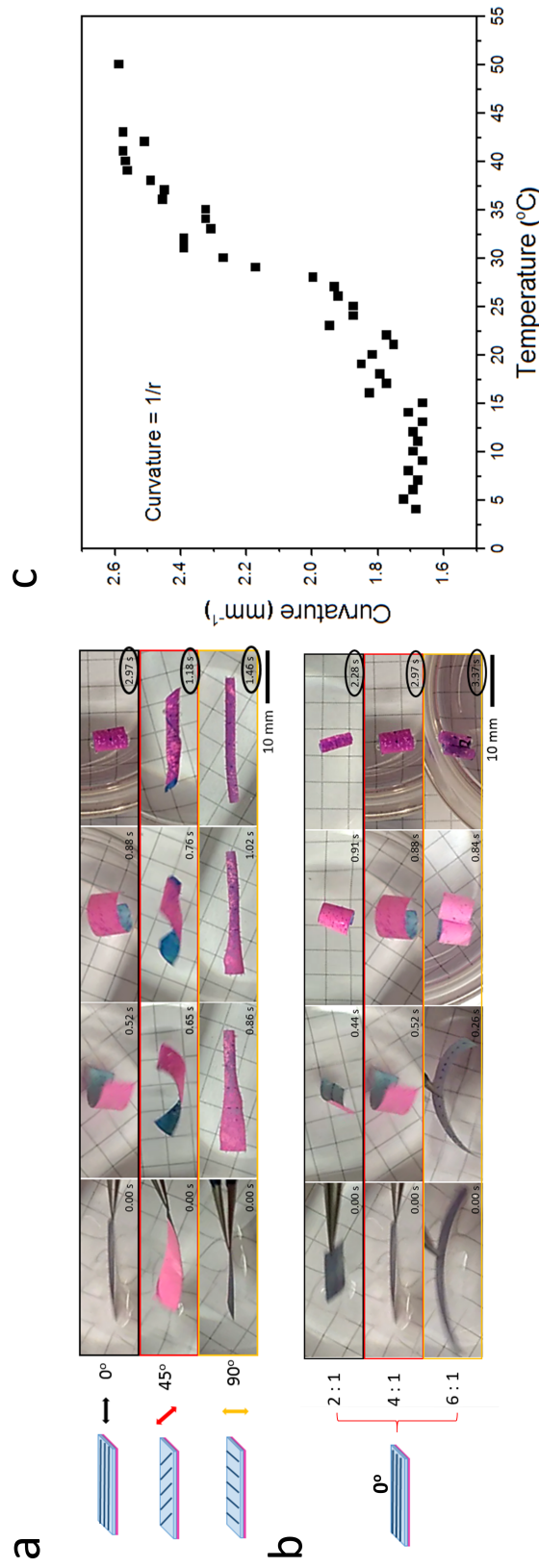


Fig. 4.2 Actuation process and effect of temperature. a) Actuation process of Bi-PNIPAM-0°, Bi-PNIPAM-45°, Bi-PNIPAM-90° mats (thickness ratio: 0.65 (aligned/random);  $L : W = 4 : 1$ ) with time in water at 40 °C; b) Size-dependent actuation process of Bi-PNIPAM-0° mats (thickness ratio: 0.65 (Aligned/random)) with time in water at 40 °C. L:W ratios were 2:1, 4:1, and 6:1; c) The effect of temperature of water on the curvature of Bi-PNIPAM-0° mat with the thickness ratio (aligned/random) of 0.65.

showed only 11% shrinkage. The differential shrinkage in width led to the formation of a tube by rolling along the fiber alignment, i.e., perpendicular to the long axis. Shape changes in all these cases were very fast in less than 3s depending upon the direction of fiber alignment due to highly porous membranes. Fast shape change is also possible even for larger size samples. 2.28, 2.97, and 3.37 s, respectively were required for Bi-PNIPAM-0° (thickness ratio (aligned:bilayer) 0.65) samples with ratio of  $L : W$  2 : 1, 4 : 1, and 6 : 1 at 40°C, respectively (Figure 4.2-a,b).

Furthermore, the effect of temperature on rolling behavior was studied for Bi-PNIPAM-0° by following the curvature. The rolling took place on placing the as spun dry sample in water at all temperatures between 4 and 40°C. There was a significant increase in curvature on going from 23 to 37°C and the change was maximum at 26°C, the cloud point of poly(NIPAM) fibrous mat (Figure 4.2-c).

In Figure 4.3, we show that the curvature normalized by the total thickness reaches its maximum point when the thickness ratio is around 0.48 and decreases again afterward. A reminiscent behavior with zero curvature for the extreme thickness ratios of 0 (random layer only) and 1 (aligned layer only) together with a maximum in between occurs in metallic bilayers under thermal expansion [117]. A similar trend was seen in samples with high aspect ratio ( $L/W = 4 : 1$ ) (Figure 4.7, Supporting Information). The difference was a complete rolling instead of merely a bending on increasing the  $L/W$  ratio.

In order to demonstrate that the observed results can indeed be understood properly by a combination of thermal expansion and elastic deformation, we conduct finite element simulations using the Abaqus software package (see Methods for details in Supporting Information). These allow us to predict the equilibrium shape of the bilayer mats after complete swelling/shrinking. The poly(NIPAM) layers are modeled as elastic materials whose swelling/shrinking is accounted for by an effective expansion coefficient. The aligned layer is an anisotropic material with expansion coefficients  $\alpha_{along} = -0.3$  and  $\alpha_{perp} = 0.2$  in direction along and perpendicular to the fiber orientation, respectively, as obtained from Figure 4.5 in the Supporting Information and Table-4.1. The elastic moduli are similarly anisotropic with  $E_{along}/E_{perp} = 50$  as measured in Figure 4.6 in the Supporting Information. The random layer is isotropic with  $\alpha_{random} = -0.1$  and  $E_{along}/E_{random} = 5/3$ .

Figure 4.1-c shows the numerically obtained structures for the mats with fibers aligned at 0°, 45°, and 90° in one of the layers corresponding to the experimental images in Figure 4.1-b. For 0° and 90° we observe rolling in fiber direction and for 45° a helical structure is found in very good agreement with experimental observations. In contrast, considering only anisotropic expansion combined with isotropic elasticity leads to shapes which are in clear disagreement with the experimental observations (Figure 4.8, Supporting Information).

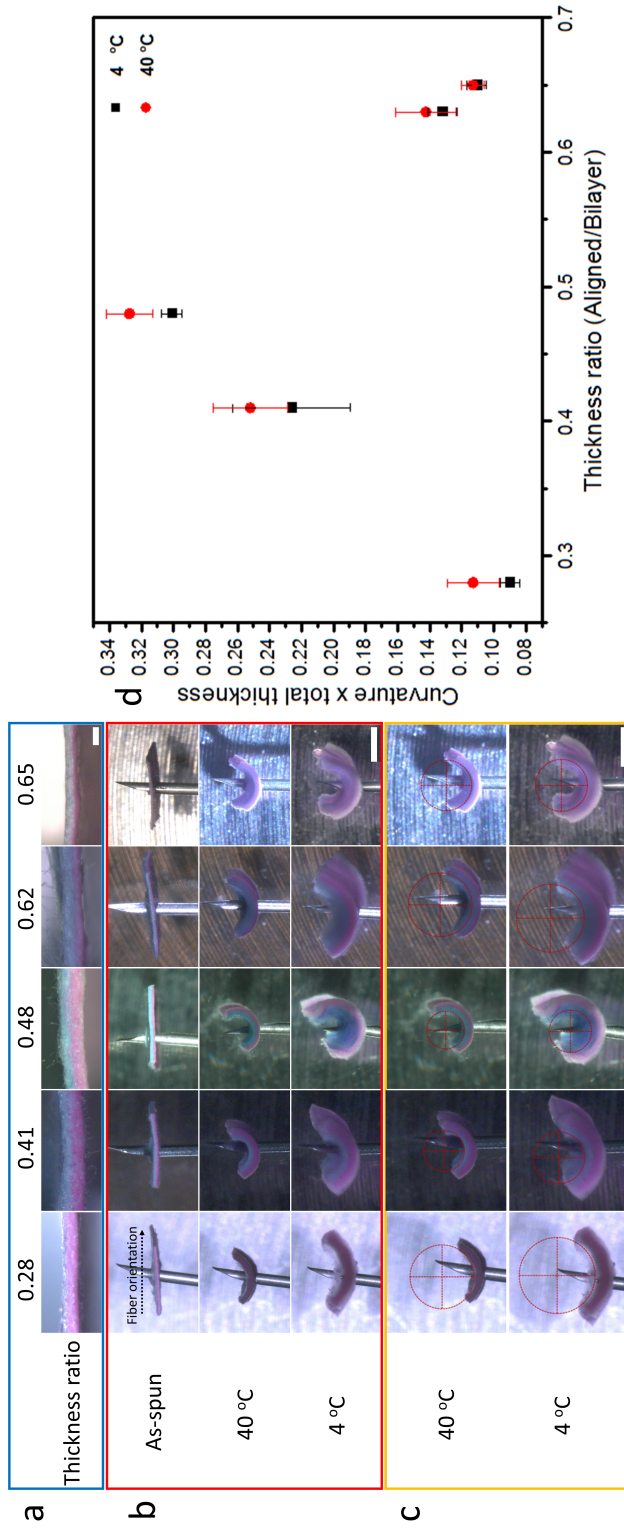


Fig. 4.3 Effect of thickness ratio (aligned/random) on “curvature  $\times$  total thickness” of Bi-PNIPAM-0° mats (size:  $L : W = 2 \text{ mm} : 3.5 \text{ mm}$ ) in water at different temperatures. a) Cross-section of Bi-PNIPAM-0° samples with different thickness ratio (blue side is aligned layer; scale bar =  $100 \mu\text{m}$ ); b) in water at different temperatures (scale bar =  $1 \text{ mm}$ ); c) radius ( $r$ ) determination (scale bar =  $1 \text{ mm}$ ); d) “curvature  $\times$  total thickness” against thickness ratio of aligned/random. The curvature is taken as  $1/r$ .

This lends strong support to our hypothesis that the observed actuation is indeed due to a combination of an anisotropic expansion with an equally important anisotropy in the elastic modulus.

In conclusion, we present a rare example of a one-component dual actuator with very fast irreversible actuation (1 – 3 s) to direction controlled 3D tubular forms and almost instant reversible size actuation with temperature in contact with water. The 3D structures kept their form in water at temperatures 4 – 40°C with reversible change in size. The actuator is a porous fibrous poly(NIPAM) membrane in which asymmetry in swelling/shrinkage required for irreversible actuation in form is created along the membrane thickness by fiber alignment and direction dependent  $E$  modulus. The actuation in size of 3D tubular forms is due to thermoresponsive nature of poly(NIPAM). The actuator can be made in any dimensions and validated by numerical simulations. This work opens up new perspectives of formation of 3D structures by external stimuli with reversible actuation in size without destroying the form useful for creating externally controlled 3D structures, scaffolds for tissue engineering, complex patterns for multi-cell culture, for example.

### Supporting Information

Supporting Information is available from the Wiley Online Library or from the author.

### Acknowledgements

The authors would like to acknowledge financial support from Deutsche Forschungsgemeinschaft (DFG; SFB 840). L.L. thanks China Scholarship Council for awarding fellowship for carrying out PhD in Germany in the lab of Prof. Seema Agarwal. SG and AG thank the Volkswagen Foundation for financial support.

## 4.2 Supplementary information

**Materials** Photo cross-linker 4-acryloylbenzophenone (ABP) was used and P(NIPAM-ABP) ( $M_n = 7.0 \times 10^4 \text{ g/mol}$ ,  $M_w = 2.0105 \text{ g/mol}$ ) was made as described in ref [197]. Preparation of fibrous mats: All fibrous mats were made by electrospinning of P(NIPAM-ABP) using DMF as solvent. The electrospinning conditions were presented in Table.4.2. For obtaining the color contrast in the bilayer fibrous mat, with respect to the weight of P(NIPAM-ABP), an amount of 0.4 wt% of methylene blue (MB) and Rhodamine B (RB) were added into the solutions to get the aligned and random fibrous mats, respectively. The fibers collected by a horizontally rotating disc of diameter 13 cm at 30 rpm formed the random fibrous mat and that collected by a vertically rotating disc of diameter 20 cm and a disc rim of 4 cm with a rotating speed of 800 rpm formed the aligned fibrous mat. After that, the random and aligned fibrous mats were pressed together under 300 bars for 20 min, at room temperature, followed by photo cross-linking under UV-lamp (Honle UVAHAND 250 GS) for 4 hours.

**Finite element simulations** Bilayer mats are simulated using ABAQUS version 6.14. The mats are meshed using three dimensional, general purpose brick elements, C3D8R, for linearly elastic (but anisotropic) materials. This method solves the elastic equations such that the equilibrium shape is obtained. The layers are tied to each other with a no slip boundary condition at their interface. No further restrictions are imposed on the free movements of the mats.

Our goal here is to model the irreversible rolling when the fibrous mats are taken from the dry state into the 40°C water. The water influx into the porous medium follows a very complicated time dynamics. Luckily, however, it is not necessary to model this influx in full detail in order to obtain an understanding of the final rolled shape. Therefore, the explicit time dynamics of water influx is not included. Instead, we model the swelling/shrinkage of the material by using ABAQUS' possibility of modeling material expansion. The total

length change of each layer was anisotropic with swelling/shrinkage ratios  $\alpha$  whose values are given in the main text. Including expansion also in the vertical direction does not lead to significant changes. The shape change is achieved by going from the dry to the 40°C wet state in small increments the number of which is determined automatically so as to ensure numerical convergence.

ABAQUS is capable of treating anisotropic materials whose elastic  $E$  moduli differ in different directions (the values are given in the main text). The shear modulus is always isotropic with  $E_{random}/G = 3$  and Poisson's ratios are  $\nu_{along, perp} = \nu_{along, z} = \nu_{perp, z} = 0.3$  for the aligned layer and  $\nu_{random} = 0.3$  for the random layer. Varying both quantities does not lead to appreciable differences in the results. In the simulation, the thickness of both mats is 30  $\mu m$ . To obtain a clear illustration of the bending effects without interpenetration of the mats, the sizes of the mats are chosen as 1600  $\times$  500  $\mu m$  for the 0°, 2000  $\times$  500  $\mu m$  for the 45° and 2000  $\times$  1000  $\mu m$  for the 90° mat.

**Characterization** Gel permeation chromatography (GPC) was used to determine the molecular weight of P(NIPAM-ABP) by using DMF as the eluent at a flow rate of 0.5  $\frac{mL}{min}$  at 25°C. A scanning electron microscope (SEM) (Phenom Pro, Phenomworld) was used to study the diameter and morphology of fibers. The quantified analysis of dimension change was carried out by a software of Image J. A software named Video Remaker was chosen to capture photos. And according to the previous literatures, the alignment degree was based on the following formula:[198]

$$d_{Fa} = \frac{3\cos^2(\theta) - 1}{2} \quad (4.1)$$

where  $\theta$  is the angle between the individual fiber and the rotating direction of the collector. The given values are based on an average of 100 fibers. The porosity (P) of the random and aligned fibrous mats were calculated by the equations of 4.2, 4.3, 4.4:

$$\rho_{mat} = \frac{mass_{mat}}{area_{mat} \times thickness_{mat}} \quad (4.2)$$

$$\rho_{film} = \frac{mass_{film}}{area_{film} \times thickness_{film}} \quad (4.3)$$

$$P = \left(1 - \frac{\rho_{mat}}{\rho_{film}}\right) \times 100\% \quad (4.4)$$

where  $\rho_{film}$  = film density and  $\rho_{mat}$  = density of cross-linked electrospun mats, respectively. The quantified analysis (swelling ratio  $q$ ) of dimension change was carried out by the

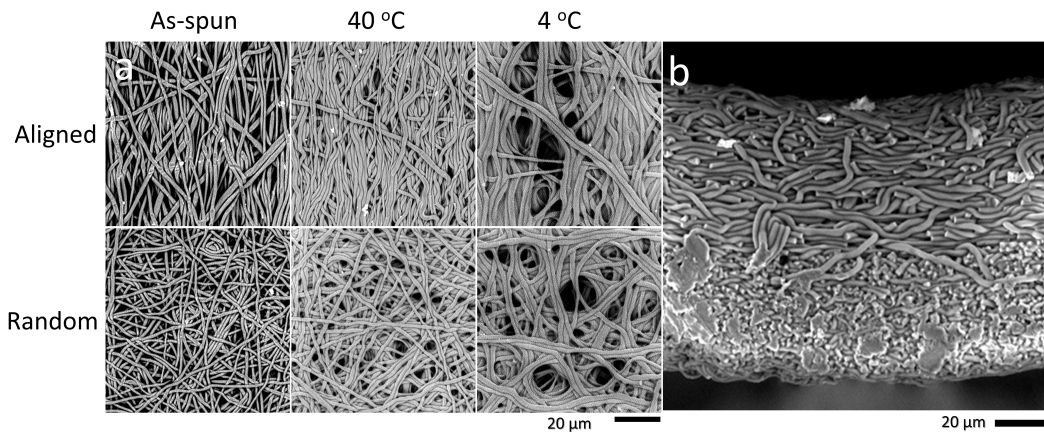


Fig. 4.4 SEM images of a) aligned and random mats in water at different temperatures, b) the cross-section of the Bi-PNIPAM-0° mat in water at 40°C after drying shows a strong interface between aligned (upper side) and random (bottom side) fibrous layers. Scale bar = 20  $\mu m$ .

formula (5):

$$q = \frac{L_A - L_B}{L_B} \quad (4.5)$$

where  $L_A$  and  $L_B$  are the sizes of the pressed cross-linked aligned or random fibrous mats which was after transferred and before transferred size (regarding to length, width and diagonal), respectively.

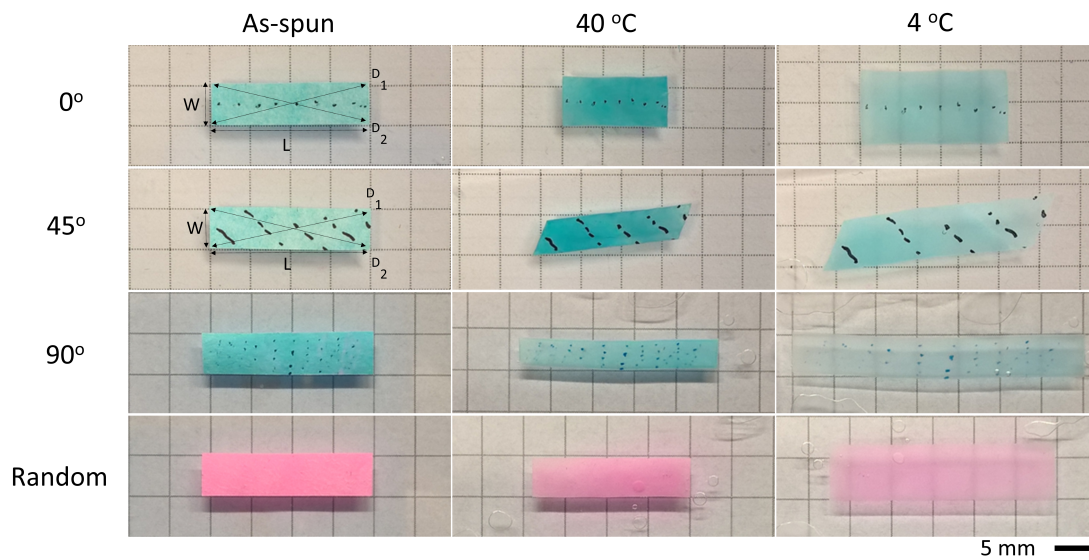


Fig. 4.5 The size change of aligned and random cross-linked fibrous mats (original size:  $2.0\text{ cm} \times 0.5\text{ cm}$ ) in water at different temperatures. The similar experiment was done previously for making bicomponent actuators [188].

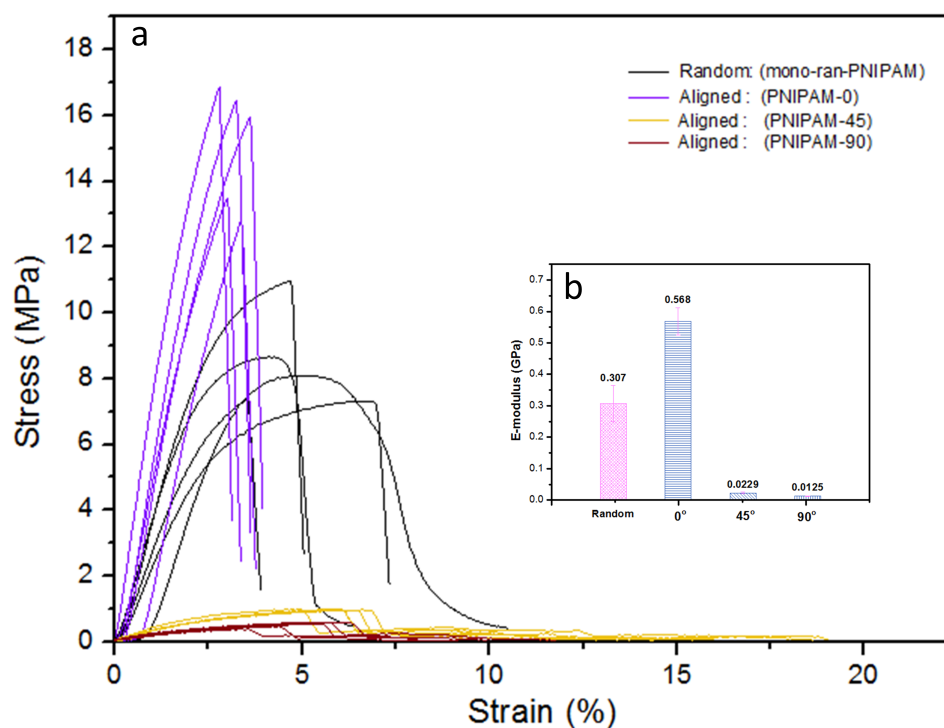


Fig. 4.6 a) strain-stress curve and b)  $E$  modulus of pressed cross-linked one-component Bi-PNIPAM-0°, 45°, 90° samples.

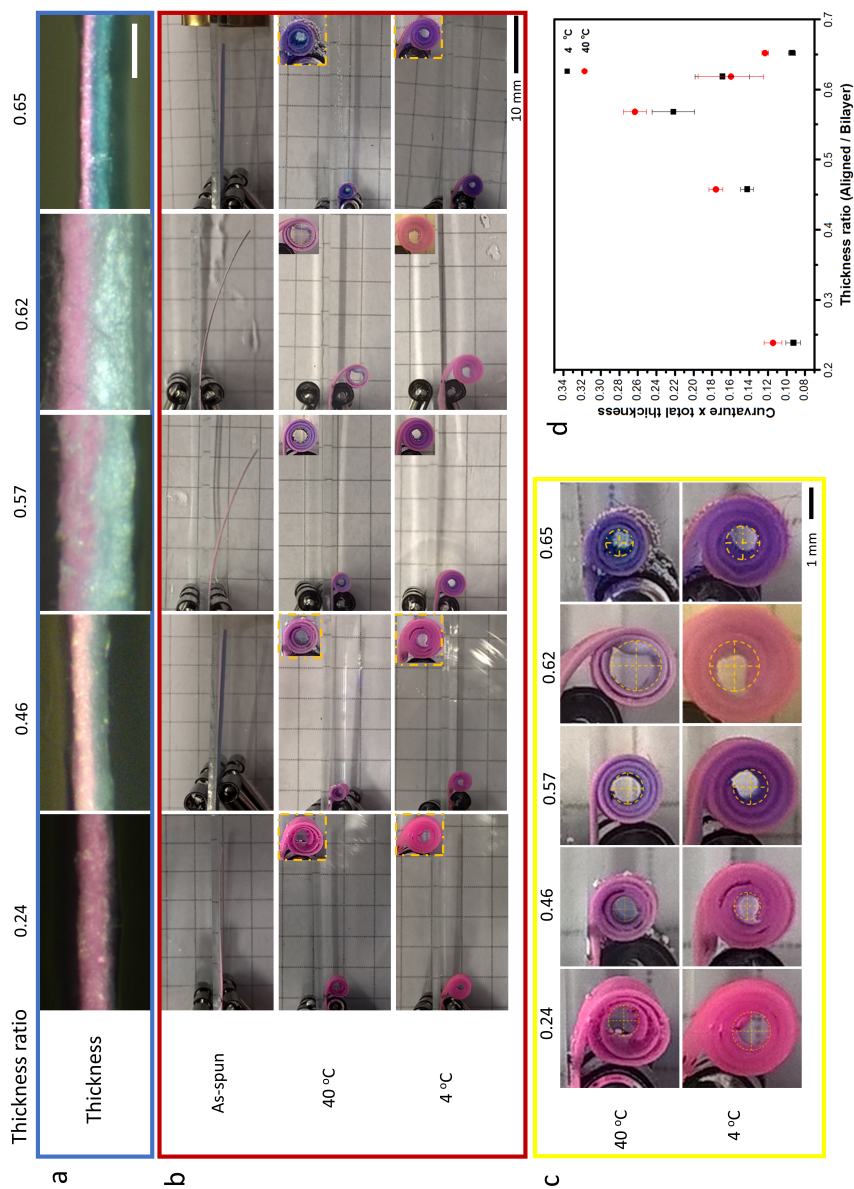


Fig. 4.7 Effect of thickness ratio (aligned / bilayer) on “curvature  $\times$  bilayer total thickness” of Bi-PNIPAM-0° mats ( $20\text{ mm} \times 5\text{ mm}$ ) in water at different temperatures. a) Cross-section of Bi-PNIPAM-0° samples with different thickness ratio (blue side is aligned layer; scale bar =  $100\ \mu\text{m}$ ); b) In water with different temperatures (scale bar =  $10\text{ mm}$ ); c) radius ( $r$ ) determination (scale bar =  $1\text{ mm}$ ); d) Curve of “curvature  $\times$  bilayer total thickness” against thickness ratio of Aligned / Bilayer. The curvature is taken as  $1/r$ .



Fig. 4.8 Equilibrium shapes of the  $0^\circ$ ,  $45^\circ$  and  $90^\circ$  bilayer mats from finite element simulations analogous to Figure 4.1-c of the main text, but with the oversimplifying assumption of an isotropic elastic modulus in both layers. Comparison with Figure 4.1 of the main text clearly demonstrates that this simple model is not able to reproduce the experimentally observed shapes. The size of the mats is  $1600 \times 500 \mu m$  for the  $0^\circ$  and  $45^\circ$  and  $800 \times 500 \mu m$  for  $90^\circ C$  mat.

Table 4.2 The electrospinning parameters used for making fibrous membranes. DMF was used as solvent.

	Solution concentration 00- [wt %]	Voltage [KV] [ml/h]	Flow Rate [ml]	Spinning Volume [mm]	Needle diameter [cm]	Collecting distance
Aligned Mat	40	-2.4-17.0	1.3	2.5	0.6	15
Random Mat	40	0-16.0	1.3	1	0.6	20

# References

- [1] I. Carvalho, B. Estevinho, and L. Santos, "Application of microencapsulated essential oils in cosmetic and personal health care products - a review," *Int. J. Cosmet. Sci.*, vol. 38, pp. 109–19, 2016.
- [2] A. Noda, M. Yamaguchi, M. Aizawa, and Y. Kumano, "Cosmetic containing fine soft microcapsules," no. Patent US 5089269 A, 18. Feb. 1992.
- [3] R. J. Norbury, R. W. H. Chang, and L. C. Zeller, "Encapsulated cosmetic materials and process of making," no. Patent US 5013473 A, 7. May 1991.
- [4] R. Charle, G. Kalopissis, and C. Zviak, "Cosmetic makeup removing or treating composition which is microencapsulated and incorporated in a flexible support," no. Patent US 3691270 A, 12. Sept. 1972.
- [5] S. Magdassi and E. Tuitou, "Novel cosmetic delivery systems," *Marcel Dekker, Inc.*, 1999.
- [6] F. Casanova and L. Santos, "Encapsulation of cosmetic active ingredients for topical application – a review," *J Microencapsul.*, vol. 33, pp. 1–17, 2016.
- [7] E. Jahns, D. Boeckh, W. Bertleff, and P. Neumann, "Microcapsule preparations and detergents and cleaning agents containing microcapsules," no. Patent US 6951836 B2, 2000.
- [8] B. Giesen, M. Wortmann, and D. Zaika, "Hand dish washing detergent with microcapsules," no. WO 2000065020 A1, 2 Nov. 2000.
- [9] W. R. Michael, "Perfume microcapsules for use in granular detergent compositions," no. Patent EP 0376385 A2, 4. Juli 1990.
- [10] M. Giamberini, S. F. Prieto, and B. Tylkowski, "Microencapsulation: Innovative applications," *Walter de Gruyter GmbH*, 2015.
- [11] S. K. Ghosh, "Functional coatings: By polymer microencapsulation," *Wiley-VCH Verlag GmbH and Co. KGaA*, 2006.
- [12] H. J. Kwon and P.-Y. B. Jar, "On the application of fem to deformation of high-density polyethylene," *International Journal of Solids and Structures*, vol. 45, pp. 3521–3543, 2008.

- [13] H. E. H. Meijer, L. E. Govaert, and R. J. M. Smit, "Chapter 4: A multi-level finite element method for modeling rubber-toughened amorphous polymers," *ACS Symposium Series*, vol. 759, pp. 50–70, 2000.
- [14] H. Jiang, G. T. Lim, J. N. Reddy, J. D. Whitcomb, and H.-J. Sue, "Finite element method parametric study on scratch behavior of polymers," *Journal of Polymer Science Part B: Polymer Physics*, vol. 45, p. 1435–1447, 2007.
- [15] M. Kubica and W. Skoneczny, "The finite element method in tribological studies of polymer materials in tribo-pair with the oxide layer," *Tribology Letters*, vol. 52, pp. 381–393, 2013.
- [16] A. Alberich-Bayarri, D. Moratal, J. Ivirico, J. Hernández, A. Vallés-Lluch, L. Martí-Bonmatí, J. Estellés, J. Mano, M. Pradas, J. Ribelles, and M. Salmerón-Sánchez, "Microcomputed tomography and microfinite element modeling for evaluating polymer scaffolds architecture and their mechanical properties.," *Journal of Biomedical Materials Research Part B: Applied Biomaterials*, vol. 91, pp. 191–202, 2009.
- [17] W. Wang, K. Sadeghipour, and G. Baran, "Finite element analysis of the effect of an interphase on toughening of a particle reinforced polymer composite," *Composites Part A: Applied Science and Manufacturing*, vol. 39, pp. 956–964, 2008.
- [18] J. L. Bucaille, E. Felder, and G. Hochstetter, "Experimental and three-dimensional finite element study of scratch test of polymers at large deformations," *Journal of Tribology*, vol. 126, pp. 372–379, 2004.
- [19] M. Solar, H. Meyer, C. Gauthier, C. Fond, O. Benzerara, R. Schirrer, and J. Baschnagel, "Mechanical behavior of linear amorphous polymers: comparison between molecular dynamics and finite-element simulations.," *Phys. Rev E*, vol. 85, pp. 021808–1–14, 2012.
- [20] B. Marvalova and I. Petrikova, "Constitutive models for rubber ix," *CRC Press*, 2015.
- [21] V. Prasad, A. Joy, G. Venkatachalam, S. Narayanan, and S. Rajakumarb, "Finite element analysis of jute and banana fibre reinforced hybrid polymer matrix composite and optimization of design parameters using anova technique," *Procedia Engineering*, vol. 97, pp. 1116–1125, 2014.
- [22] J. Pyo, T. Lee, C. Kim, M. S. Kim, and T. Kim, "Prediction of time-dependent swelling of flexible polymer substrates using hygro-mechanical finite element simulations," *Soft Matter*, vol. 12, pp. 4135–4141, 2016.
- [23] J. Hu, H. Chen, and Z. Zhang, "Mechanical properties of melamine formaldehyde microcapsules for self-healing materials," *Materials Chemistry and Physics*, vol. 118, no. 1, pp. 63–70, 2009.
- [24] G. Gouadec, K. Carlisle, K. Chawla, M. Koopman, G. Gladysz, and M. Lewis, "Nano-compression of carbon micro-balloons with a flat-ended cylindrical indenter," *Indentation Techniques in Ceramic Materials Characterization*, vol. 156, pp. 143–152, 2004.

- [25] K. B. Carlisle, K. K. Chawla, G. M. Gladysz, and M. Koopman, "Structure and mechanical properties of micro and macro balloons: An overview of test techniques," *J MATER SCI*, vol. 41, pp. 3961–3972, 2006.
- [26] R. Mercadé-Prieto, R. Allen, D. York, J. A. Preece, T. E. Goodwin, and Z. Zhang, "Compression of elastic-perfectly plastic microcapsules using micromanipulation and finite element modelling: Determination of the yield stress," *Chemical Engineering Science*, vol. 66, pp. 1835–1843, 2011.
- [27] J. Stenson, C. Thomas, and P. Hartley, "Modelling the mechanical properties of yeast cells," *Chem. Eng. Sci.*, vol. 64, no. 8, pp. 1892–1903, 2009.
- [28] V. Nguyen, C. X. Wang, C. R. Thomas, and Z. Zhang, "Mechanical properties of single alginate microspheres determined by microcompression and finite element modelling," *Chem. Eng. Sci.*, vol. 64, no. 5, pp. 821–829, 2009.
- [29] R. Mercadé-Prieto, R. Allen, Z. Zhang, D. York, J. A. Preece, and T. E. Goodwin, "Failure of elastic-plastic core-shell microcapsules under compression," *AIChE J.*, vol. 58, pp. 2674–2681, Dec. 2012.
- [30] X. Pan, R. Mercadé-Prieto, D. York, J. A. Preece, and Z. Zhang, "Structure and mechanical properties of consumer-friendly pmma microcapsule," *Ind. Eng. Chem. Res.*, vol. 52, pp. 11253–11265, 2013.
- [31] D. Vella, A. Ajdari, A. Vaziri, and A. Boudaoud, "The indentation of pressurized elastic shells: from polymeric capsules to yeast cells," *Journal of The Royal Society Interface*, vol. 9, no. 68, pp. 448–455, 2012.
- [32] A. Ghaemi, A. Philipp, A. Bauer, K. Last, A. Fery, and S. Gekle, "Mechanical behaviour of micro-capsules and their rupture under compression," *Chem. Eng. Sci.*, vol. 142, pp. 236–243, Mar. 2016.
- [33] L. Sagis, "Microencapsulation and microspheres for food applications," *Academic Press*, 2015.
- [34] S. Tan, S. Mettu, M. D. Biviano, M. Zhou, B. Babgi, J. White, R. R. Dagastine, and M. Ashokkumar, "Ultrasonic synthesis of stable oil filled microcapsules using thiolated chitosan and their characterization by afm and numerical simulations," *Soft Matter*, vol. 12, pp. 7212–7222, 2016.
- [35] A. Fery and R. Weinkamer, "Mechanical properties of micro- and nanocapsules: Single-capsule measurements," *Polymer*, vol. 48, pp. 7221–7235, 2007.
- [36] L. Zhang, M. D'Acunzi, M. Kappl, A. Imhof, A. van Blaaderen, H. Butt, R. Graf, and D. Vollmer, "Tuning the mechanical properties of silica microcapsules," *Phys. Chem. Chem. Phys.*, vol. 12, p. 15392–15398, 2010.
- [37] H. Ejima, N. Yanai, J. P. Best, M. Sindoro, S. Granick, and F. Caruso, "Near-incompressible faceted polymer microcapsules from metal-organic framework templates," *Adv. Mat.*, vol. 25, p. 5767–5771, 2013.

- [38] E. Reissner, "Stresses and small displacements of shallow spherical shells," *J. Math. Phys.*, vol. 25, pp. 80–85, 1946.
- [39] E. Reissner, "Stresses and small displacements of shallow spherical shells ii," *J. Math. Phys.*, vol. 25, pp. 279–300, 1946.
- [40] "Abaqus documentation," *Dassault Systemes, Providence, RI, USA*.
- [41] R. Mercadé-Prieto, B. Nguyen, R. Allen, D. York, J. A. Preece, T. E. Goodwin, and Z. Zhang, "Determination of the elastic properties of single microcapsules using micromanipulation and finite element modeling," *Chem. Eng. Sci.*, vol. 66, pp. 2042–2049, 2011.
- [42] A. B. Strong, "Plastics: Materials and processing," *Prentice Hall, Inc.*, 1996.
- [43] S. Jabbari-Farouji, J. Rottler, O. Lame, A. Makke, M. Perez, and J. L. Barrat, "Plastic deformation mechanisms of semicrystalline and amorphous polymers," *ACS Macro Letters*, vol. 4, pp. 147–150, 2015.
- [44] G. Kaufman, S. Nejati, R. Sarfati, R. Boltyanskiy, M. Loewenberg, E. Dufresne, and O. Osuji, "Soft microcapsules with highly plastic shells formed by interfacial polyelectrolyte–nanoparticle complexation," *Soft Matter*, vol. 11, no. 38, pp. 7478–7482, 2015.
- [45] I. H. Shames and F. A. Cozzarelli, "Elastic and inelastic stress analysis," *Taylor & Francis*, 1997.
- [46] G. Sun and Z. Zhang, "Mechanical strength of microcapsules made of different wall materials," *International Journal of Pharmaceutics*, vol. 242, pp. 307–311, 2002.
- [47] L. Sperling, "Introduction to physical polymer science," *John wiley & Sons*, 2006.
- [48] R. von Mises, "Mechanik der festen körper in plastisch-deformablen zustand," *Nachr. Ges. Wiss. Gottingen, Math.-phys. Klasse 4*, pp. 582–592, 1913.
- [49] G. Taylor and H. Quinney, "The plastic distortion of metals," *Phil. Trans. R. Soc.*, vol. 230, pp. 323–362, 1931.
- [50] G. Swallowe, "Mechanical properties and testing of polymers: An a–z reference," *Springer Science & Business Media*, 1999.
- [51] I. M. Ward, "Review: The yield behaviour of polymers," *J. Mat. Sci.*, vol. 6, pp. 1397–1417, 1971.
- [52] I. Ward and J. Sweeney, "An introduction to the mechanical properties of solid polymers," *John Wiley & Sons, Ltd*, 2004.
- [53] R. Raghava and R. M. Caddell, "The macroscopic yield behaviour of polymers," *J. Mater. Sci.*, vol. 8, pp. 225–232, 1973.
- [54] S. Lampman, "Characterization and failure analysis of plastics," *ASM International*, 2003.

- [55] M. Vogler, S. Kolling, and A. Haufe, “A constitutive model for polymers with a piecewise linear yield surface,” *Proc. Appl. Math. Mech.*, vol. 6, pp. 275–276, 2006.
- [56] J. Rottler and M. O. Robbins, “Yield conditions for deformation of amorphous polymer glasses,” *Phys. Rev. E*, vol. 64, pp. 051801:1–8, 2001.
- [57] E. Jaramillo, N. Wilson, S. Christensen, J. Gosse, and A. Strachan, “Energy-based yield criterion for pmma from large-scale molecular dynamics simulations,” *Phys. Rev. B*, vol. 85, pp. 024114:1–7, 2012.
- [58] H. Altenbach and K. Tushte, “A new static failure criterion for isotropic polymers,” *Mech. Compos. Mater.*, vol. 37, p. 475–482, 2001.
- [59] E. Arruda, M. C. Boyce, and R. Jayachandran, “Effects of strain rate, temperature and thermomechanical coupling on the finite strain deformation of glassy polymers,” *Mechanics of Materials*, vol. 19, pp. 193–212, 1995.
- [60] W. Michaeli and M. Glissmann, “Investigation and measurement of the true stress/strain behaviour of semi-crystalline thermoplastics,” *Macromolecular Materials and Engineering*, vol. 284–285, pp. 19–24, 2000.
- [61] R. S. Hoy and M. O. Robbins, “Strain hardening of polymer glasses: Effect of entanglement density, temperature, and rate,” *Journal of Polymer Science Part B: Polymer Physics*, vol. 44, pp. 3487–3500, 2006.
- [62] D. Xu and S. L. Craig, “Strain hardening and strain softening of reversibly cross-linked supramolecular polymer networks,” *Macromolecules*, vol. 44, pp. 7478–7488, 2011.
- [63] R. Hiss, S. Hobeika, C. Lynn, and G. Strobl, “Network stretching, slip processes, and fragmentation of crystallites during uniaxial drawing of polyethylene and related copolymers. a comparative study,” *Macromolecules*, vol. 32, pp. 4390–4403, 1999.
- [64] D. Barthès-Biesel, “Motion and Deformation of Elastic Capsules and Vesicles in Flow,” *Annu. Rev. Fluid Mech.*, vol. 48, pp. 25–52, Jan. 2016.
- [65] G. Boedec, M. Leonetti, and M. Jaeger, “Isogeometric FEM-BEM simulations of drop, capsule and vesicle dynamics in Stokes flow,” *J. Comput. Phys.*, vol. 342, pp. 117–138, Aug. 2017.
- [66] C. Schaaf and H. Stark, “Inertial migration and axial control of deformable capsules,” *Soft Matter*, vol. 13, pp. 3544–3555, May 2017.
- [67] Z. Y. Luo and B. F. Bai, “Dynamics of nonspherical compound capsules in simple shear flow,” *Phys. Fluids*, vol. 28, pp. 101901–18, Oct. 2016.
- [68] Z. Wang, Y. Sui, A. V. Salsac, D. Barthès-Biesel, and W. Wang, “Motion of a spherical capsule in branched tube flow with finite inertia,” *J. Fluid Mech.*, vol. 806, pp. 603–626, Oct. 2016.
- [69] C. Dupont, F. Delahaye, D. Barthès-Biesel, and A. V. Salsac, “Stable equilibrium configurations of an oblate capsule in simple shear flow,” *J. Fluid Mech.*, vol. 791, pp. 738–757, Feb. 2016.

- [70] H.-H. Boltz and J. Kierfeld, “Shapes of sedimenting soft elastic capsules in a viscous fluid,” *Phys. Rev. E*, vol. 92, pp. 033003–16, Sept. 2015.
- [71] L. Zhu, J. Rabault, and L. Brandt, “The dynamics of a capsule in a wall-bounded oscillating shear flow,” *Phys. Fluids*, vol. 27, pp. 071902–16, July 2015.
- [72] Z. Y. Luo, L. He, and B. F. Bai, “Deformation of spherical compound capsules in simple shear flow,” *J. Fluid Mech.*, vol. 775, pp. 77–104, June 2015.
- [73] D. Matsunaga, Y. Imai, T. Yamaguchi, and T. Ishikawa, “Deformation of a spherical capsule under oscillating shear flow,” *J. Fluid Mech.*, vol. 762, pp. 288–301, Dec. 2014.
- [74] A. Yazdani and P. Bagchi, “Influence of membrane viscosity on capsule dynamics in shear flow,” *J. Fluid Mech.*, vol. 718, pp. 569–595, Feb. 2013.
- [75] D. Abreu and U. Seifert, “Effect of thermal noise on vesicles and capsules in shear flow,” *Phys. Rev. E*, vol. 86, p. 010902, July 2012.
- [76] W.-X. Huang, C. B. Chang, and H. J. Sung, “Three-dimensional simulation of elastic capsules in shear flow by the penalty immersed boundary method,” *J. Comput. Phys.*, vol. 231, pp. 3340–3364, Apr. 2012.
- [77] P. M. Vlahovska, Y. N. Young, G. Danker, and C. Misbah, “Dynamics of a non-spherical microcapsule with incompressible interface in shear flow,” *J. Fluid Mech.*, vol. 678, pp. 221–247, Apr. 2011.
- [78] S. K. Veerapaneni, Y. N. Young, P. M. Vlahovska, and J. Bławdziewicz, “Dynamics of a Compound Vesicle in Shear Flow,” *Phys. Rev. Lett.*, vol. 106, pp. 158103–4, Apr. 2011.
- [79] M. Zhao and P. Bagchi, “Dynamics of microcapsules in oscillating shear flow,” *Phys. Fluids*, vol. 23, no. 11, p. 111901, 2011.
- [80] X. Q. Hu, A. V. Salsac, and D. Barthès-Biesel, “Flow of a spherical capsule in a pore with circular or square cross-section,” *J. Fluid Mech.*, vol. 705, pp. 176–194, Dec. 2011.
- [81] S. Knoche and J. Kierfeld, “Buckling of spherical capsules,” *Phys. Rev. E*, vol. 84, pp. 046608–13, Oct. 2011.
- [82] S. J. Shin and H. J. Sung, “Inertial migration of an elastic capsule in a Poiseuille flow,” *Phys. Rev. E*, vol. 83, pp. 046321–13, Apr. 2011.
- [83] R. Finken, S. Kessler, and U. Seifert, “Micro-capsules in shear flow,” *J. Phys. Cond. Mat.*, vol. 23, p. 184113, Apr. 2011.
- [84] D. V. Le, “Effect of bending stiffness on the deformation of liquid capsules enclosed by thin shells in shear flow,” *Phys. Rev. E*, vol. 82, p. 016318, July 2010.
- [85] P. Pranay, S. G. Anekal, J. P. Hernandez-Ortiz, and M. D. Graham, “Pair collisions of fluid-filled elastic capsules in shear flow: Effects of membrane properties and polymer additives,” *Phys. Fluids*, vol. 22, no. 12, p. 123103, 2010.

- [86] W. R. Dodson and P. Dimitrakopoulos, “Dynamics of strain-hardening and strain-softening capsules in strong planar extensional flows via an interfacial spectral boundary element algorithm for elastic membranes,” *J. Fluid Mech.*, vol. 641, p. 263, Nov. 2009.
- [87] S. Kessler, R. Finken, and U. Seifert, “Elastic capsules in shear flow: Analytical solutions for constant and time-dependent shear rates,” *Eur. Phys. J. E*, vol. 29, pp. 399–413, Aug. 2009.
- [88] S. Kessler, R. Finken, and U. Seifert, “Swinging and tumbling of elastic capsules in shear flow,” *J. Fluid Mech.*, vol. 605, May 2008.
- [89] Y. Sui, Y. Chew, P. Roy, X. Chen, and H. Low, “Transient deformation of elastic capsules in shear flow: Effect of membrane bending stiffness,” *Phys. Rev. E*, vol. 75, p. 066301, June 2007.
- [90] E. Lac, D. Barthès-Biesel, N. A. Pelekasis, and J. Tsamopoulos, “Spherical capsules in three-dimensional unbounded Stokes flows: effect of the membrane constitutive law and onset of buckling,” *J. Fluid Mech.*, vol. 516, pp. 303–334, 2004.
- [91] D. Barthès-Biesel and J. M. Rallison, “The time-dependent deformation of a capsule freely suspended in a linear shear,” *J. Fluid Mech.*, vol. 113, p. 251, 1981.
- [92] D. Barthès-Biesel, “Motion of a spherical microcapsule freely suspended in a linear shear,” *J. Fluid Mech.*, vol. 100, p. 831, Nov. 1980.
- [93] D. Barthès-Biesel, “Modeling the motion of capsules in flow,” *Curr. Opin. Coll. Int. Sci.*, vol. 16, pp. 3–12, Feb. 2011.
- [94] J. A. Sherburn, M. I. Hammons, and M. J. Roth, “Modeling finite thickness slab perforation using a coupled eulerian–lagrangian approach,” *International Journal of Solids and Structures*, vol. 51, pp. 4406–4413, 2014.
- [95] F. Kobeissy, “Brain neurotrauma: Molecular, neuropsychological, and rehabilitation aspects,” *CRC Press*, 2015.
- [96] V. Meyer, “Frontiers in offshore geotechnics iii,” *CRC Press*, 2015.
- [97] V. Flamini, A. DeAnda, and B. E. Griffith, “Immersed boundary-finite element model of fluid–structure interaction in the aortic root,” *Theoretical and Computational Fluid Dynamics*, vol. 30, pp. 139–164, 2016.
- [98] A. M. Bavo, G. Rocatello, F. Iannaccone, J. Degroote, J. Vierendeels, and P. Segers, “Fluid–structure interaction simulation of prosthetic aortic valves: Comparison between immersed boundary and arbitrary lagrangian-eulerian techniques for the mesh representation,” *PLoS One*, vol. 11, no. 4, p. e0154517, 2016.
- [99] H. Gao, H. Wang, C. Berry, X. Luo, and B. E. Griffith, “Quasi-static image-based immersed boundary-finite element model of left ventricle under diastolic loading,” *International Journal for Numerical Methods in Biomedical Engineering*, vol. 30.

- [100] K. S. Chang and W. L. Olbricht, "Experimental studies of the deformation and breakup of a synthetic capsule in steady and unsteady simple shear flow," *J. Fluid Mech.*, vol. 250, pp. 609–633, 1993.
- [101] A. Walter, H. Rehage, and H. Leonhard, "Shear-induced deformations of polyamide microcapsules," *Colloid. Polym. Sci.*, vol. 175, pp. 169–175, 2000.
- [102] A. Walter, H. Rehage, and H. Leonhard, "Shear induced deformation of microcapsules: shape oscillations and membrane folding," *Colloids and Surfaces A: Physicochemical and Engineering Aspects*, vol. 183-185, pp. 123–132, 2001.
- [103] C. Dupont, A. V. Salsac, D. Barthès-Biesel, M. Vidrascu, and P. Le Tallec, "Influence of bending resistance on the dynamics of a spherical capsule in shear flow," *Phys. Fluids*, vol. 27, pp. 051902–16, May 2015.
- [104] I. Koleva and H. Rehage, "Deformation and orientation dynamics of polysiloxane microcapsules in linear shear flow," *Soft Matter*, vol. 8, no. 13, pp. 3681–13, 2012.
- [105] S. K. H. Gulrez, S. Al-Assaf, and G. O. Phillip, "Hydrogels: Methods of preparation, characterisation and applications," *Progress in Molecular and Environmental Bioengineering—From Analysis and Modeling to Technology Applications*, Intech Europe, Croatia, 2011.
- [106] N. Kashyap, N. Kumar, and M. Kumar, "Hydrogels for pharmaceutical and biomedical applications," *Critical Reviews in Therapeutic Drug Carrier Systems*, vol. 22, no. 2, pp. 107–150, 2005.
- [107] A. Hoffman, "Hydrogels for biomedical applications," *Advanced Drug Delivery Reviews*, vol. 54, pp. 3–12, 2002.
- [108] E. M. Ahmed, "Hydrogel: Preparation, characterization, and applications: A review," *Journal of Advanced Research*, vol. 6, no. 2, pp. 105–121, 2015.
- [109] L. Liu, A. Ghaemi, S. Gekle, and S. Agarwal, "One-component dual actuation: Poly(NIPAM) can actuate to stable 3D forms with reversible size change," *Adv. Mater.*, vol. 28, 2016.
- [110] L. Liu, S. Jiang, Y. Sun, and S. Agarwal, "Giving direction to motion and surface with ultra-fast speed using oriented hydrogel fibers," *Adv. Function. Mater.*, vol. 26, pp. 1021–1027, 2016.
- [111] L. Ionov, "Hydrogel-based actuators: possibilities and limitations," *Materials Today*, vol. 17, pp. 494–503, 2014.
- [112] A. Holm, C. Erasmo, and K. Gennady, "Analysis and modelling of advanced structures and smart systems," *Springer Nature Singapore Ltd.*, 2018.
- [113] E. Palleau, D. Morales, M. D. Dickey, and O. D. Velev, "Reversible patterning and actuation of hydrogels by electrically assisted ionoprinting," *Nature Communications*, vol. 4, no. 2257, pp. 1–7, 2013.

- [114] D. Morales, I. Podolsky, R. W. Mailen, M. D. D. T. Shay, and O. D. Velev, "Ionoprinted multi-responsive hydrogel actuators," *Micromachines*, vol. 7, no. 98, pp. 1–15, 2016.
- [115] W. Guo, M. Li, and J. Zhou, "Modeling programmable deformation of self-folding all-polymer structures with temperature-sensitive hydrogels," *Smart Materials and Structures*, vol. 22, no. 115028, pp. 1–6, 2013.
- [116] T. van Manen, S. Janbaz, and A. Zadpoor, "Programming the shape-shifting of flat soft matter," *Materials Today*, vol. In Press, 2017.
- [117] S. Timoshenko, "Analysis of bi-metal thermostats," *Journal of the Optical Society of America*, vol. 11, pp. 233–255, 1925.
- [118] A. S. Gladman, E. A. Matsumoto, R. G. Nuzzo, L. Mahadevan, and J. A. Lewis, "Biomimetic 4d printing," *Nature Materials*, vol. 15, pp. 413–419, 2016.
- [119] Q. Li, "Intelligent stimuli-responsive materials: From well-defined nanostructures to applications," *John Wiley & Sons Inc.*, 2013.
- [120] D. Liu and D. Broer, "Responsive polymer surfaces: Dynamics in surface topography," *Wiley-VCH Verlag GmbH & Co. KGaA*, 2017.
- [121] V. Kozlovskaya, B. Xue, and E. Kharlampieva, "Shape-adaptable polymeric particles for controlled delivery," *Macromolecules*, vol. 49, pp. 8373–8386, 2016.
- [122] K. Urdl, A. Kandelbauer, W. Kern, U. Müller, M. Thebault, and E. Zikulnig-Rusch, "Self-healing of densely crosslinked thermoset polymers—a critical review," *Progress in Organic Coatings*, vol. 104, pp. 232–249, 2017.
- [123] E. Jeoffroy, A. F. Demirörs, P. Schwendimann, S. D. Santos, S. Danzi, A. Hauser, M. N. Partl, and A. R. Studart, "One-step bulk fabrication of polymer-based microcapsules with hard–soft bilayer thick shells," *ACS Appl. Mater. Interfaces*, vol. 9, pp. 37364–37373, 2017.
- [124] Y. Pang, X. Duan, G. Ren, and W. Liu, "Comparative study on different drying methods of fish oil microcapsules," *Journal of Food Quality*, vol. 2017, pp. 1–7, 2017.
- [125] Y. Yoo, C. Martinez, and J. P. Youngblood, "Synthesis and characterization of microencapsulated phase change materials with poly(urea-urethane) shells containing cellulose nanocrystals," *ACS Appl. Mater. Interfaces*, vol. 9, pp. 31763–31776, 2017.
- [126] K. Bando and Y. Yamaguchi, "Mechanical characterization of apa microcapsules by parallel-plate compression," *Journal of Membrane and Separation Technology*, vol. 6, pp. 40–47, 2017.
- [127] Y. Yoo, C. Martinez, and J. P. Youngblood, "Sustained dye release using poly(urea-urethane)/cellulose nanocrystal composite microcapsules," *Langmuir*, vol. 33, pp. 1521–1532, 2017.
- [128] Q. Zhao, J. W. Dunlop, X. Qiu, F. Huang, Z. Zhang, J. Heyda, J. Dzubiella, M. Antonietti, and J. Yuan, "An instant multi-responsive porous polymer actuator driven by solvent molecule sorption," *Nature Communications*, vol. 5, no. 4293, pp. 1–8, 2014.

- [129] S. S. Bansode, S. K. Banarjee, D. D. Gaikwad, S. L. Jadhav, and R. M. Thora, "Microencapsulation: A review," *International Journal of Pharmaceutical Sciences Review and Research*, vol. 1, pp. 38–43, 2010.
- [130] J. Sri.S, A.Seethadevi, K. Prabha, P.Muthuprasanna, and P.Pavitra, "Microencapsulation: A review," *International Journal of Pharma and Bio Sciences*, vol. 3, pp. 509–531, 2012.
- [131] K. Tsuji, "Microencapsulation of pesticides and their improved handling safety," *J Microencapsulation*, vol. 18, pp. 137–47, 2001.
- [132] B. Wang, H. Sheng, Y. Shi, W.Hu, N. Hong, W. Zeng, H. Ge, X. Yu, L. Song, and Y. Hu, "Recent advances for microencapsulation of flame retardant," *Polymer Degradation and Stability*, vol. 113, pp. 96–109, 2015.
- [133] B. Gibbs, S. Kermasha, I. Alli, and C. Mulligan, "Encapsulation in the food industry: a review," *International Journal of Food Sciences and Nutrition*, vol. 50, pp. 213–224, 1999.
- [134] E. Koh, N. Kim, J. Shin, and Y. Kim, "Polyurethane microcapsules for self-healing paint coatings," *RSC Adv.*, vol. 4, pp. 16214–16223, 2014.
- [135] V. Tyagia, S. Kaushika, S. Tyagib, and T. Akiyamac, "Development of phase change materials based microencapsulated technology for buildings: A review," *Renewable and Sustainable Energy Reviews*, vol. 15, pp. 1373–1391, 2011.
- [136] P. Schossiga, H. Henninga, S. Gschwandera, and T. Haussmann, "Micro-encapsulated phase-change materials integrated into construction materials," *Solar Energy Materials and Solar Cells*, vol. 89, pp. 297–306, 2005.
- [137] E. N. Brown, S. R. White, and N. R. Sottos, "Microcapsule induced toughening in a self-healing polymer composite," *J. Mater. Sci.*, vol. 39, pp. 1703–1710, 2004.
- [138] A. Mac, D. Negi, and D. Friend, "Preparation and characterization of poly(styrene) microcapsules containing corrosion inhibitors," *Journal of Microencapsulation*, vol. 6, pp. 361–367, 1989.
- [139] M. F. Bédard, B. G. D. Geest, A. G. Skirtach, H. Möhwald, and G. B. Sukhorukov, "Polymeric microcapsules with light responsive properties for encapsulation and release," *Adv. Colloid Interface Sci.*, vol. 158, pp. 2–14, 2010.
- [140] S. Carregal-Romero, P. Guardia, X. Yu, R. Hartmann, T. Pellegrino, and W. J. Parak, "Magnetically triggered release of molecular cargo from iron oxide nanoparticle loaded microcapsules," *Nanoscale*, vol. 20, pp. 570–576, 2015.
- [141] P. Degen, E. Zwar, I. Schulz, and H. Rehage, "Magneto-responsive alginate capsules," *J. Phys.: Condens. Matter*, vol. 27, pp. 194–105, 2015.
- [142] C. Peyratout and L. Dähne, "Tailor-made polyelectrolyte microcapsules: from multi-layers to smart containers," *Angew Chem Int Ed Engl.*, vol. 43, pp. 3762–83, 2004.

- [143] Q. He, Y. Cui, and J. Li, "Molecular assembly and application of biomimetic microcapsules," *Chem Soc Rev*, vol. 38, pp. 2292–2303, 2009.
- [144] R. Verberg, A. T. Dale, P. Kumar, A. Alexeev, and A. C. Balazs, "Healing substrates with mobile, particle-filled microcapsules: designing a repair and go system," *J. R. Soc. Interface*, vol. 4, pp. 349–357, 2007.
- [145] H. Masoud and A. Alexeev, "Controlled release of nanoparticles and macromolecules from responsive microgel capsules," *ACS Nano*, vol. 6, pp. 212–219, 2012.
- [146] V. Nguyen, C. Wang, C. Thomas, and Z. Zhang, "Mechanical properties of single alginate microspheres determined by microcompression and finite element modeling," *Chemical Engineering Science*, vol. 64, pp. 821–829, 2009.
- [147] R. Hartmann, M. Weidenbach, M. Neubauer, A. Fery, and W. J. Parak, "Stiffness-dependent in vitro uptake and lysosomal acidification of colloidal particles," *Angewandte Chem. Int. Ed.*, vol. 54, pp. 1365–1368, 2015.
- [148] M. P. Neubauer, M. Poehlmann, and A. Fery, "Microcapsule mechanics: From stability to function," *Adv Colloid Interface Sci*, vol. 207, pp. 65–80, 2014.
- [149] K. Cole and E. M. Michaelis, "Surface forces of fertilized arbacia eggs," *J. Cell. Comp. Physiol.*, vol. 2, pp. 121–126, 1932.
- [150] T. Lim, B. Smith, and D. McDowel, "Behavior of a random hollow sphere metal foam," *Acta Materialia*, vol. 50, pp. 2867–2879, 2002.
- [151] K. Carlisle, M. Lewis, K. Chawla, M. Koopman, and G. Gladysz, "Finite element modeling of the uniaxial compression behavior of carbon microballoons," *Acta Materialia*, vol. 55, pp. 2301–2318, 2007.
- [152] A. Fery and R. Weinkamer, "Mechanical properties of micro- and nanocapsules: Single-capsule measurements," *Polymer*, vol. 48, pp. 7221–7235, 2007.
- [153] R. Mercadé-Prieto, C. R. Thomas, and Z. Zhang, "Mechanical double layer model for *Saccharomyces Cerevisiae* cell wall," *Eur. Biophys. J.*, vol. 42, pp. 613–620, May 2013.
- [154] M. P. Neubauer, M. Poehlmann, and A. Fery, "Microcapsule mechanics: From stability to function," *Adv. Coll. Int. Sci.*, vol. 207, pp. 65–80, May 2014.
- [155] K. B. Carlisle, K. K. Chawla, G. M. Gladysz, and M. Koopman, "Structure and mechanical properties of micro and macro balloons: An overview of test techniques," *J Mater Sci*, vol. 41, pp. 3961–3972, June 2006.
- [156] K. Tsuji, "Microencapsulation of pesticides and their improved handling safety," *J Microencapsul*, vol. 18, pp. 137–147, Mar. 2001.
- [157] B. Wang, H. Sheng, Y. Shi, W. Hu, N. Hong, W. Zeng, H. Ge, X. Yu, L. Song, and Y. Hu, "Recent advances for microencapsulation of flame retardant," *Polymer Degradation and Stability*, vol. 113, pp. 96–109, Mar. 2015.

- [158] I. T. Carvalho, B. N. Estevinho, and L. Santos, "Application of microencapsulated essential oils in cosmetic and personal healthcare products - a review," *Int J Cosmet Sci*, vol. 38, pp. 109–119, May 2015.
- [159] R. Hartmann, M. Weidenbach, M. Neubauer, A. Fery, and W. J. Parak, "Stiffness-Dependent In Vitro Uptake and Lysosomal Acidification of Colloidal Particles," *Angew. Chem. Int. Ed.*, vol. 54, pp. 1365–1368, Dec. 2014.
- [160] A. Le Goff, B. Kaoui, G. Kurzawa, B. Haszon, and A.-V. Salsac, "Squeezing bio-capsules into a constriction: deformation till break-up," *Soft Matter*, vol. 13, pp. 7644–7648, Oct. 2017.
- [161] A. Fery and R. Weinkamer, "Mechanical properties of micro- and nanocapsules: Single-capsule measurements," *Polymer*, vol. 48, pp. 7221–7235, Nov. 2007.
- [162] V. V. Lulevich, D. Andrienko, and O. I. Vinogradova, "Elasticity of polyelectrolyte multilayer microcapsules," *J. Chem. Phys.*, vol. 120, no. 8, p. 3822, 2004.
- [163] Y. Lefebvre, E. Leclerc, D. Barthès-Biesel, J. Walter, and F. Edwards-Levy, "Flow of artificial microcapsules in microfluidic channels: A method for determining the elastic properties of the membrane," *Phys. Fluids*, vol. 20, pp. 123102–10, Dec. 2008.
- [164] C. de Loubens, J. Deschamps, F. Edwards-Levy, and M. Leonetti, "Tank-treading of microcapsules in shear flow," *J. Fluid Mech.*, vol. 789, pp. 750–767, Jan. 2016.
- [165] A. Guckenberger and S. Gekle, "Theory and algorithms to compute Helfrich bending forces: a review," *J. Phys. Cond. Mat.*, vol. 29, pp. 203001–30, Apr. 2017.
- [166] G. Sun and Z. Zhang, "Mechanical properties of melamine-formaldehyde microcapsules," *Journal of Microencapsulation*, vol. 18, pp. 593–602, 2001.
- [167] B. Li, T. Du, B. Yu, J. van der Gucht, and F. Zhou, "Caterpillar-inspired design and fabrication of a self-walking actuator with anisotropy, gradient, and instant response," *Small*, vol. 11, pp. 3494–3501, 2015.
- [168] L. Zhang, S. Chizhik, Y. Wen, and P. Naumov, "Directed motility of hygroresponsive biomimetic actuators," *Adv. Funct. Mater.*, vol. 26, pp. 1040–1053, 2016.
- [169] B. Xu, H. Jiang, H. Li, G. Zhang, and Q. Zhang, "High strength nanocomposite hydrogel bilayer with bidirectional bending and shape switching behaviors for soft actuators," *RSC Adv.*, vol. 5, pp. 13167–13170, 2015.
- [170] D. Kim, H. Lee, and J. Yoon, "Highly bendable bilayer-type photo-actuators comprising of reduced graphene oxide dispersed in hydrogels," *Sci. Rep.*, vol. 6, p. 20921, 2016.
- [171] J. Robertson, A. Torbati, E. Rodriguez, Y. Mao, R. Baker, H. Qi, and P. Mather, "Mechanically programmed shape change in laminated elastomeric composites," *Soft Matter*, vol. 11, pp. 5754–5764, 2015.
- [172] L. Zhang, I. Desta, and P. Naumov, "Synergistic action of thermoresponsive and hygroresponsive elements elicits rapid and directional response of a bilayer actuator," *Chem. Commun.*, vol. 52, pp. 5920–5920, 2016.

- [173] D. V. Opdenbosch, G. Fritz-Popovski, W. Wagermaier, O. Paris, and C. Zollfrank, "Moisture-driven ceramic bilayer actuators from a biotemplating approach," *Adv. Mater.*, vol. 28, pp. 5235–5240, 2016.
- [174] M. Ji, N. Jiang, J. Chang, and J. Sun, "Near-infrared light-driven, highly efficient bilayer actuators based on polydopamine-modified reduced graphene oxide," *Adv. Funct. Mater.*, vol. 24, pp. 5412–5419, 2014.
- [175] X. Zhang, Z. Yu, C. Wang, D. Zarrouk, J. Seo, J. Cheng, A. Buchan, K. Takei, Y. Zhao, J. Ager, J. Zhang, M. Hettick, M. Hersam, A. Pisano, R. Fearing, and A. Javey, "Photoactuators and motors based on carbon nanotubes with selective chirality distributions," *Nature Communications*, vol. 5, p. 2983, 2014.
- [176] E. Wang, M. Desai, and S. Lee, "Light-controlled graphene-elastin composite hydrogel actuators," *Nano Letters*, vol. 13, pp. 2826–2830, 2013.
- [177] Y. Kim, M. Liu, Y. Ishida, Y. Ebina, M. Osada, T. Sasaki, T. Hikima, M. Takata, and T. Aida, "Thermoresponsive actuation enabled by permittivity switching in an electrostatically anisotropic hydrogel," *Nature Materials*, vol. 14, pp. 1002–1007, 2015.
- [178] M. Dai, O. T. Picot, J. M. N. Verjans, L. T. de Haan, A. P. H. Schenning, T. Peijs, and C. W. M. Bastiaansen, "Humidity-responsive bilayer actuators based on a liquid-crystalline polymer network," *ACS Appl. Mater. Interfaces*, vol. 5, pp. 4945–4950, 2013.
- [179] X. Xie, L. Qu, C. Zhou, Y. Li, J. Zhu, H. Bai, G. Shi, and L. Dai, "An asymmetrically surface-modified graphene film electrochemical actuator," *ACS Nano*, vol. 4, pp. 6050–6054, 2010.
- [180] S. Taccola, F. Greco, E. Sinibaldi, A. Mondini, B. Mazzolai, and V. Mattoli, "Toward a new generation of electrically controllable hygromorphic soft actuators," *Adv. Mater.*, vol. 27, pp. 1668–1665, 2015.
- [181] J. Kim, S. Chung, S. Choi, H. Lee, J. Kim, and S. Kwon, "Programming magnetic anisotropy in polymeric microactuators," *Nature Materials*, vol. 10, pp. 747–752, 2011.
- [182] Y. Haldorai and J. Shim, "Chemo-responsive bilayer actuator film: fabrication, characterization and actuator response," *New J. Chem.*, vol. 38, pp. 2653–2659, 2014.
- [183] M. Islam and M. Serpe, "Poly(n-isopropylacrylamide) microgel-based thin film actuators for humidity sensing," *RSC Advances*, vol. 4, pp. 31937–31940, 2014.
- [184] Y. Yamamoto, K. Kanao, T. Arie, S. Akita, and K. Takei, "Air ambient-operated pnipam-based flexible actuators stimulated by human body temperature and sunlight," *ACS Appl. Mater. Interfaces*, vol. 7, pp. 11002–11006, 2015.
- [185] X. Zhang, C. Pint, M. Lee, B. Schubert, A. Jamshidi, K. Takei, H. Ko, A. Gillies, J. U. R. Bardhan, M. Wu, R. Fearing, and A. Javey, "Optically- and thermally-responsive programmable materials based on carbon nanotube-hydrogel polymer composites," *Nano Letters*, vol. 11, pp. 3239–3244, 2011.

- [186] L. Ionov, "Polymer origami: programming the folding with shape," *e-Polymers*, vol. 14, pp. 109–114, 2014.
- [187] S. Jiang, F. Lium, A. Lerch, L. Ionov, and S. Agarwal, "Unusual and superfast temperature-triggered actuators," *Adv. Mater.*, vol. 27, pp. 4865–4870, 2015.
- [188] L. Liu, S. Jiang, Y. Sun, and S. Agarwal, "Giving direction to motion and surface with ultra-fast speed using oriented hydrogel fibers," *Adv. Funct. Mater.*, vol. 26, pp. 1021–1027, 2016.
- [189] A. Yarin and S. Agarwal, "Buckling and unraveling poly(n-isopropyl acrylamide)-thermoplastic polyurethane bilayers," *Polymer*, vol. 97, pp. 604–613, 2016.
- [190] S. Douezan, M. Wyart, F. Brochard-Wyart, and D. Cuvelier, "Curling instability induced by swelling," *Soft Matter*, vol. 7, pp. 1506–1511, 2011.
- [191] R. M. Erb, J. Sander, R. Grisch, and A. Studart, "Self-shaping composites with programmable bioinspired microstructures," *Nature Communications*, vol. 4, p. 1712, 2013.
- [192] J. Mu, C. Hou, B. Zhu, H. Wang, Y. Li, and Q. Zhang, "A multi-responsive water-driven actuator with instant and powerful performance for versatile applications," *Sci. Rep.*, vol. 5, p. 9503, 2015.
- [193] K. Baek, J. Jeong, A. Shkumatov, R. Bashir, and H. Kong, "In situ self-folding assembly of a multi-walled hydrogel tube for uniaxial sustained molecular release," *Adv. Mater.*, vol. 25, pp. 5568–5573, 2013.
- [194] L. Liu, N. Wang, Y. Han, Y. Li, and W. Liu, "Redox-triggered self-rolling robust hydrogel tubes for cell encapsulation," *Macromol. Rapid Commun.*, vol. 35, p. 344–349, 2014.
- [195] T. Asoh, M. Matsusaki, T. Kaneko, and M. Akashi, "Fabrication of temperature-responsive bending hydrogels with a nanostructured gradient," *Adv. Mater.*, vol. 20, pp. 2080–2083, 2008.
- [196] R. Namani, M. D. Wood, S. E. Sakiyama-Elbert, and P. V. Bayly, "Anisotropic mechanical properties of magnetically aligned fibrin gels measured by magnetic resonance elastography," *Journal of Biomechanics*, vol. 42, pp. 2047–2053, 2009.
- [197] G. Stoychev, N. Pureskiy, and L. Ionov, "Self-folding all-polymer thermoresponsive microcapsules," *Soft Matter*, vol. 7, pp. 3277–3279, 2011.
- [198] R. Dersch, T. Liu, A. Schaper, A. Greiner, and J. Wendorff, "Electrospun nanofibers: Internal structure and intrinsic orientation," *J. Polym. Sci. A Polym. Chem.*, vol. 41, pp. 545–553, 2003.

## **Eidesstattliche Versicherung**

Hiermit versichere ich an Eides statt, dass ich die vorliegende Arbeit selbstständig verfasst und keine anderen als die von mir angegebenen Quellen und Hilfsmittel verwendet habe. Weiterhin erkläre ich, dass ich die Hilfe von gewerblichen Promotionsberatern bzw. –vermittlern oder ähnlichen Dienstleistern weder bisher in Anspruch genommen habe, noch künftig in Anspruch nehmen werde. Zusätzlich erkläre ich hiermit, dass ich keinerlei frühere Promotionsversuche unternommen habe.

Bayreuth, den

Ali Ghaemi

